AD NUMBER

AD865728

NEW LIMITATION CHANGE

TO

Approved for public release, distribution unlimited

FROM

Distribution authorized to U.S. Gov't. agencies and their contractors; Administrative/Operational Use; Dec 1969. Other requests shall be referred to Air Force Materials Lab., Attn: MAMC, Wright-Patterson AFB, OH 45433.

AUTHORITY

AFML ltr, 29 Mar 1972

AFML-TR-69-84
PART IV – VOLUME I

STABILITY CHARACTERIZATION OF REFRACTORY MATERIALS UNDER HIGH VELOCITY ATMOSPHERIC FLIGHT CONDITIONS

PART IV – VOLUME I: THEORETICAL CORRELATION OF MATERIAL PERFORMANCE WITH STREAM CONDITIONS

LARRY KAUFMAN, HARVEY NESOR, HAROLD BERNSTEIN
and JUDSON R. BARON
ManLabs, Inc.

TECHNICAL REPORT AFML-TR-69-84, PART IV, VOLUME I

DECEMBER 1969

This document is subject to special export controls and each transmittal to foreign governments or foreign nationals may be made only with prior approval of the Air Force Materials Laboratory (MAMC), Wright-Patterson Air Force Base, Ohio 45433.

AIR FORCE MATERIALS LABORATORY
AIR FORCE SYSTEMS COMMAND
WRIGHT-PATTERSON AIR FORCE BASE, OHIO

129

NOTICE

When Government drawings, specifications, or other data are used for any purpose other than in connection with a definitely related Government procurement operation, the United States Government thereby incurs no responsibility nor any obligation whatsoever; and the fact that the government may have formulated, furnished, or in any way supplied the said drawings, specifications, or other data, is not regarded by implication or otherwise as in any manner licensing the holder or any other person or corporation, or conveying any rights or permission to manufacture, use, or sell any patented invention that may in any way be related thereto.

This document is subject to special export controls and each transmittal to foreign governments or foreign nationals may be made only with prior approval of the Air Force Materials Laboratory (MAMC), Wright-Patterson Air Force Base, Ohio 45433.

Distribution of this report is limited for the protection of technology relating to critical materials restricted by the Export Control Act.

Copies of this report should not be returned unless return is required by security considerations, contractual obligations, or notice on a specific document.

700 - January 1970 - CO455 - 106-2361

STABILITY CHARACTERIZATION OF REFRACTORY MATERIALS UNDER HIGH VELOCITY ATMOSPHERIC FLIGHT CONDITIONS

PART IV—VOLUME I: THEORETICAL CORRELATION OF MATERIAL PERFORMANCE WITH STREAM CONDITIONS

LARRY KAUFMAN

HARVEY NESOR

HAROLD BERNSTEIN

JUDSON R. BARON

This document is subject to special export controls and each transmittal to foreign governments or foreign nationals may be made only with prior approval of the Air Force Materials Laboratory (MAMC), Wright-Patterson Air Force Base, Ohio 45433.

FOREWORD

This report was prepared by ManLabs, Inc. under Project 7312, "Metal Surface Deterioration and Protection, "Task 731201, "Metal Surface Protection," and Project 7350, "Refractory Inorganic Nonmetallic Materials," Task Numbers 735001, "Refractory Inorganic Nonmetallic Materials: Nongraphitic," and 735002, "Refractory Inorganic Nonmetallic Materials: Graphitic," under AF33(615)-3859 and was administered by the Metals and Ceramics Divisions of the Air Force Materials Laboratory, Air Force Systems Command, with J.D. Latva, J. Krochmal, and N.M. Geyer acting as project engineers.

This report covers the period from April 1966 to July 1969.

ManLabs' personnel participating in this study included L. Kaufman, H. Nesor, H. Bernstein, J.R. Baron and G. Stepakoff.

The manuscript of this report was released by the authors in September 1969 for publication. This technical report has been reviewed and is approved.

W. G. Ramke
Chief, Ceramics and Graphite Branch
Metals and Ceramics Division
Air Force Materials Laboratory

The following reports will be issued under this contract.

Part/Volume	
I-I	Summary of Results
II-I	Facilities and Techniques Employed for Characterization of Candidate Materials
II-II	Facilities and Techniques Employed for Cold Gas/Hot Wall Tests
II-III	Facilities and Techniques Employed for Hot Gas/Cold Wall Tests
III-I	Experimental Results of Low Velocity Cold Gas/Hot Wall Tests
III-II	Experimental Results of High Velocity Cold Gas/Hot Wall Tests
III-III	Experimental Results of High Velocity Hot Gas/Cold Wall Tests
IV-I	Theoretical Correlation of Material Performance with Stream Conditions
IV-II	Calculation of the General Surface Reaction Problem

ABSTRACT

The oxidation of refractory borides, graphites and JT composites, hypereutectic carbide-graphite composites, refractory metals, coated refractory metals, metal-oxide composites, and iridium coated graphites in air has been studied under high velocity atmospheric flight conditions. Elucidation of the relationship between hot gas/cold wall (HG/CW) and cold gas/hot wall (CG/HW) surface effects in terms of heat and mass transfer rates at high temperatures was a principal goal.

Published arc plasma test data for refractory materials taken in eight different facilities were collected and examined by comparing the observed surface temperature with calculated radiation equilibrium values. Wide variations in the ratio of calculated to observed temperature were encountered. Similar calculations performed for tests conducted in the present program yielded results close to unity especially when melting is encountered. Larger ratios (up to 1.5) were noted for specific materials which produce silicon oxides, implying enhanced resistance to energy absorbtion. Thus, an alternative method of presentation which compares recession rate as a function of heat flux and enthalpy for the candidate materials was developed. This description provides a means for comparing performance for various trajectories by applying a flux/enthalpy-altitude/velocity translation in considering candidate materials. Comparison of the trajectory of the FDL-7MC lifting reentry vehicle (Lift/Drag ratio between 2.5 and 3.0 and a 3" nose radius) eliminates all of the candidate materials except the boride composites. These composites have survived multicycle exposures totaling 20,000 seconds under conditions simulating the most severe portions of the FDL-7MC trajectory.

Calculations of the flux-enthalpy boundaries for recession rates of 1 mil/sec based on melting of the solid oxide forming materials are found to compare reasonably with observations. The model employed for these calculations is based on providing the latent heat required for melting at a rate of 1 mil/sec.

Calculation of the surface temperature based on stream and material properties is presented to predict internal temperature gradients for comparison with the "in-depth" measurements. Temperature gradients along the axis of a right circular cylinder which is heated from one end in an arc plasma test with front face and side radiation losses are considered. The effects of radius, length, thermophysical properties and an oxide film on the front face are included. Measurement of temperature gradients through oxide films formed during arc plasma exposures indicate substantial gradients ($1000^{o}R$ through 100 mils) can exist. Comparison of the measurements with computed results yield good agreement in view of the simple models employed. Explicit models are presented for computing the rate of graphite recession in air as a function of density, surface temperature, gas velocity, stagnation pressure and sample radius. The results are compared with observations covering a wide range of conditions.

TABLE OF CONTENTS

LIST OF TABLES

LIST OF ILLUSTRATIONS

Figure		Page

Figure		Page
31	Recession Rates of PG(B-6) and BPG(B-7) as a Function of Heat Flux and Stagnation Enthalpy	98
32	Recession Rates of HfC+C(C-11), ZrC+C(C-12), Si/RVC (B-8) and KT-SiC(E-14) as a Function of Heat Flux and Stagnation Enthalpy	99
33	Recession Rates of JTA(D-13), JT0992(F-15) and JT0981 (F-16) as a Function of Heat Flux and Stagnation Enthalpy	100
34	Recession Rates of WSi_2/W(G-18), Sn-Al/Ta-W(G-19), W+Zr+Cu(G-20) and W/Ag(G-21) as a Function of Heat Flux and Stagnation Enthalpy	101
35	Recession Rates of SiO_2+W(H-22)(H-23), Hf-Ta-Mo(I-23) and Ir/C(I-24) as a Function of Heat Flux and Stagnation Enthalpy	102
36	Location of 1 mil/sec Recession Rate Boundary as a Function of Heat Flux and Enthalpy for Refractory Materials at P_e = 1 atm.	103
37	Recession Rate of Hafnium Diboride as a Function of Heat Flux and Stagnation Enthalpy	104
38	Recession Rate of Zirconium Diboride as a Function of Heat Flux and Stagnation Enthalpy	105
39	Recession Rate of HfB_2 + SiC Composites as a Function of Heat Flux and Stagnation Enthalpy	106
40	Superposition of the FDL-7MC Trajectory on the Flux-Enthalpy Map showing Recession Rates for Refractory Materials	107
41	Computed Boundaries for Melting Recession of $HfB_{2.1}$ (A-2)	108
42	Computed Boundaries for Melting Recession of ZrB_2 (A-3)	109
43	Computed Boundaries for Melting Recession of HfC+C (C-11)	110
44	Computed Boundaries for Melting Recession of ZrC+C (C-12)	111
45	Variation of $\overline{T}_i$ with $\overline{T}_t$ for a Number of C_S Values According to Eq. 64 when I/L = 0 and k_F/k_S = 0.10	112

I. INTRODUCTION AND SUMMARY

A. Introduction

The response of refractory materials to high temperature oxidizing conditions imposed by furnace heating has been observed to differ markedly from the behavior in arc plasma "reentry simulators." The former evaluations are normally performed for long times at fixed temperatures and slow gas flows with well-defined solid/gas-reactant/product chemistry. The latter on the other hand are usually carried out under high velocity gas flow conditions in which the energy flux rather than the temperature is defined and significant shear forces can be encountered. Consequently, the differences in philosophy, observables, and techniques used in the "material centered" regime and the "environment centered, reentry simulation" area differ so significantly as to render correlation of material responses at high and low speeds difficult if not impossible in many cases. Under these circumstances, expeditious utilization of the vast background of information available in either area for optimum matching of existing material systems with specific missions or prediction and synthesis of advanced material systems to meet requirements of projected missions is sharply curtailed.

In order to progress toward the elimination of this gap, an integrated study of the response of refractory materials to oxidation in air over a wide range of time, gas velocity, temperature and pressure has been designed and implemented. This interdisciplinary study spans the heat flux and boundary layer-shear spectrum of conditions encountered during high-velocity atmospheric flight as well as conditions normally employed in conventional materials centered investigations. In this context, significant efforts have been directed toward elucidating the relationship between hot gas/cold wall HG/CW and cold gas/hot wall CG/HW surface effects in terms of heat and mass transfer rates at high temperatures, so that full utilization of both types of experimental data can be made. The elucidation of various mass transfer reaction regimes have been studies in gaseous and solid oxide formation.

The principal goal of this study is the coupling of the material-centered and environment-centered philosophies in order to gain a better insight into systems behavior under high-speed atmospheric flight conditions. This coupling function has been provided by an interdisciplinary panel composed of scientists representing the component philosophies. The coupling framework consists of an intimate mixture of theoretical and experimental studies specifically designed to overlap temperature/energy and pressure/velocity conditions. This overlap has provided a means for the evaluation of test techniques and the performance of specific materials systems under a wide range of flight conditions. In addition, it provides a base for developing an integrated theory or modus operandi capable of translating reentry systems requirements such as velocity, altitude, configuration, and life time into requisite materials properties as vaporization rates, oxidation kinetics, density, etc., over a wide range of conditions.

The correlation of heat flux, stagnation enthalpy, Mach No., stagnation pressure, and specimen geometry with surface temperature through the utilization of thermodynamic, thermal and radiational properties of the material and environmental systems used in this study was of prime importance in defining the conditions for overlap between materials-centered and environment-centered tests.

Significant practical as well as fundamental progress along the above mentioned lines necessitated evaluation of refractory material systems which exhibit varying gradations of stability above 2700°F. Emphasis was placed on candidates for 3400°F to 6000°F exploitation. Thus, borides, carbides, boride-graphite composites (JTA), JT composites, carbide-graphite composites, pyrolytic and bulk graphite, PT graphite, coated refractory metals/alloys, oxide-metal composites, oxidation-resistant refractory metal alloys, and coated graphites were considered. Similarly, a range of test facilities and techniques including oxygen pickup measurements, cold sample hot gas, and hot sample cold gas devices at low velocities as well as different arc plasma facilities capable of covering the 50-2500 BTU/ft^2sec flux range under conditions equivalent to speeds up to Mach 12 at altitudes up to 200,000 ft were employed. Stagnation pressures covered the range between 0.001 and 10 atmospheres. Splash and pipe tests were performed in order to evaluate the effects of aerodynamic shear. Based on the present results, this range of heat flux and stagnation enthalpy produced surface temperatures between 2000°F and 6500°F.

B. Summary

The present report, which is the seventh in a series (1-6)*, deals with theoretical methods for correlating the performance of the candidate refractory materials with stream conditions. In many respects, this correlation constitutes the essence of the entire study. Thus, given stream characteristics such as stagnation enthalpy, stagnation pressure and cold wall heat flux, is it possible to provide a means for predicting the response of a candidate material upon insertion into this stream? The development of such methods would be of twofold value to the current program. Operationally it would provide a means for checking the internal consistency of arc plasma tests. Thus, measurements of arc plasma stream conditions could be employed to compute the surface temperature achieved by candidate materials during exposure for comparison with observed surface temperature. In addition, since the behavior of these materials is strongly dependent on the surface temperature (or temperature regime) the foregoing correlation could provide a means of describing the materials performance in terms of flight characteristics. This translation could be affected by employing the relations between altitude, velocity and body radius on the one hand and enthalpy, pressure and heat flux on the other. In this way, a logical method for comparing the requirements of specific flight trajectories with the capabilities of refractory materials could be developed.

Accordingly, activities aimed at generating such methods were carried out during the course of the program. At the outset, a literature survey of published arc plasma test data for refractory materials was performed. Data taken in eight different facilities were collected and examined

*Underscored numbers in parentheses indicate references given at the end of this report.

by comparing the observed surface temperature with values calculated on the basis of radiation equilibrium. Rather wide variations in the ratio of calculated to observed temperature, T(CALC)/T(OBS) were encountered. In most instances this ratio was greater than unity and in some instances (exposures performed in a given facility) the ratio T(CALC)/T(OBS) resulted in values near 2.0. Similar calculations were performed for all of the arc plasma tests conducted in the present program (6). In these cases (nearly 800 in total) the ratio T(CALC)/T(OBS) was reasonably close to unity. In particular the present results indicate that values near unity are observed when melting is encountered. Larger ratios (up to 1.5) were noted for specific materials which produce silicon oxides such as HfB_2+ SiC(A-4), KT-SiC(E-14), and WSi_2/W (G-18) and for Sn-Al/Ta-10W(G-19). At low temperatures (i.e., 3000°R-3500°R) these materials exhibit T(CALC)/T(OBS) ratios near 1.5 providing that melting does not occur. The occurrence of ratios which are larger than unity implies enhanced temperature capability due to resistance to energy absorbtion by the material. Although the origin of this resistance is not clear at present, it is probably due to blocking effects caused by evolution of gaseous oxides. These observations suggest a method of ranking the behavior of the refractory materials which differs from the customary recession vs. temperature curves. Thus, an alternative method of presentation which compares recession rate as a function of heat flux and enthalpy for the candidate materials was developed. This method does not require a knowledge of the spectral or the normal emittance and integrates the blocking effects characteristic of each material.

In the course of the present study, the oxidation of graphites in air has been investigated experimentally over a range of conditions (4-6) between 2500°R and 6500°R, at velocities between 1 ft/sec and Mach 3.2. The succeeding volume of this series presents a complete discussion of the surface reaction problem encountered in the oxidation of graphite. This discussion considers the coupling of mass transport through the boundary layer with reactions at the surface in detail. By contrast, the discussion presented here employs simplified models which provide an explicit means for computing the rate of graphite recession in air as a function of density, surface temperature, gas velocity, stagnation pressure and sample radius. The results are compared with observations covering a range of density between 80 and 115 lbs/ft^3, temperatures between 2500° and 6500°R, velocities between 1 ft/sec and Mach 8.0, stagnation pressures between 0.007 and 1.0 atm and nose radii between 0.005 and 0.07 ft. The current description is based on the product of Arrhenius' term and an oxygen partial pressure term. The former consists of a pre-exponential of 0.74 lbs/ft^{2}sec and an activation energy of 10,730 cal/mole. The oxygen partial pressure term has an exponent of 0.333 and is modified by an explicit correction factor which relates the oxygen concentration at the reacting surface to the oxygen concentration at the edge of the boundary layer. This correction factor is specified in terms of Mach No., body radius and pressure.

A method for describing the response of refractory materials to the enthalpy and heat flux characteristics of the stream has been developed. This description provides a means for comparing material performance at the stagnation point for various trajectories. The comparison can be made by translating the flux-enthalpy description into altitude-velocity characteristics based on established relations between stagnation pressure, altitude and velocity. The Fay-Riddell relation is employed to specify heat flux in terms of altitude, velocity and body radius. The material ranking afforded by this description shows that HfB_2+SiC(A-4) possesses the widest range of applicability of all the candidate materials investigated in the present study. In addition, the different modes of behavior exhibited by ablators (such as graphite and tungsten) and solid oxide formers are clearly displayed.

The applicability of the flux/enthalpy-altitude/velocity description in considering candidate materials has been illustrated by comparing the trajectory of the FDL-7MC lifting reentry vehicle with the behavior of candidate refractory materials. This vehicle is designed for a Lift/Drag ratio between 2.5 and 3.0. The conditions imposed by this trajectory for the case of a 3" nose radius eliminate all of the candidate materials except the boride composites. These composites have survived multicycle exposures totaling 20,000 seconds under conditions simulating the most severe portions of the FDL-7MC trajectory (6).

Calculations of the flux-enthalpy boundaries for recession rates of 1 mil/sec based on melting of the solid oxide forming materials are found to compare reasonably with observations. The model employed for these calculations is based on providing the latent heat required for melting at a rate of 1 mil/sec.

Measurement of temperature gradients which exist through oxide films formed during arc plasma exposures indicate substantial gradients (1000°R through 100 mils) can exist (6).

A first order calculation of the surface temperature as a function of stream conditions and material properties is presented in order to provide a means for predicting internal temperature gradients for comparison with the "in depth" measurements. This calculation considers temperature gradients along the axis of a right circular cylinder which is heated from one end in an arc plasma test. Front face and side radiation losses are considered in describing the effects of radius, length and thermophysical properties on the surface temperature and internal gradients. In addition, the effect of an oxide film on the front face was included. The calculations indicate that small gradients occur when the surface temperature is low, or when the cylinder length and/or the length/radius ratio is small. Large values of the thermal conductivity of the cylinder material also leads to small gradients. Large values of surface temperature, length/radius ratio and small values of the thermal conductivity of the oxide and base material result in large gradients.

The model has been applied to calculation of temperature gradients for comparison with the experimental results obtained in sixty-five arc plasma tests on a variety of refractory materials. Ablators and oxide forming materials covering a wide range of thermophysical and oxidation characteristics, such as ZrB_2+SiC(A-8), ZrB_2(A-3), HfB_2+SiC(A-7), RVA (B-5), ZrB_2+SiC+C(A-10), WSi_2/W(G-18) and Hf-Ta-Mo(I-23) were included.

Observables consisted of the measured front face temperature T_f, the observed temperature at a distance, d mils from the front face, T(d), the cold wall heat flux, q, the stagnation enthalpy, i_e, and the stagnation pressure P_e. Additional input consisted of sample radius, R, length, L, and oxide coating thickness, I. The latter was equated to the conversion depth for the oxide formers (6). For WSi_2/W, I was equated to the WSi_2 coating thickness with I=0 for RVA(B-5) graphite which ablates without coating formation. Suitable values of the emittance, ϵ_S, and the thermal conductivities of the coating, k_F, and the substrate, k_S, were also employed.

The computed results are displayed in terms of the ratio of calculated front face temperature to observed front face temperature $T_f(CALC)/T_f(OBS)$ and the ratio of computed in-depth temperature $T_d(CALC)$ to computed front face temperature $T_f(CALC)$. The latter is compared with the ratio of observed in-depth temperature $T_d(OBS)$ to observed front face temperature $T_f(OBS)$. If agreement between calculated and observed temperatures results, $T_f(CALC)/T_f(OBS)$ would equal unity and the ratios $T_d(CALC)/T_f(CALC)$ and $T_d(OBS)/T_f(OBS)$ would coincide. Relatively good agreement was encountered as regards the latter comparison in view of the simple model employed to describe the complex tests. In addition, $T_f(CALC)/T_f(OBS)$ ratios were computed near unity for many of these tests. However, in line with the behavior noted above some systematic deviations were observed.

The largest of these occurred at low surface temperatures (i.e., $T_f < 3300^{o}R$) for the materials which form SiO_2 as an oxidation product. Thus, in cases where samples of HfB_2+SiC(A-7), ZrB_2+SiC(A-8), $ZrB_2+SiC+C$(A-10) or WSi_2/W(G-18) were exposed with shrouds or as large diameter hemispheres, $T_f(CALC)$ is considerably larger than $T_f(OBS)$. However, this difference is smaller than obtained when T_f is computed on the basis of front face radiation equilibrium alone. The cause of this behavior is presently unknown.

II. THE THERMAL RESPONSE OF REFRACTORY MATERIALS TO HOT GAS/COLD WALL EXPOSURES

A. Introduction

Prior to launching the extensive HG/CW testing program conducted under the present investigation, published data on the surface temperature of borides, graphites, graphite composites, silicon carbide, boron nitride, tungsten alloys and composites, refractory metal-oxide composites, coated refractory metals and iridium coated graphite exposed in arc plasma and Wave Superheater tests were collected. These data covered exposure conditions over a range of stagnation pressures between 0.002 and 70 atmospheres while Mach Numbers, stagnation enthalpy and heat flux levels ran from 0.2 to 8.5, 1400 to 18,000 BTU/lb and 20 to 4080 BTU/ft^{2}sec, respectively. The specimen configurations tested included flat face cylinders and hemispherical caps with diameters between 0.25 and 3.00 inches. The facilities at which these exposures were performed included Avco/SSD, Cornell Aeronautical Laboratory, General Electric Space Science Center, Plasmadyne Corporation, Cinncinati Testing Laboratory, North American Aviation Center, Grumman Aircraft Engineering Corporation and Aerospace Corporation. The results were compared with computed surface temperatures based on radiation equilibrium in order to estimate the current level of reliability of surface temperature predictions from stream conditions. A similar comparison of the results obtained in the present program (6) has been provided and is compared with the earlier results.

B. Compilation of Experimental Surface Temperatures and Stream Conditions

Since the present study is concerned with a comparison of CG/HW and HG/CW oxidation, correlation of the surface temperature of models (specimens) exposed under HG/CW conditions with specific stream characteristics is of paramount importance. In order to gain some insight into the relationship between the surface temperature and stagnation enthalpy, heat flux and pressure under subsonic and supersonic flow conditions, a review of available literature has been made. The results are contained in Tables 1-16 which identifies the material, Mach Number, stagnation pressure (P_e), enthalpy (i_e), cold wall heat flux (q_{cw}) and model configuration (D). As indicated, the diameter of cylindrical samples are designated by asterisks. In addition, the observed surface temperature, measured optically, is noted. Since the assignment of "observed temperature" is not performed uniformly in Tables 1-16, it is worthwhile to report the methods employed for each set of measurements. No attempt will be made at present to correct these "observed temperatures".

The ZrB_2, HfB_2 and HfB_2-SiC exposures reported under Reference (7) in Tables 1 and 2 were performed at Avco/SSD. Brightness temperatures were measured at $\lambda = 0.65$ microns and converted to "observed temperature" by using an emittance value of 0.60. Exposure times of five to thirty minutes were employed. The high pressure exposures of ZrB_2, Boride Z, ZrO_2, etc., shown under Reference (8) in Tables 2-8 were performed in the Cornell Wave Superheater. The former runs, as well as those in Tables 4-6 and 8 designated by Reference (11) (which were also carried out in the Wave Superheater), were given 15 second exposure times. In these cases, the brightness temperature at $\lambda = 2.1 \pm 0.5$ microns is reported. These temperatures represent mean values observed during exposure.

The graphite and tungsten exposures in Tables 7, 9, 12 and 13 denoted by Reference (10) were performed at Avco/SSD. These tests were of 60 to 120 seconds duration. Total emittance values were measured with an Eppley thermopile. In addition, brightness temperatures were measured at $\lambda = 0.65$ microns and converted to surface temperature by assuming that the emittance at $\lambda = 0.65$ microns is equal to the total emittance.

The results reported in Table 2 for tantalum (9) were obtained during 50-150 second exposures using an optical pyrometer at $\lambda = 2.1 \pm 0.4$ microns. Brightness temperatures were converted to observed temperatures by using an emittance of 0.45. The latter value was obtained from the observation of the melting point of Ta_2O_5 at 3730°R. The HfC-C (20) exposure time was 6 seconds. The temperature level of this CAL Wave Superheater test was established by observation of incipient melting of HfO_2 (Table 4).

The ATJ Graphite exposures denoted by Reference (12) were performed in the General Electric tandem Gerdien and free jet facilities (Table 10). The RVA graphite and graphite composites designated by Reference (13), Tables 11 and 12 were similarly tested. Exposure time was 60 to 1000 seconds and surface temperatures were measured with a two color pyrometer.

Exposure times of 100-1200 seconds were employed testing the JTA and ZrO_2 materials shown in Tables 13 and 14 designated by Reference (16). The reported surface temperatures are optical brightness temperature measured at $\lambda = 0.65\mu$. The same situation holds for the subsonic, one atmosphere exposures, shown in Tables 15 and 16 denoted by Reference (18) except that 30-60 second exposures were performed for the latter cases. Finally, the iridium coated graphite and JTA tests in Table 14 designated by Reference (17) were exposed for 400-1200 seconds. Temperatures were measured with a two color pyrometer.

C. Correlation of Results

Tables 1-16 provide a valuable empirical guide to estimating surface temperatures from specific stream conditions. However, it is desirable to provide a means for comparing results contained in Tables 1-6 which are related (i.e., cases where a given material is exposed to two slightly different stream conditions). In other terms, it would be useful to interpolate and extrapolate these in order to compare results obtained in different facilities and to predict the anticipated temperature for any given exposure.

The simplest means of performing such a correlation is to describe the conditions for radiation equilibrium at the stagnation point of the model on the assumption that the energy lost by radiation is equal to the heat transferred to the model. On this basis,

$$\sigma \epsilon T^4 = h_e(i_e - i_w[T, P_e]) \text{ BTU/ft}^2\text{sec} \quad (1)$$

where $\sigma = 0.47 \times 10^{-12}$ BTU/ft^{2}sec^{o}R^4, ϵ is the total hemispherical emittance, h_e is the stagnation point heat transfer coefficient, $i_e[T, P_e]$ is the stagnation enthalpy, and i_w is the enthalpy of air at the wall (surface) of the model and T^oR is the wall temperature. Eq. 1 usually ignores reactions at the model surface which give rise to significant evolution or absorption of energy and is as a result but a crude approximation to estimating the surface temperature which depends on a knowledge of h_e. If the cold wall heat flux, q_{cw}, is defined as

$$q_{cw} = h_e i_e \text{ BTU/ft}^2\text{sec} \quad (2)$$

then Eq. 1 becomes

$$\sigma \epsilon T^4 = q_{cw}(1 - i_w[T, P_e]/i_e) \quad (3)$$

Eq. 3 describes the wall temperature, T^oR as an explicit function of the stream parameters, i_e, q_{cw}, and the stagnation pressure P_e, as well as the enthalpy of air at the wall $i_w[T, P_e]$ and the total hemispherical emittance of the surface ϵ.

Numerical values of the enthalpy of air at the wall are given in Table 17. Specification of ϵ, q_{cw}, i_e and P_e fixes the surface temperature. Eq. 3 can be solved numerically by using the values of $i_w[T, P_e]$ shown in Table 17. However, it is convenient to represent $i_w[T, P_e]$ by analytic functions in order to obtain algebraic solutions. The following equations have been employed for this purpose:

$$i_w[T, P_e] \approx (T/1000)(100 + 45 \log P_e + (T/1000)(46 - 14 \log P_e)) \text{ BTU/lb} \quad (4)$$

and

$$i_w[T, P_e] \simeq 33.9\,(T/1000)^2 (2.0 - 0.13 \log P)\ \text{BTU/lb} \tag{5}$$

The numerical values of $i_w[T, P_e]$ described by Eq. 4 and Eq. 5 are compared with the established values of the enthalpy of air (21), (10) in Table 17. In the temperature and pressure range of interest (i.e., $2700^\circ < T < 7200^\circ R$ and $+2 > \log P_e \geq -2$), Eq. 4 represents a reasonably good representation of $i_w[T, P_e]$. Thus at pressures which are equal to or greater than 0.1 atm the difference between $i_w[T, P_e]$ and Eq. 4 are less than 200 BTU/lb. At 0.01 atm, larger differences are noted at 5400° and 6300°R. However, reference to Tables 1-16 shows that under low pressure testing conditions i_e is generally in the 5000-18,000 BTU/lb range. Under these circumstances, an error of 400 BTU/lb in $i_w[T, P_e]$ is not serious.

Eq. 5 is a poorer representation of $i_w[T, P_e]$. However, its simple quadratic form permits direct solution of Eq. 3 as follows:

$$0.47\epsilon\,(T/1000)^4 = q_{cw}\left(1 - 33.9\,(T/1000)^2 (2.0 - 0.13 \log P_e)/i_e\right) \tag{6}$$

hence

$$(T/1000)^4 + 33.9 q_{cw}(2.0 - 0.13 \log P_e)\,(0.47\epsilon i_e)^{-1}\,(T/1000)^2 - q_{cw}/0.47\epsilon = 0 \tag{7}$$

or

$$(T/1000)^2 = -0.5b + 0.5\,(b^2 - 4c)^{1/2} \tag{8}$$

where

$$b = 33.9 q_{cw}\,(2.0 - 0.13 \log P_e)\,(0.47\epsilon\, i_e)^{-1} \tag{9}$$

and

$$c = -q_{cw}/0.47\epsilon \tag{10}$$

Eqs 6-10 can be employed to obtain a crude estimate of the surface temperature at pressure equal to or less than 1 atm. At higher pressures, temperatures computed to be greater than 5400°R will be too low.

Eq. 3 has been employed to compute i_e for fixed values of q_{cw} and T at various stagnation pressures and emittance levels. These calculations were performed by using the established values of $i_w[T, P_e]$ given by Reference (10). The results are contained in Figures 1 to 15 and constitute exact solutions to Eq. 3.

Reference to Figures 1 to 15 illustrate the expected effect of the total emittance on surface temperature. Thus, under stream conditions corresponding to a cold wall heat flux of 200 BTU/ft²-sec, a stagnation pressure of one atmosphere and a stagnation enthalpy of 10,000 BTU/lb; a material having a total emittance of 0.2 would reach a surface temperature of 6200°R (Figure 6). Under the same conditions, a material having an emittance of 1.0 would reach a surface temperature of only 4400°R (Figure 10). These curves also show that with increasing stagnation enthalpy, the surface temperature is dependent only on heat flux and emittance as implied by Eq. 3 for $(i_w/i_e) \rightarrow$ zero. However, when the heat transfer coefficient is large, the temperature depends upon the stagnation enthalpy. In other terms, even under high flux conditions, the surface temperature cannot exceed the gas temperature. Note that in all of the proceeding discussions, heats of chemical reaction at the surface are ignored. Naturally, such effects could result in generation of surface temperatures which are in excess of stream temperatures. The inflections present in the $i_e[T]$ curves at log P_e = -2.0 (Figures 11-15) result from the temperature dependence of the enthalpy as indicated in Table 17.

Eq. 3 has been employed to compute the surface temperature for each of the exposures shown in Tables 1-16 by employing the representation of $i_w[T, P]$ given by Eq. 4. These calculations are performed on a computer using a Newton-Raphson technique to obtain solutions. The resultant ratio of computed temperature to observed temperature is contained in Tables 1-16. The ratio, T(CALC)/T(OBS), is plotted as a function of cold wall heat flux, q_{CW}, stagnation enthalpy, i_e, stagnation pressure, P_e, Mach Number and observed temperature in Figures 16-20. These calculations have been performed using a total hemispherical emittance of 0.6 for all exposures in Tables 1-16 except those in which emittance values were measured. In the latter cases, the reported values were employed.

An alternate calculation of the "Radiation Equilibrium" surface temperature can be performed which employs the Fay-Riddell relation (22) to compute the heat transfer coefficient, h_c. This procedure is performed by setting

$$h_e = 0.94 \left(\frac{2R_B}{u_\infty} \frac{du_e}{dx} \right)^{1/2} \left(\frac{(\rho\mu)_e u_\infty}{2R_B} \right)^{1/2} \left(\frac{(\rho\mu)_w}{(\rho\mu)_e} \right)^{1/10} \quad \text{lbs/ft}^2\text{sec} \tag{11}$$

Letting

$$\left(\frac{2R_B}{u_\infty} \frac{du_e}{dx} \right) = Q \tag{12}$$

for convenience and noting that

$$Q^2 = \frac{8\,((\gamma-1)\,M^2+2)}{(\gamma+1)\,M^2}\left[1+\frac{(\gamma-1)}{2}\,\frac{((\gamma-1)\,M^2+2))}{(2\gamma M^2-(\gamma-1))}\right]^{-\frac{1}{\gamma-1}} \tag{13}$$

for Mach Numbers greater than one, and

$$Q^2 = 9 \tag{14}$$

for Mach Number = 0, where $\gamma = C_p/C_v = 1.4$ for an ideal gas, and M is the Mach Number. Approximating

$$((\rho\mu)_w / (\rho\mu)_e)^{1/10} = 1 \tag{15}$$

yields

$$h_e = 0.94Q^{1/2}\,((\rho\mu)_e\, u_\infty /2RB)^{1/2} \tag{16}$$

Eq. 16 can be evaluated by estimating the viscosity by (23, 24) the following:

$$\mu = 2.17 \times 10^{-8}\, T^{1/2} \quad \frac{\text{lbs (force) sec}}{\text{ft}^2} \tag{17}$$

Setting $P = \rho RT$ and $R = 1724\ \text{ft}^2/\text{sec}^2\ {}^\circ R$ and noting that

$$(T_e/T_\infty) = 1 + 0.5\,(\gamma-1)\,M^2 \tag{18}$$

with $M^2 = u_\infty^2/\gamma RT_\infty$ yields

$$h_e = 0.94Q^{1/2}\left[1.09\times10^{-8}\,\frac{(\text{lbs (force) sec})}{\text{ft}^2\ {}^\circ R^{1/2}}\,(\gamma/R)^{1/2} M(1+0.5(\gamma-1)M^2)^{-1/2}\right]^{1/2}(P_e/R_B)^{1/2} \tag{19}$$

Also for high Mach Numbers ($M >> 1$), $Q = 1.11$ and

$$h_e = 0.99\,(6.90 \times 10^{-10})^{1/2}\,(P_e/R_B)^{1/2}\ \text{lbs (force) sec/ft}^3 \tag{20}$$

where P_e is in lbs (force)/ft^2 and R_B is in feet. Thus

$$h_e = 2.60 \times 10^{-5} (P_e/R_B)^{1/2} \text{ lbs (force) sec/ft}^3 \qquad (21)$$

(lbs (force) = 32.2 lbs ft/sec^2). Hence

$$h_e = 8.37 \times 10^{-4} (P_e/R_B)^{1/2} \text{ lbs/ft}^2\text{sec} \qquad (22)$$

When the stagnation pressure is in atmospheres. (1 atm = 2117 lbs (force)/ft^2)

$$h_e = 0.0386 (P_e/R_B)^{1/2} \text{ lbs/ft}^2\text{sec} \qquad (23)$$

Eq. 23 is a reduced Fay-Riddell relation applicable at high Mach Numbers. The general relation given above in Eq. 19 is

$$h_e = 0.0245Q^{1/2} [M^2(1 + 0.5 (\gamma - 1) M^2)^{-1}]^{1/4} (P_e/R_B)^{1/2} \text{ lbs/ft}^2\text{sec} \qquad (24)$$

where P is in atmosphere and R_B in feet. If the quantity $0.0245Q^{1/2}[1 + 0.5 (\gamma - 1) M^2)^{-1}]^{1/4}$ is approximated by $0.0386/(1 + 0.17M^{-1})$, which is accurate to within 5% for $M > 0.1$, then Eq. 24 becomes

$$h_e = 0.0386 (1 + 0.17M^{-1})^{-1} (P_e/R_B)^{1/2} \text{ lbs/ft}^2\text{sec} \qquad (25)$$

Substitution into Eq. 1 yields

$$\sigma\epsilon T^4 = 0.0386 (1 + 0.17M^{-1})^{-1} (24 P_e/D)^{1/2} (i_e - i_w[T, P_e]) \qquad (26)$$

where D is the diameter of the hemispherical cap in inches.

Eq. 26 has also been applied to compute the radiation equilibrium temperature for all of the exposures in Tables 1-16 by employing the description of $i_w[T, P_e]$ afforded by Eq. 4. These calculations were performed for flat faced cylinders by setting

$$D = 2.5 \text{ Diameter of Cylinder} \qquad (27)$$

in Eq. 26 in order to account for the difference in heat transfer between hemispherical caps and flat faced cylinders. The stagnation point heat flux to a flat faced cylinder having a diameter D_c is equivalent to the heat transfer to a hemisphere having an effective diameter, D_{eff}, equal to fD_c. The values of f noted in the literature are 2.1 (25), 2.5 (12) and 2.9 (12). In addition, the following numerical values of f have been reported: 2.0 (26), 3.2 (26), 3.3 (27) and 3.08, 3.34 and 3.72 at Mach Number 2.0, 3.0 and 4.76, respectively (28). Thus it appears that values of $2.0 \leq f \leq 3.72$ have been employed for relating flat faced cylinders to hemispheres. As indicated above, a value of 2.5 is currently being employed in the present calculations (Eq. 27). This variation may result from individual facility characteristics and measurement techniques. For example, the value f = 2.0 (26) has a heat transfer basis while f = 3.2 (26) has a pressure gradient basis. All of the remaining values except 2.1 (25) were obtained experimentally.

The results of applying Eq. 26 contained in Tables 1-16 under the heading "Fay-Riddell" are displayed in Figure 21 which shows the ratio T(CALC)/T(OBS) vs. the observed cold wall heat flux.

D. Discussion of Results

Examination of Tables 1-16 and Figures 16-21 shows the wide divergence between observed and calculated temperatures. Although it is presently impossible to define the causes of these discrepancies, some of the possibilities are worthwhile noting. To begin with, the exposure times for the tests under consideration are variable. Thus the Avco-MeB_2 and HfB_2 + SiC; the Plasmadyne-ZrO_2 and JTA; the General Electric ATJ, RVA and JTA; and the Cincinnati Testing Laboratory JTA and Ir coated graphite exposures were of 100-1800 seconds duration. The remaining tests were for 30-60 seconds with the exception of the CAL exposures which were limited to 15 seconds. Under these conditions, it might be expected that radiation equilibrium is more readily attained in the long time exposures (i.e., times greater than 100 seconds). Thus, the observed temperature in a short time exposure would be lower than the calculated radiation equilibrium temperature.

A second major source of error is the measurement of surface temperature. This depends upon the particular value of spectral emissivity employed in correcting the observed brightness (ϵ = 1) to the true temperature. For the G.E. and CTL results, obtained with a two color pyrometer, the error in assigning a true surface temperature depends upon how well grey body conditions are approximated. Although these temperature measurement errors can be significant, it is not likely that they are the prime source of the present discrepancies in the T(CALC/OBS) ratios. A related source of error is the value of total emittance used in computing the temperature in Eq. 3. As indicated earlier, measured values have been employed where available. Where no values are available, a mean value of 0.6 has been employed. If the true value of total emittance is 1.0, then the calculated temperature will be too high by the one fourth root of (1/0.6) or fourteen percent. Such corrections could improve the present results. However, such changes would not eliminate the current level of disagreement between observed and calculated temperature.

The relative sizes of the model and the arc are an additional variable which has not been considered in the analysis. Table 13 contains the results obtained during the exposure of silicide coated refractory metal alloy foil. In these experiments, the arc diameter was about one inch and the model was a two inch square foil. The foil radiated from both the front and back face. As a result, the ratio of T(CALC)/T(OBS) is much larger than unity. These ratios are not included in Figures 16-21.

Comparison of the T(CALC)/T(OBS) values shown in Tables 1-16 for the "Cold Wall" and "Fay-Riddell" Heat Transfer Coefficient computations indicate that in some cases substantial differences exist between these heat transfer coefficients. Thus, the "Cold Wall" and "Fay-Riddell" heat transfer coefficients differ markedly in the data generated at Avco and CTL. There is some evidence that this may be due to turbulent test streams (29). On the other hand, the CAL, General Electric, Aerospace Corp., Plasmadyne, North American and Grumman data show good correlation between the "Cold Wall" and "Fay-Riddell" values. Reference to Figure 21 shows that the ratio of T(CALC)/T(OBS) is poorer for the "Fay-Riddell" calculation than for the "Cold Wall" calculation.

As previously indicated, the present calculations ignore heat liberated at the surface due to oxide formation or heat absorbed by the surface in order to vaporize or melt the model material. Inclusion of the former effects could raise the present values of T(CALC)/T(OBS) while inclusion of the latter would lower the current T(CALC)/T(OBS) ratios. Although these effects can be substantial, they do not appear to be the source of the current differences. Inclusion of the heats of combustion would raise T(CALC) and further aggravate the T(CALC)/T(OBS) ratios. Moreover, reference to Figure 20 shows that the largest deviations from T(CALC)/T(OBS) = 1, occur below 5000°R where copious vaporization of the materials under consideration is unlikely.

The most important (and unfortunately the least tractable) sources of error are the reported values of the stagnation enthalpy and cold wall heat flux. Nonuniform flux and enthalpy conditions in addition to gas radiation losses and variation in the techniques employed for the measurement of these quantities is probably the most important single source of the deviation of T(CALC)/T(OBS) from unity in Figures 16-21. Thus, comparison of theAvco (half-filled squares) and General Electric (rimmed squares) results for ATJ graphite shows an extremely large discrepancy. The Avco data yield values of T(CALC)/T(OBS) which fall between 1.10 and 1.18 based on observed "Cold Wall" heat transfer coefficients while the General Electric results for the same material range from 1.13 to 2.05. It should be pointed out that the latter results were obtained for long time exposures.

Apart from the General Electric data, values of T(CALC)/(OBS) which differ from 1.0 + 0.2 are frequent in the Aerospace and CAL exposures. As indicated earlier, these exposures were for short times and the high values may be due to the fact that radiation equilibrium was not established.

E. Results Obtained during the Present Testing Program

In the course of the present program, more than 700 arc plasma tests were performed (6). Measurements of stagnation enthalpy, stagnation pressure, cold wall heat flux and brightness temperature were performed in each case. The latter were converted to true temperature by using the measured values of the emittance for the candidate materials (5) under oxidizing conditions. In addition, radiated heat flux was also measured in these tests so that normal emittance, ϵ_N, could be deduced (6). Table 18 summarizes the average values of ϵ_N and the T(CALC)/T(OBS) ratios for each of the materials tested (6). The latter ratio is computed on the basis of Eqs. 3 and 4 corresponding to radiation equilibria.

Ideally, if radiation equilibria were the dominant factors and all measurements were accurate, these ratios should be unity. Although there are departures, it is satisfying to note that the differences are small compared to those obtained by considering the results of other studies (i.e., Figures 16-21 and Tables 1-16). Reference to Table 18 shows that ratios of T(CALC)/T(OBS) are lower for cases where melting is observed than for cases where a solid oxide (or coating) is present. Moreover, Table 18 shows that large values of T(CALC)/T(OBS) are characteristic for some of the materials. The occurrence of ratios which are larger than unity implies resistance to energy absorption by the material. Thus, exposure of HfB_2 + SiC(A-4) and HfC + C(C-11) to identical stream conditions (i.e., stagnation pressure, enthalpy and cold wall heat flux) would result in an 11% lower surface temperature than that reached by HfC + C(C-11). This conclusion would apply if stream conditions were not sufficient to produce melting of HfB_2 + SiC(A-4). At lower levels, KT-SiC(E-14), WSi_2/W(G-18) and Sn-Al/Ta-10W(G-19), which exhibit T(CALC)/T(OBS) ratios of 1.43, 1.56 and 1.41, respectively demonstrate similar resistance to energy transfer. Although the origin of this resistance is not clear at present, it is probably due to blocking effects caused by evolution of gaseous oxides. These observations suggest a method of ranking the behavior of the refractory materials which differs from the customary recession vs. temperature curves. In Section IV, an alternative method of presentation which compares recession rate as a function of heat flux and enthalpy for the candidate materials is considered. This method does not require a knowledge of the spectral or the normal emittance and integrates the blocking effects characteristic of each material.

III. SIMPLIFIED MODEL FOR CALCULATING THE OXIDATION BEHAVIOR OF GRAPHITE UNDER HIGH VELOCITY AIR FLOW CONDITIONS

A. Introduction and Summary

In the course of the present study, the oxidation of graphites in air has been investigated experimentally over a range of conditions (4-6) between 2500°R and 6500°R, at velocities between 1 ft/sec and Mach 3.2. Additional studies (12), (13) have been performed. The succeeding volume of this series (30) presents a complete discussion of the surface reaction problem encountered in the oxidation of graphite. This discussion considers the coupling of mass transport through the boundary layer with reactions at the surface in detail (30). By contrast, the discussion presented below employs simplified models (7, 31-33) which provide an explicit means for computing the rate of graphite recession as a function of density, surface temperature, gas velocity, stagnation pressure and sample radius. The results are compared with observations covering a range of density between 80 and 115 lbs/ft^3, temperatures between 2500° and 6500°R, velocities between 1 ft/sec and Mach 8.0, stagnation pressures between 0.007 and 1.0 atm and nose radii between 0.005 and 0.07 ft.

B. Derivation of the Simplified Model for Graphite Oxidation

Comparison of the recession rates observed for graphite in the present study at air flow rates between 1 ft/sec and 250 ft/sec (Figure 37 and pp 23-29 of reference 5) demonstrate that most (if not all) of the graphite oxidation data previously determined (34, 35) is controlled by a supply limit. Thus, for example, Eqs. 28 (Gulbransen et al. (34)) corresponds to a recession rate of

$$\dot{m} = 1.86 \times 10^{-6} P_{O_2}^{0.32} e^{-3600/RT} \quad \text{gm/cm}^2\text{sec} \tag{28}$$

where P_{O_2} is in torr and T is in °K, and

$$\dot{S} = 2.44 \times 10^{-2} P_{O_2}^{0.32} e^{-3600/RT} \quad \text{mils/min}$$

for graphite with a density $\rho = 1.80$ gms/cm^3 or 112 lbs/ft^3. For air, P_{O_2} = 160 , thus Eq. 28 yields a rate of 0.0007 mils/sec at 3000°R. This compares with values near 0.1 mils/sec at a flow rate of 1 ft/sec and 1 mil/sec at 250 ft/sec observed in the current study (5, Figure 37). The oxidation rates reported by Okada and Ikeqawa (35) between 1800°R and 5400°R under slow flow conditions at a pressure of 0.21 atm O_2 yield similar comparisons. Values corresponding to 0.02, 0.07 and 0.10 mils/sec are reported (35) at temperatures of 2000°R, 3000°R and 4000°R, respectively. As indicated (5), transport of sufficient quantities of oxygen to the reacting surface and a knowledge of the oxygen partial pressure at the reacting surface are required in order to make any measurement meaningful. Theoretical studies along these lines are presented in reference (30) in order to calculate concentration gradients present in the gaseous boundary layer adjacent to the reaction surface. However, since the details of this treatment are quite complex it is instructive to consider the approximate treatment described earlier (Eq. 15 p. 242, Reference (7)).

The correct picture for the oxidation of graphite above 800°C (1472°F) is one of continually increasing rate with both temperature and oxygen pressure according to the Arrhenius relationship:

$$\dot{m} = kP^z e^{-E/RT} \tag{29}$$

From 800° to 2065°C (1472°-3750°F) $z = 0.32$-0.38 and $E = 3600$-4200 cal/mol based on results of Gulbransen (34) and this study on Speer 710 and RVA graphites (5). Although the activation energies observed in the present study (5) are comparable to those reported by Gulbransen et al., the rates are much higher in the present investigation. Thus, for P_{O_2} = 150 torr, at T = 1700°F, Eq. 28 yields a rate of about 0.04 mils/minute. The present study indicates 60 mils/minute at 250 fps. Eq. 28 converts to

$$\dot{m} = 3.16 \times 10^{-5} P_{O_2}^{0.32} e^{-3600/RT} \quad \text{lbs/ft}^2\text{sec} \tag{30}$$

where P_{O_2} is in atmospheres and T is in °K, and

$$\dot{S} = 3.39 \times 10^{-3} P_{O_2}^{0.32} e^{-3600/RT} \quad \text{mils/sec} \tag{31}$$

for graphite with a density $\rho = 1.80$ gms/cm³ or 112 lbs/ft³. These reaction kinetic equations are altered (7) to reflect diffusion control (31) yielding

$$\dot{m} = k(C_{O_{2},e} M/M_{O_2})^z P_e^z (1-m/m_D)^z e^{-E/RT} \text{ lbs/ft}^2\text{sec} \tag{32}$$

where P_e is the stagnation pressure and $C_{O_2,e}$ is the mass fraction of oxygen at the edge of the boundary layer.

If one considers the reaction

$$C + 1/2O_2 + 2N_2 \rightarrow CO + 2N_2 \tag{33}$$

as dominant, then M = 28.5, M_{O_2} = 32 and $C_{O_2,e}$ = 0.21. In addition (7, 32)

$$\dot{m}_D = 0.006 \, (P_e/R_B)^{1/2} \ \mathrm{lbs/ft^2 sec} \tag{34}$$

Thus, Eq. 32 describes the oxidation of graphite in terms of an Arrhenius term ($ke^{-E/RT}$) and a pressure correction term ($1-\dot{m}/\dot{m}_D$) which is based on a diffusion limit $\dot{m}_D$ given by Eq. 34. In other terms, the ($1-\dot{m}/\dot{m}_D$) coefficient can be considered as a pressure correction which relates the oxygen concentration at the edge of the boundary layer to that at the graphite surface. Divergent values have been reported for the Arrhenius constants k and E (5). Part of the difficulty undoubtedly arises from the fact that CO_2 is the dominant product gas of graphite oxidation at low temperature while CO dominates at high temperature (36). In contrast to the values $k = 3.16 \times 10^{-5}$ and $E = 3600$ implied by Eq. 30, Scala and Gilbert (32) have proposed $k = 6.729 \times 10^8$ and $E = 44,000$ for "fast kinetics" and $k = 4.473 \times 10^4$ and $E = 42,300$ for "slow kinetics". The current results indicate that lower values of the activation energy may be more appropriate (5).

As indicated below the results of the present study (5, 30) have been examined in order to obtain the most appropriate values of k and E. To begin with, Eq. 34 was re-examined in order to allow for air flow rate effects at subsonic velocities since the diffusion limited rate for carbon removal, $\dot{m}_{KD}$, was originally approximated by (7)

$$\dot{m}_{KD} = A(P_e/R_B)^{1/2} C_K \tag{35}$$

where C_K is the mass fraction of carbon in the oxidation reaction. Since the average molecular weight in Eq. 33 is 25.8 (with $M_{O_2} = 32$) then $C_K = 1/7$. The coefficient "A" was estimated by analogy with the Fay-Riddell relation (22, 27)

$$q = 0.042 \, (P_e/R_B)^{1/2} (i_e - i_w) \tag{36}$$

where the enthalpy difference ($i_e - i_w$) is the analog of C_K in the mass loss relation. Thus, with $A = 0.042$, $\dot{m}_D$ is defined by Eq. 34. However, at low velocities a Mach Number correction (of Eq. 25) is required and the result yields (30)

$$\dot{m}_D = 0.0072 \, (1 + 0.17M^{-1})^{-1} (P_e/R_B)^{1/2} \ \mathrm{lbs/ft^2 sec} \tag{37}$$

with

$$\dot{m} = 0.74 \, P_{O_2}^{1/3} \, e^{-10,730/RT} \ \ \mathrm{lbs/ft^2 sec} \tag{38}$$

for the reaction rate, then

$$\dot{m} = (0.170)^{1/3} \left[1 - \dot{m}(R_B)^{1/2} / 0.0072 \, (1 + 0.17M^{-1})^{-1} \, P_e^{1/2} \right]^{1/3}$$

$$\text{times } 0.74 \, e^{-10,730/RT} \quad \text{lbs/ft}^2\text{sec} \tag{39}$$

where R_B is the body radius in feet. Since

$$\dot{S} \text{ (mils/sec)} = \dot{m} \text{ (lbs/ft}^2\text{sec) } 12000/\rho \text{ (lbs/ft}^3\text{)} \tag{40}$$

Hence

$$\dot{S} = 4920\rho^{-1} P_e^{1/3} \exp(-9720/T) \left[1 - \frac{0.0116\rho \dot{S} R_B^{1/2} P_e^{-1/2}}{(1 + 0.17M^{-1})^{-1}} \right]^{1/3} \quad \text{mils/sec} \tag{41}$$

for the carbon recession rate in air, where ρ is the density of graphite in lbs/ft^3 and T is in ^{o}R. The activation energy and pre-exponential factor in Eq. 38 were evaluated by employing the form of Eq. 41 and the data in Table 19 in order to obtain the best fit.

The experimental results shown in Table 19 include results for ATJ, RVA(B-5), PT0178(B-9) and Poco Graphite (B-10). The calculations refer to flat faced cylinders ($R_B = 2.5 \, R_c$) exposed during the present study by R. A. Tanzilli (13), and by Metzger et al. (12). Exposures performed in the current study are designated by run numbers (6). Tanzilli's exposures of PT0178(B-9) are designated by B9-Gel-18 in Table 19. The exposures of ATJ graphite by Metzger et al. are denoted by MED. In addition to these arc plasma exposures, calculations were performed for serveral high velocity CG/HW tests conducted on RVA(B-5) (5). Exposure B5-L2, B5-L3 and B5-L4 were taken to represent the results contained in Figure 45 of (5) at 200 ft/sec. Examination of the samples after exposure indicates a nose radius equal to one sixteenth of an inch as shown in Figure 44 of (5), hence R_B = 62 mils or 0.0052 ft. The data and calculations cover temperatures between 2300° and 6500°R. Thus, it is possible that some of the high temperature points (T > 6000°R) reflect recession via diffusion limited vaporization where the observed values would be expected to exceed Eq. 41 since vaporization becomes a significant factor in the recession rate above 6000°R at one atmosphere. The present data cover the pressure range between 0.007 and 1 atmosphere and represent RVA(B-5), PT0179(B-9) and Poco(B-10) graphite. Moreover, the results include data generated in the HG/CW Avco Model 500 and ROVERS facilities (3) and the General Electric Tandem Gerdien Arc as well as the Lockheed M/S Co., CG/HW facility (2).

In addition, it should be pointed out that an independent experimental arc plasma study by Sallis et al. (37) between 2500° and 5000°R at stagnation pressures between 0.1 and 9 atmospheres yields a pre-exponential of 3.0 and an activation energy of 15,500 cal/mole as compared with the current results of 0.74 and 10,730 cal/mole shown in Eq. 28. In addition, Sallis et al. suggest that the exponent of the oxygen pressure is 0.4 rather than the value of 0.333 indicated by Eq. 38.

Eq. 41 has been employed to generate Figures 22-26, which compare with the observed and computed results of graphite oxidation at low velocities. Figure 22 shows excellent agreement for RVA(B-5) at 3310°R (Figure 37 of reference 5), while Figure 23 shows qualitative agreement (see Figure 45 of reference 5). While it is apparent that Eq. 41 provides an excellent description for the oxidation kinetics of graphite over a very wide range of conditions shown in Table 19, it is of interest to consider the results of a different kind of experiment relative to the predictions of Eq. 41.

Blyholder and Eyring (38) have measured the oxidation of graphite in flowing oxygen at 800°K. The oxygen pressure employed was 26 microns of mercury while the flow rate was 1000 cm/sec. The samples employed in this experiment were hollow cylinders of carbon having a density of 1.3 gms/cm^3 (81 lbs/ft^3) which were 1/4 inch in diameter with a one millimeter wall thickness. The samples were cut in half parallel to their longitudinal axes prior to exposure. Under these conditions, the oxidation rate of carbon (as measured by formation of CO) corresponded to 16×10^{15} molecules of $CO/cm^2 sec$. This corresponds to 3.2×10^{-6} gms of $carbon/cm^2 sec$. In order to apply Eq. 41 to compute the rate of carbon oxidation for comparison with this result is is necessary to estimate the value of the term within the braces in Eq. 41 first. Since the flow rate was 1000 cm/sec or about 33 ft/sec, M is approximately 0.03. The corresponding value of P_e is equal to 3.4×10^{-5} atm. (26μ of Hg) multiplied by (1.00/0.21) or 160×10^{-6} atm. Estimating $R_B = 2.5\ R_C$ leads to $R_B = 0.026$ ft. Thus, Eq. 41 becomes

$$\dot{S} = 3.85 \times 10^{-3} (1 - 80\dot{S})^{1/3} \quad \text{mils/sec} \tag{42}$$

or $\dot{S} = 3.4 \times 10^{-3}$ mils/sec $= 8.6 \times 10^{-6}$ cm/sec $= 11.2 \times 10^{-6}$ $gms/cm^2 sec$. This value is in good agreement with the observed value of 3.2×10^{-6} $gm/cm^2 sec$ in view of the estimates required for R_B and M. Moreover, this experiment was performed far from the range of conditions employed to fix the pre-exponential and activation energy in Eq. 38.

C. Comparison of the Scala-Gilbert and John-Schick Models for Graphite Ablation

John and Schick (33) have developed a theory for describing the diffusion controlled ablation of graphite which defines the linear recession rate, $\dot{S}$(mils/sec), of graphite as follows:

$$\dot{S} = 12,000 q_{HW} \rho^{-1} (i_e - i_w)^{-1} \left[\frac{M_{O_2}}{2 M_C C_{O_2}} + \eta \right]^{-1} \text{ mils/sec} \quad (43)$$

where ρ is the density of the graphite (lbs/ft^3), i_e(BTU/lb) is the stagnation enthalpy, i_w(BTU/lb) is the enthalpy at the wall, $M_{O_2} = 32$ and $M_C = 12$ are the molecular weights of oxygen and carbon, $C_{O_2} = 0.21$ is the mass fraction of oxygen in air, η is a blowing factor, and q_{HW} is the hot wall heat flux. If we set $\eta = 0.67$, which is the usual value, and

$$\frac{q_{cw}}{i_e} = \frac{q_{HW}}{(i_e - i_w)} \quad (44)$$

Then Eq. 43 becomes

$$\dot{S} = 12,000 \rho^{-1} (q_{cw}/i_e) 7^{-1} \text{ mils/sec} \quad (45)$$

or

$$\dot{m} = h_e (7)^{-1} \text{ lbs/ft}^2\text{sec} \quad (45)$$

where h_e is the heat transfer coefficient. Setting

$$h_e = 0.042 (P_e/R_B)^{1/2} \quad (47)$$

based on the Fay-Riddell relation at high Mach Numbers yields

$$\dot{m} = 0.006 (P_e/R_B)^{1/2} \text{ lbs/ft}^2\text{sec} \quad (48)$$

Eq. 48 is identical to the result obtained by Scala and Gilbert (32) in the diffusion limited range. Thus, it is apparent that

(John-Schick Model) + (Fay-Riddell Model) = (Scala-Gilbert Model) (49)

IV. INFLUENCE OF FLUX-ENTHALPY AND ALTITUDE-VELOCITY VARIABLES ON THE RECESSION OF REFRACTORY MATERIALS

Figures 1-8 of reference (6) describe the 30 minute recession or oxidation depths observed for the candidate materials in HG/CW arc plasma tests and in CG/HW furnace tests as a function of surface temperature. In the former case, the surface temperature is a result of the interaction of the material with the stream. Thus, while comparison of a given material in the CG/HW and HG/CW cases based upon results at a given temperature is quite legitimate, evaluation of various materials in HG/CW tests on solely a temperature basis is not complete. As indicated earlier (6) factors such as emittance, oxidation products and surface characteristics can lead to situations where identical stream conditions produce a variety of surface temperatures on different materials even after long exposure times. In order to consider an alternative method for comparison of the oxidation characteristics and to relate the HG/CW tests to flight parameters, an additional description can be employed.

Figure 27 shows the stagnation pressure as a function of altitude and velocity. In addition, stagnation heat flux to a one inch sphere described as a function of altitude and velocity is displayed. In essence, these curves provide a means for relating the HG/CW arc plasma tests to flight trajectory conditions. The relations are presented for the case of a one inch radius sphere. Since the heat flux is proportional to $R^{-1/2}$, the heat flux to a 4 inch sphere would be one half of the values shown on the ordinate of Figure 27, while the heat flux to a 1/4 inch sphere would be twice those shown in Figure 27. The curves relating stagnation pressure, P_e, altitude, A, and velocity, V, in Figure 27 are the results of complex equations (39-41). However, between 50 Kilo feet and 250 Kilo feet, these curves can be represented simply by Eq. 50 as:

$$P_e = V^2 (1 + (A/216)^4)\, 10^{-A/54} \text{ atm} \tag{50}$$

where P_e is the stagnation pressure behind a normal shock in atmospheres, V is the velocity in kilo feet/sec and A is the altitude in kilo feet. The stagnation enthalpy, i_e, is approximately

$$i_e = 20V^2 \text{ BTU/lb} \tag{51}$$

Eqs. 50 and 51 when coupled with the Fay-Riddell relation for a hemisphere

$$q = 0.042\, i_e (P_e/R_B)^{1/2} \text{ BTU/ft}^2\text{sec} \tag{52}$$

where R_B is the body radius in feet yields

$$q = 2.9V^3 (1 + (A/216)^4)^{1/2} R_B^{-1/2} 10^{-A/108} \tag{53}$$

where R_B is the body radius in inches.

Thus, Figure 27, or the approximations afforded by Eqs. 50-53 permit direct conversion from altitude-velocity space to flux-enthalpy space for a hemisphere. As indicated above, the behavior of the refractory materials of interest under HG/CW conditions simulating high velocity atmosphere flight is presented in Figures 1-8 of reference 6. The latter show material recession as a function of stagnation pressure and surface temperature. In this case, the surface temperature results from a combination of q, i_e and material reactions with the stream. The relations between q, i_e, P_e and surface temperature (for radiation equilibrium) is illustrated in Figures 1 to 15. Calculations of this type have been performed for each HG/CW exposure (6). Although reasonable agreement of computed $T[i_e, q, P_e]$ with observed surface temperature has been encountered, some systematic differences have been noted as shown in Table 18. Specifically, SiC and SiC bearing composites reach lower surface temperatures for given i_e, q and P_e conditions than do the other materials considered. Similar behavior is noted for WSi_2/W and SnAl/Ta-10W under conditions where the coatings do not fail.

An alternative method for describing the performance of these refractory materials is illustrated in Figures 28-36. These figures show heat flux as the ordinate and stagnation enthalpy as the abscissa. In addition, velocity as related to stagnation enthalpy by Eq. 51 is shown as the abscissa. Moreover, the relationship for a one inch radius sphere at 150 kilo feet is the ordinate. Thus, for a velocity of 16 kft/sec at an altitude of 150 kft, the stagnation enthalpy would be approximately 5100 BTU/lb and the stagnation heat flux to a one inch radius sphere would be about 600 BTU/ft^{2}sec. If the body radius were 4", the heat flux would be 300 BTU/ft^{2}sec (located by dropping down to 300 on the inner ordinate scale). Conversely, if the body radius were 1/4", the heat flux would be 1200 BTU/ft^{2}sec (located by moving up to 1200 on the inner ordinate scale). Thus, the double set of ordinate and abscissa scales permit direct translation of velocity and body radius to flux altitudes, Eq. 53 has been employed to construct the inserted curve shown on each graph which shows the ratio of q[Altitude] / q[150 kft] as a function of altitude. This ratio is 0.27, 0.48, 1.00, 2.46 and 6.85 at 250, 200, 150, 100 and 50 kft, respectively. Thus, at a velocity of 16 kft/sec and 250 kft altitude, the heat flux to a one inch sphere would be 600 x 0.27 or 162 BTU/ft^{2}sec. Under these conditions a 4" radius would experience a heat flux of 81 BTU/ft^{2}sec while a 1/4" radius sphere would be exposed to a heat flux of 324 BTU/ft^{2}sec. Similarly at an altitude of 50 kft, the heat flux to a one inch radius sphere would be 2.46 x 600 = 1476 BTU/ft^{2}sec and the flux to a 4" and 1/4" sphere would be 738 and 2952 BTU/ft^{2}sec, respectively.

Thus, Figures 28-36 show heat flux and enthalpy for any velocity, altitude and body radius. Figure 28 shows the recession rates observed for hafnium diboride at stagnation pressures of one atmosphere (circles) and 0.01-0.1 atmospheres (squares). Recession rates which are less than 0.1 mils/sec, between 0.1 and 1 mil/sec and more than one mil/sec are indicated by open, half-filled and filled points, respectively. Recession rates are plotted at flux and enthalpy co-ordinates for exposures given in reference 6. At present, sufficient data are not available to construct boundaries representing constant recession levels over the entire flux-enthalpy space. To bridge the gap, 1.0 mil/sec boundaries are approximated at each pressure by temperature levels obtained from Figures 1-15. Figure 36 summarizes all of the results for a 1 mil/sec boundary at one atmosphere.

The hyperbolic curves for all of the materials except graphites and tungsten, define the flux-enthalpy (or velocity-altitude-body radius) conditions where the recession rate exceeds 1 mil/sec. Flux-enthalpy conditions below and to the left of these boundaries result in recession rates which are less than 1 mil/sec. Flux-enthalpy conditions above and to the right of these boundaries yield recession rates in excess of 1 mil/sec. In the case of graphites and tungsten, the linear boundaries (based on diffusion limits) are shown for 0.5, 1.0, 2.0 and 4.0 mils/sec. Flux-enthalpy conditions lying below and to the right of these boundaries will result in lower recession rates, while those lying above and to the left will result in higher rates. The computed rates for graphite and tungsten are calculated on the basis of Reference 31 and Eq. 45.

Although Figure 36 is based on a limited number of tests, it provides a clear indication of the superiority of SiC and SiC composites. Figure 1 of reference 6 suggests that ZrB_2(A-3) exhibits recession rates below 1 mil/sec at surface temperatures up to 5000°F. Figure 5 of Reference 6 shows that KT-SiC(E-14) exhibits rates below 1 mil/sec or less below 4000°F. However, Table 18 as well as Figure 36 indicate that the flux-enthalpy conditions which produce 5000°F surface temperature (and a 1 mil/sec recession rate) for ZrB_2(A-3) will yield a surface temperature of only 4000°F (and a comparable recession rate) for KT-SiC(E-14). Of course, relative mechanical properties, thermal shock resistance, density and other factors may impose additional criteria for comparison. Nevertheless, Figure 36 presents a direct ranking of oxidation behavior as a function of flight conditions for extended periods of time at the stagnation point. The position of these curves could vary with stagnation pressure. There are several other inversions of rank relative to the CG/HW and HG/CW tests using temperature as a base. Figures 42 and 45 of reference 6 show that HfB_2 + SiC(A-4) and (A-7) exhibit 1 mil/sec recession rates at lower temperatures than HfC + C(C-11). Nevertheless, for given stream conditions, the latter reaches surface temperatures which are 20% higher than the former (see Table 18) and ranks lower in Figure 36. Similarly, SiO_2 + W(H-22) and Si/RVC(B-8) which degrade rapidly at 4000°F and 3100°F respectively in CG/HW furnace tests rank high on the basis of Figure 36. The relative behavior of Si/RVC(B-8) and Ir/C(I-24) is also illustrated graphically in Figure 36. Reference to Figures 5 and 8 of reference 6 shows that Si/RVC(B-8) provides protection for graphite at surface temperatures up to 3700°F in the HG/CW arc plasma tests while Ir/C(I-24) is protective up to surface temperatures of 4200°F. However, since the latter has an emittance of 0.3 and T(CALC)/T(OBS) = 1.16 (Table 18) while the former has an emittance of 0.70 and T(CALC)/T(OBS) = 1.43, Si/RVA(B-8) exhibits a much greater resistance to heat flux and enthalpy than does Ir/C(I-24). Addition of HfO_2 to the Ir/C(I-24) coating system improves the performance of this material by increasing its emittance (6).

V. UTILIZATION OF THE FLUX-ENTHALPY VS. ALTITUDE-VELOCITY CORRELATION TO SCREEN MATERIALS FOR SPECIFIED TRAJECTORIES

In order to illustrate the means by which Figure 36 can be employed to predict the behavior of a candidate refractory material for a specific trajectory it is worthwhile to consider the Air Force Flight Dynamics Laboratory FDL-7MC lifting reentry vehicle's maximum cross range characteristics. This vehicle is designed for a Lift/Drag ratio between 2.5 and 3.0.

Table 20 provides the altitude and velocity as a function of time. These data were employed to calculate stagnation enthalpy, pressure and heat flux based on Eqs. 50-53 for a 3" nose radius. The results are shown in Table 20 and in Figures 37-40. These figures indicate that HfB_2+SiC (A-4) and (A-7), HfB_2(A-2), ZrB_2+SiC(A-8) and HfC+C(C-11) could survive the entire trajectory in this configuration. In addition, ZrB_2(A-3) and ZrB_2+SiC+C(A-10) might also survive. Comparison of the flux-enthalpy values for this trajectory with the results of arc plasma tests shows that HfB_2(A-2), ZrB_2(A-3), HfB_2+SiC(A-4) and (A-7), ZrB_2+SiC(A-8), and ZrB_2+SiC+C(A-10) survived tests which are equivalent to the FDL-7MC with very small recessions. Due to the low temperature oxidation of HfC+C(C-11), this material might be limited for reuse (6). The borides and boride composites would not suffer from this limitation. A number of long-time cyclic exposures of diboride composites have been performed (6) in the Model 500 and ROVERS facilities to evaluate reuse capabilities for trajectories typified by FDL-7MC. The results provide a striking illustration of the reuse capability of these materials for lifting reentry applications.

Sample $HfB_{2.1}$+20%SiC(A-7)-28R was exposed for thirteen cycles at 0.07 atm stagnation pressure, a stagnation enthalpy of 10,200 BTU/lb and a cold wall heat flux of 495 BTU/ft^2sec. Each cycle was about 1800 seconds long with a total exposure time of 22,500 seconds. The surface temperature increased from one cycle to the next starting at 3500°R and holding near 5300°R for cycles 5 through 13. Total material recession was 15 mils after this extremely long exposure. Sample $ZrB_{2.1}$+20%SiC(A-8)-15M was exposed for four cycles at 1.0 atm stagnation pressure, a stagnation enthalpy of 5000 BTU/lb and a cold wall heat flux of 380 BTU/ft^2sec. Each cycle was 1800 seconds long, total exposure time was 7200 seconds. The surface temperatures were near 5000°R. Total material recession was 26 mils. Finally, sample ZrB_2+SiC+C(A-10)-26R was exposed at 0.236 atmospheres stagnation pressure, a stagnation enthalpy of 7700 BTU/lb and a cold wall heat flux of 455 BTU/ft^2sec. This test covered eleven cycles of approximately 1800 seconds duration for a total exposure time of 18,900 seconds. Surface temperature held near 5100°R after the first cycle. Total material recession was 83 mils.

These results illustrate the reuse capability of boride composites for lifting reentry application, since they exceed the range of conditions and FDL-7MC. This capability is unrivaled by any other materials system.

VI. CALCULATION OF THE FLUX-ENTHALPY BOUNDARIES FOR RECESSION RATES OF 1 MIL/SEC VIA MELTING

Figures 28-40 display the recession rates observed in arc plasma tests as a function of heat flux and stagnation enthalpy. This representation indicates the locus of heat flux, q, and stagnation enthalpies, i.e., which define the region where recession rates exceed 1 mil/sec for refractory materials. This value was arbitrarily chosen in order to illustrate a means by which the flux-enthalpy representation can be employed. The 1 mil/sec boundaries can be identified by collecting sufficient data to cover the q-i_e space completely. Since sufficient data points are not available to do this experimentally, the procedure employed in Figures 28-35 is to associate the 1 mil/sec boundary for condensed oxide forming refractory materials with a specific temperature. This procedure is quite arbitrary.

An alternative method is to consider the 1 mil/sec rate as being characteristic of melting. Under these conditions, the convective heat flux can be considered as a source of the radiative losses and the heat of melting. This heat balance is defined by Eq. 54 as follows:

$$h_e(i_e - i_w[T,P]) = \sigma\epsilon\ (T/1000)^4 + (12,000)^{-1}\rho\Delta H_f\dot{S}\ \text{BTU/ft}^2\text{sec} \tag{54}$$

where the heat transfer coefficient, h_e, is

$$h_e = q_{cw}/i_e \tag{55}$$

The enthalpy of air at the wall, $i_w[T,P]$, is given by the following expression from Eq. (4),

$$i_w[T,P] = (T/1000)\,(100 + 45\log P + (T/1000)\,(46 - 14\log P))\ \text{BTU/lb} \tag{56}$$

and q_{cw} and i_e are the cold wall heat flux and stagnation enthalpy, respectively.

In Eq. 54, $\sigma = 0.47$ BTU/ft^{2}sec^{o}R^4 is Boltzmann's constant, T^{o}R is the melting point of the refractory material, ρ is the density in lbs/ft^3, ϵ is the total normal emittance, ΔH_f is the latent heat of melting in BTU/lb and $\dot{S}$ is the recession rate in mils/sec. Since there is not available experimental data for ΔH_f, estimates have been made as indicated in Table 21. Thus, Eq. 54 is similar to the radiation equilibrium surface temperature calculation except that an additional heat loss $(12,000^{-1}\rho\Delta H_f\dot{S})$ has been included. Rearrangement yields:

$$\dot{S} = \frac{(q/i_e)\,(i_e - i_w\,[T,P]) - \sigma_\epsilon\,(T/1000)^4}{(12,000)^{-1}\,\rho \Delta H_f} \quad \text{mils/sec} \tag{57}$$

Eq. 57 defines the recession rate for melting under conditions where the convective heat flux is balanced by the radiated heat flux and the heat flux required to melt the material at a fixed recession rate. Table 21 contains values of T, ϵ, ΔH_f and ρ for the candidate materials. The latent heat of fusion has been estimated for most of these materials since virtually no measurements are available. Figures 41-44 show sample results obtained for $HfB_{2.1}$(A-2), ZrB_2(A-3), HfC+C(C-11) and ZrC+C(C-12) by setting $\dot{S}$ = 1, 3 and 10 mils/sec in Eq. 56. The location and form of these curves is in qualitative agreement with the results displayed in Figures 28-35.

VII. CALCULATION OF TEMPERATURE DISTRIBUTION THROUGH A COMPOSITE CYLINDER UNDER STEADY STATE CONDITIONS ALLOWING FOR SIDE LOSSES VIA RADIATION

The calculation of surface temperature from stream conditions based on radiation equilibrium described by Equations (1-4) in Section VII has been performed for all tests. The results which are given in Table 18 show that reasonable agreement can be obtained in most cases to within 10 or 15%. In most cases, the calculated temperature is too high. At present, the results indicate that the over estimated values are due to a reduction in heat transfer coefficient due to vaporizing oxidation products. This conclusion is based on the fact that materials containing SiC, SiO_2 and other vapor products (i.e. Sn-Al/Ta-10W(G-19) yield higher values of T(CALC)/T(OBS) as seen in Table 18. The following calculation deals with the problem of side losses via radiation and axial temperature gradients in the arc plasma test cylinders.

Representation of the steady state temperature distribution through a right circular cylinder of radius R, length L, and a coating which has a thickness I as shown below can be defined on the basis of a convective heat input and radiation losses from the front and sides according to the model shown above. In this description, the thermal conductivity of the coating and substrate are k_i and k_s, respectively.

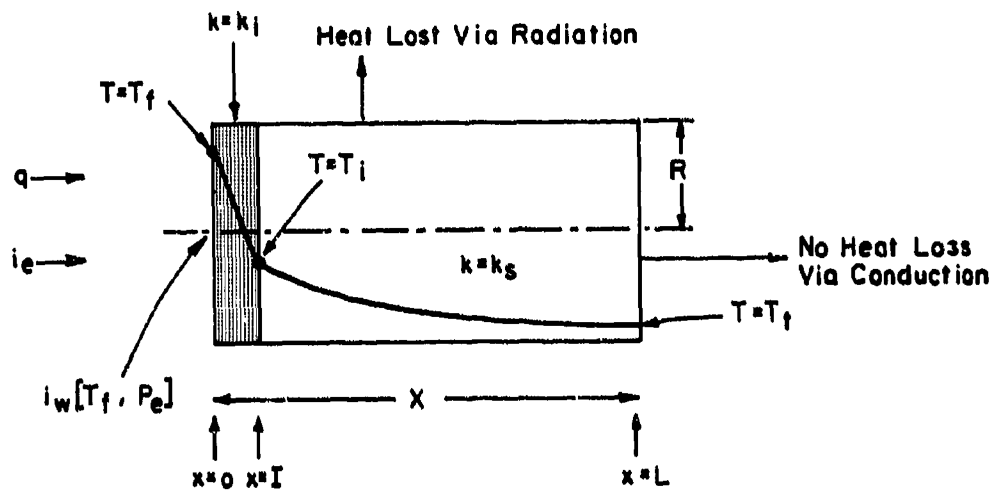

The total heat balance requires that

$$(q/i_e)\,(i_e - i_w(T_f,\ P_e)) = \sigma\epsilon\, T_f^4\,(1 + (2L/R)\,(F_F + F_S))\ \mathrm{BTU/ft^2 sec} \qquad (58)$$

where q and i_e are the cold wall heat flux and stagnation enthalpy respectively, and the enthalpy at the wall, i_w, at a temperature T_f and a stagnation pressure P_e is approximately (from Eq. (4)),

$$i_w\,[T_f, P_e] = (T_f/1000)\,(100 + 45 \log P_e + (T_f/1000)(46 - 14 \log P_e))\ \mathrm{BTU/lb} \qquad (59)$$

Evaluation of the temperature distributions along the length of the cylinder are performed on the basis of the following assumptions,

(a) the gradient through the coating is linear for $0 \leq x \leq I$

(b) the temperature distribution through the substrate is quadratic for $I \leq x \leq L$

(c) heat losses at $x = L$ are negligible

(d) there are no radial temperature gradients.

With these assumptions, the quantities F_F and F_S contained on the right side of Eq.(58) are defined as follows

$$F_F = \int_0^{\bar{x}_i} (T/T_f)^4 \, d\bar{x} \tag{60}$$

where $\bar{x} = x/L$, $\bar{x}_i = I/L$ and T is the temperature at any value of x. Similarly,

$$F_S = \int_{\bar{x}_i}^{1.0} (\epsilon_S/\epsilon)\,(T/T_f)^4 \, d\bar{x} \tag{61}$$

where ϵ_S is the emittance of the substrate and ϵ is the emittance of the coating. If the ratio $T/\bar{T}_f$ is defined as $\bar{T}$, then

$$\bar{T} = 1 - (\bar{T}_i - 1)(\bar{x}/\bar{x}_i) \quad \text{for } 0 \leq \bar{x} \leq \bar{x}_i \tag{62}$$

where $\bar{T}_i$ is equal to T/T_f at $x = I$, and

$$\bar{T} = (1-\bar{x}_i)^{-2}\,[\bar{T}_i + (\bar{T}_t - \bar{T}_i)\bar{x}(2-\bar{x}) - \bar{T}_t\bar{x}_i\,(2 - \bar{x}_i)] \quad \text{for } \bar{x}_i \leq \bar{x} \leq 1 \tag{63}$$

where $\bar{T}_t = T_t/T_f$ is the ratio of the back face temperature T_t to the front face temperature T_f. Matching of the conductive fluxes at the interface requires that

$$T_i/T_f = \bar{T}_i = [2\bar{x}_i + \bar{k}(1-\bar{x}_i)]^{-1}[2\bar{x}_i\bar{T}_t + \bar{k}(1-\bar{x}_i) - C_S\bar{x}_i(1-\bar{x}_i)\int_0^{\bar{x}_i} \bar{T}^4 \, dx] \tag{64}$$

where $\bar{k} = k_F/k_S$ is the ratio of thermal conductivities of the coating and substrate and C_S is defined by Eq. (65) as follows

$$C_S = 2\epsilon\sigma T_f^3 L^2/Rk_S \tag{65}$$

Eqs (62) and (64) permit evaluation of F_F since

$$F_F = \int_0^{\bar{x}_i} \bar{T}^4 dx = \int_0^{\bar{x}_i} (1 + \bar{x}(\bar{T}_i - 1)\bar{x}_i^{-1})^4 \, d\bar{x}$$

$$F_F = \bar{x}_i [1 + 2(\bar{T}_i - 1) + 2(\bar{T}_i - 1)^2 + (\bar{T}_i - 1)^3 + (1/5)(\bar{T}_i - 1)^4]. \tag{66}$$

Similarly, defining

$$a_3 = [\bar{T}_i - \bar{T}_t\bar{x}_i(2-\bar{x}_i)](1-\bar{x}_i)^{-2} \text{ and } a_4 = (\bar{T}_t - \bar{T}_i)a_3^{-1}(1-x_i)^{-2} \tag{67}$$

yields

$$(\epsilon/\epsilon_S)F_S = \int_{\bar{x}_i}^{1.0} a_3^4 [1 + a_4\bar{x}(2-\bar{x})]^4 \, dx \tag{68}$$

$$= a_3^4 \text{ times}$$

$$\left[\begin{array}{l} a_4^4 \left(\frac{128}{315} + x_i^5 \left[-\frac{1}{9}\bar{x}_i^4 + \bar{x}_i^3 - \frac{24}{7}\bar{x}_i^2 + \frac{16}{3}\bar{x}_i - \frac{16}{5}\right]\right) \\ + a_4^3 \left(\frac{64}{35} + 4\bar{x}_i^4 \left[\frac{1}{7}\bar{x}_i^3 - \bar{x}_i^2 + \frac{12}{5}\bar{x}_i - 2\right]\right) \\ + a_4^2 \left(\frac{16}{5} + 2x_i^3 \left[-\frac{3}{5}\bar{x}_i^2 + 3\bar{x}_i - 4\right]\right) \\ + a_4 \left(\frac{8}{3} + 4\bar{x}_i^2 \left[\frac{1}{3}\bar{x}_i - 1\right]\right) \\ + 1 - \bar{x}_i \end{array}\right] \tag{69}$$

Eq. (63)can be employed to define the temperature gradient in the cylinder at the front face

$$-\left(\frac{d\bar{T}}{d\bar{x}}\right)_{\bar{x}=0} = (1-\bar{T}_i)\bar{x}_i^{-1} \tag{70}$$

Since all of the energy entering the cylinder at its front face must be radiated away, then

$$-\left(\frac{d\bar{T}}{d\bar{x}}\right)_{\bar{x}=0} = \frac{1-\bar{T}_i}{\bar{x}_i} = C_S\bar{k}^{-1}\int_0^1 \bar{T}^4\, d\bar{x} = C_S\bar{k}^{-1}(F_F+F_S) \tag{71}$$

or

$$(F_F + F_S) = (1-\bar{T}_i)\bar{k}/\bar{x}_i C_S \tag{72}$$

When $\bar{x}_i = I = 0$, i.e., no coating is present, Eq. (62) yields

$$-\left(\frac{d\bar{T}}{d\bar{x}}\right)_{\bar{x}=0} = 2(1-\bar{T}_t) = C_S F_S \tag{73}$$

or

$$F_S = 2(1-\bar{T}_t)/C_S \tag{74}$$

The limiting case where I = L = 0, indicating no radiation losses from the sides, reduces Eq. (58) to

$$(q/i_e)(i_e - i_w[T_f, P_e]) = \sigma\epsilon T_f^4 \tag{75}$$

for radiation equilibrium from the front face. This result is identical to Equations 1-4 of Section II.

Solution of Eq. (58) for the general case where I and L are not equal to zero requires location by iteration of the proper value of T_f which satisfies Eqs. (58), (64), (73), (68) and (72). This procedure is started by employing the solution of Eq. (58) (based on I = L = 0) for T_f as a first guess. Once this first guess is available, C_s is defined by Eq. (65). These initial values of T_i and C_s are employed in conjunction with Eqs. (64), (66) and (68) to search for a value of T_i satisfying (72). The iteration procedure is begun by substituting the resultant value of $(F_F + F_S)$ into Eq. (58) and solving for the resultant error. The procedure is repeated by perturbing the initial T_f, repeating the solution and obtaining the resultant error for the second choice. Examination of these values of T_f and the resultant errors, using a Newton-Raphson method, permits the iteration process to proceed to convergence.

When I = 0 the procedure is the same except that Eq. (72) is replaced by Eq. (64). In this case F_F is zero. A computer program has been developed to perform these calculations.

Sample calculations are shown in Table 22 for arc plasma tests ZrB_2 (A-3)-2MC which exhibited a front face temperature of 4930°R and an internal temperature of 3400°R at a distance of 100 mils from the front face (6). The effects of the internal pyrometer hole was considered theoretically and found to be negligible. Consequently, the present calculations are based on the total length of 429 mils. The results illustrate the large temperature gradients through the sample indicated in reference 6.

In order to gain some insight into the effects of length, L, radius, R, coating thickness, I, and the thermophysical properties, ϵ, ϵ_S, k_F and k_S on the temperature gradients, it is instructive to reconsider Equation (58). In Equation 58, the calculation of T_f reduces to the simple radiation equilibrium case given by Equation 75 and Equations 1-4 of Section II when L is equal to zero or when R is infinitely large compared to L. When this is not the case, the temperature gradients are controlled by the values of F_F and F_S in Equation 58. These quantities are in turn dependent on the related values of T_i and T_t defined in Equations 62-64. The relation between T_i and T_t (Equation 64) specifically involves the thermophysical properties through C_S given by Equation 65. The explicit correspondence between the radiation parameters F_F and F_S and the thermophysical parameters T_i, T_t and C_S are given by Equations 72 or 74. Figure 45 shows the variation of T_i and T_t specified by Equation 64 for a representative case where $k_F/k_S = 0.10$. Figure 46 illustrates a portion of the coating contribution (F_F) to the radiation term in Equation 58 and its dependence on T_i. The total radiation parameter $(F_F + F_S)$ varies with T_i as shown in Figure 47. This dependence is illustrated for the case where I/L = 0.10 and $k_F/k_S = 0.10$ on the basis of Equations 66 and 69. Solutions for T_i and $(F_F + F_S)$ are given by the indicated intersections using Equation 72. These calculations are carried out by the computer program which then solves Equation 58. In the special case where I = 0 (no coating present), F_F vanishes and F_S as given by Equation 69 is solely dependent on T_t as shown in the figure based on Equation 74.

The effect of the thermophysical properties and the radiation losses on the surface temperature gradient within the material is evident from Equation 71. For small C_S the temperature gradient is small, as may arise for low surface temperature, (T_f), physically thin cylinders ($L \rightarrow 0$), relatively thin cylinders ($L/R \rightarrow 0$), or large thermal conductivity (k_s) aft of any coating. For large values of those parameters, C_S, and thus the temperature gradient, tend to be large. Relatively small thermal conductivity of the coating (i.e. $k = k_F/k_S$ small) also leads to larger thermal gradients. Lastly, the normalized radiation parameters, F_F and F_S, influence the gradient by partially compensating for the C_S effect. Figure 47 shows that small ($F_F + F_S$) is associated with large C_S and vice versa. Physically, this implies larger gradients at the face lead to lesser radiation losses from the aft parts of the cylinder due to the lesser temperatures then present.

Tables 23-28 summarize the results obtained by comparing the observed internal temperatures (6) with calculated values based on Eqs. 58-75 for ZrB_2+SiC(A-8), ZrB_2(A-3), HfB_2+SiC(A-7), RVA(B-5), ZrB_2+SiC+C(A-10), WSi_2/W (G-18) and Hf-Ta-Mo(I-23). These tables contain the measured front face temperature T_F, the observed temperature at a distance, d mils from the front face, T(d), and the cold wall heat flux, q, the stagnation enthalpy, i_e, and the stagnation pressure, P_e. In addition, these tables show the radius, R, length, L, and oxide coating thickness, I. The latter was equated to the conversion depth for the oxide formers (6). For WSi_2/W, I was equated to the WSi_2 coating thickness and I = 0 for RVA(B-5) graphite which ablates without coating formation. Values of the emittance, ϵ_S, taken from Table 18 as well as suitable values of the thermal conductivities of the thermal conductivity of the coating k_F and the substrate k_S are also shown in Tables 23-28.

The computed results are displayed in terms of the ratio of calculated front face temperature to observed front face temperature T_f (CALC)/T_f (OBS) and the ratio of computed in depth temperature T_d(CALC) to computed front face temperature T_f (CALC). If the agreement is exact (e.g., Hf-Ta-Mo(I-23)-43R in Table 28), the ratio of T_f (CALC)/T_f (OBS) would be 1.00. In the example T_f (CALC) is 4440°R vs. 4530°R = T_f (OBS). Similarly the measured temperature at 120 mils is 3560°R vs. T_d (CALC) = 3380°R. In this case, the observed gradient is 960°R while the calculated gradient is 1060°R in 120 mils.

All of the runs shown in Tables 23-28 were performed on flat faced cylinders except those designated by a suffix H (hemisphere) or S (cylindrical shroud with a 200 mil wall). Photographs of these models have been presented (6). The shrouds and hemispherical caps did not alter the gradients observed for flat faced cylinders. Thus all of the calculations were based on flat faced cylinders ignoring the hemispherical caps and the shrouds. Reference to Tables 23-28 indicate relatively good agreement between calculation and observation, in view of the simple model employed and the complexities of the experiments.

The largest deviations occur at low surface temperatures (i.e., T_f < 3300°R) for the materials which form SiO_2 as an oxidation product. Thus, in cases where samples of HfB_2+SiC(A-7), ZrB_2+SiC(A-8), ZrB_2+SiC+C(A-10) or WSi_2/W(G-18) were exposed with shrouds or as large diameter hemispheres T_f (CALC) is considerably larger than T_f (OBS). However, this difference is smaller than obtained when T_f is computed on the basis of radiation equilibrium (6) (i.e., Eq. 75). The cause of this behavior is presently unknown (6). Reference to Tables 23-28 shows that the calculated and observed ratios of T_d/T_f are in general agreement.

REFERENCES

1. Kaufman, L. and Nesor, H., "Stability Characterization of Refractory Materials under High Velocity Atmospheric Flight Conditions", AFML-TR-69-84 Part II Volume I: Facilities and Techniques Employed for Characterization of Candidate Materials, ManLabs, Inc., Cambridge, Mass. (September 1969).

2. Kaufman, L. and Nesor, H., "Stability Characterization of Refractory Materials under High Velocity Atmospheric Flight Conditions", AFML-TR-69-84 Part II Volume II: Facilities and Techniques Employed for Cold Gas/Hot Wall Tests, ManLabs, Inc., Cambridge, Mass. (September 1969).

3. Kaufman, L. and Nesor, H., "Stability Characterization of Refractory Materials under High Velocity Atmospheric Flight Conditions", AFML-TR-69-84 Part II Volume III: Facilities and Techniques Employed for Hot Gas/Cold Wall Tests, ManLabs, Inc., Cambridge, Mass. (September 1969).

4. Kaufman, L. and Nesor, H., "Stability Characterization of Refractory Materials under High Velocity Atmospheric Flight Conditions", AFML-TR-69-84 Part III Volume I: Experimental Results of Low Velocity Cold Gas/Hot Wall Tests, ManLabs, Inc., Cambridge, Mass. (September 1969).

5. Perkins, R., Kaufman, L. and Nesor, H., "Stability Characterization of Refractory Materials under High Velocity Atmospheric Flight Conditions", AFML-TR-69-84 Part III Volume II: Experimental Results of High Velocity Cold Gas/Hot Wall Tests, ManLabs, Inc., Cambridge, Mass. (September 1969).

6. Kaufman, L. and Nesor, H., "Stability Characterization of Refractory Materials under High Velocity Atmospheric Flight Conditions", AFML-TR-69-84 Part III Volume III: Experimental Results of High Velocity Hot Gas/Cold Wall Tests, ManLabs, Inc., Cambridge, Mass. (September 1969).

7. Kaufman, L. and Clougherty, E.V., "Investigation of Boride Compounds for Very High Temperature Applications", RTD-TDR-63-4096 Part III (March 1966).

8. Tate, S. and Collesimo, D., Cornell Aeronautical Laboratory, Private Communication (December 1966).

9. Marshall, B.W., AIAA Journal (1966) 4 1899.

10. Hoercher, H., Avco/SSD Private Communication (December 1966).

11. Etemad, G.A. and Holly, D.E., AIAA Journal (1966) 4 1543-8.

REFERENCES (CONT)

12. Metzger, J.W., Engel, M.J. and Diaconis, N.S., AIAA Jnl. (1967) 5, 451.

13. Tanzilli, R.A., "Evaluation of Graphite Composites in Reentry Environments", AFML-TR-65-328 (October 1965).

14. Lawthers, D.D. and Sama, L., "Development of Coatings for Protection of High Strength Tantalum Alloys in Severe High Temperature Environments", AFML-TR-67-374, November 1967. Progress Report #1. (STR-66-56013)(Augsut 1966).

15. Stinebring, R.C. and Sturiale, T., "Development of Nondestructive Methods for Evaluating Diffusion Formed Coatings on Metallic Substrates", AFML-TR-66-221 (September 1966).

16. Grindle, S.L. and Todd, J.P., "Evaluation of Thermal Protective Systems under Simulated Reentry Conditions", ML-TDR-64-293 (February 1965).

17. Criscione, J.M., et al., "High Temperature Protective Coatings for Graphite", ML-TDR-64-173, Part II (October 1964).

18. Leeds, D.H., Welsh, W.E., Slaughter, J.I. and Kendall, E.G., "Air Plasma Arc Materials Testing for Reentry", SSD-TDR-64-75, (June 1964).

19. White, J.E. and Leeds, D.H., "A Metallurgical Evaluation of Various Commercial Infiltrated Tungsten Materials in Air and Nitrogen Plasmas", SSD-TR-65-54 (May 1965).

20. Kendall, E.G., Slaughter, J.I. and Riley, W.C., "A New Class of Hypereutectic Carbide Composites", Aerospace Corp., TDR-469(52500-10)-11(SSD-TD-65-78) (June 1965).

21. Hansen, C.G., "Approximation for the Thermodynamic and Transport Properties of High Temperature Air", NASA Technical Report No. R-50 (1959).

22. Fay, J.A. and Riddell, F.R., J. Aeronautical Sciences (1958) 25, 73.

23. Hansen, C.F. and Heims, S.P., A Review of the Thermodynamic Transport and Chemical Reaction Rate Properties of High Temperature Air, NACA-TN 4359 (1958).

24. Morey, F.C., NBS-NACA Tables of Thermal Properties of Gases Table 239 for Dry Air Coefficients of Viscosity, Dept. of Commerce, NBS Publication (December 1950).

REFERENCES (CONT)

25. Baron, J.R., Private Communication (March 1965).

26. Cooper, M. and Mayo, E.E., "Measurement of Local Heat Transfer and Pressure on Six, Two Inch Diameter Blunt Bodies at M = 4.95", NASA Memo 1-3-59L (1959).

27. Heister, N.K. and Clark, C.F., SAMPE Journal (1967) 3 No. 6 p. 14.

28. Boison, J.C. and Curtiss, H.A., J. Am. Rocket Soc. (1954) 2, 130.

29. Comfort, E.H., O'Connor, T.J. and Cass, L.A., Heat Transfer Resulting from the Normal Infringement of a Turbulent High Temperature Jet on an Infinitely Large Flat Plate, Proc. of the 1966 Heat Transfer and Fluid Mechanics Institute, Stanford University Press.

30. Bernstein, H. and Baron, J.R., "Stability Characterization of Refractory Materials Under High Velocity Atmospheric Flight Conditions", AFML-TR-69-84 Part IV Volume II: Calculation of the General Surface Reaction Problem, ManLabs, Inc., Cambridge, Mass. (September 1969).

31. Scala, S.M., "The Ablation of Graphite in Dissociated Air:, IAS National Summer Meeting, Los Angeles, Calif., June 1962.

32. Scala, S.M. and Gilbert, L., AIAA Entry Technology Conference, Williamsburg and Hampton, Va., Oct. 1964.

33. John, R.R. and Schick, H.L., "Testing of Re-enforced Plastics under Simulated Re-entry Conditions, Part II, Experimental Determination of the Steady State Heat of Ablation", Avco RAD-TR-9(7)-60-11 (1960).

34. Gulbransen, E.A., Andrew, K.F. and Brassart, F.A., "The Oxidation of Graphite at Temperatures of 600° to 1500°C and at Pressures of 2 to 76 Torr of Oxygen", J. Electro. Chem. Soc. 110, No. 6, 477, 1963.

35. Okada, J. and Ikeqawa, T., "Combustion Rate of Artificial Graphite from 700°-2000°C in Air", J. of App. Phys., 24, 1249, 1953.

36. Ong, J.N. Jr., "On the Kinetics of Oxidation of Graphite", Carbon, (2), 1964, 281-297.

37. Sallis, D.V., Sparhawk, H.E. and Hotchkiss, H.H. "Evaluation of Ablative Materials" AFML-TR-66-348 Martin-Marietta Corp., Baltimore, Maryland, September 1967 p. 143.

38. Blyholder, G. and Eyring, H.J., Phys. Chem. (1957), 61, 683.

39. Hansen, C.G., "Approximation for the Thermodynamic and Transport Properties of High Temperature Air", NASA Technical Report No. R-50 (1959).

40. Katsikas, C.J., Castle, G.K. and Higgins, Ablation Handbook and Entry Materials Data and Design, AFML-TR-66-262 (Sept. 1966).

41. Rose, P.H. and Stark, W.I., J. Aero. Sciences (1958) 25, 86.

TABLE 1

SUMMARY OF PUBLISHED FLUX-TEMPERATURE DATA FOR REFRACTORY MATERIALS

Material	Mach No.	P_e (atm)	i_e (BTU/lb)	D (in.)	q_{cw} (BTU/ft^2 sec)	T (^{o}R) (obs)	Ratio T(CALC)/T(OBS) Cold Wall Heat Transfer	Ratio T(CALC)/T(OBS) Fay-Riddell Coefficient
ZrB_2 (7)								
C-2	3.50	0.014	6400	0.488*	27	3033	1.00	1.42
C-3	3.50	0.013	7100	0.483*	56	3443	1.05	1.28
C-5	3.50	0.013	7450	0.484*	65	3560	1.05	1.25
C-4	3.50	0.012	8400	0.470*	76	4253	0.92	1.08
C-6	3.50	0.012	8200	0.483*	100	4406	0.94	1.03
C-7	3.50	0.012	9200	0.480*	108	4523	0.94	1.04
C-8	3.50	0.013	11100	0.480*	112	4640	0.93	1.07
C-9	3.50	0.022	10700	0.478*	160	5135	0.91	1.02
C-1	0.47	1.19	1680	0.500*	264	3983	1.03	1.01
C-14	0.60	1.22	2380	0.452*	260	4127	1.08	1.14
C-15	0.48	1.18	1720	0.449*	264	4379	0.94	0.93
C-16	0.50	1.12	4800	0.451*	423	4631	1.18	1.29
N-4	3.5	0.008	8900	0.426*	100	3910	1.06	1.15
N-1	3.5	0.009	8300	0.384*	86	3613	1.11	1.25
N-8	3.5	0.008	7200	0.385*	65	3204	1.16	1.34
N-9	3.5	0.008	8100	0.425*	68	3040	1.25	1.44
N-10	3.5	0.010	11400	0.425*	120	4291	1.02	1.15
N-10	3.5	0.010	12000	0.425*	120	4685	0.94	1.07
ZrB_2 (8)	2.90	36.0	1935	0.500*	2330	4860	1.15	1.13
Boride Z (8)	2.90	36.0	1935	0.500*	2420	4560	1.23	1.21

*D is the hemispherical cap diameter of the model. An asterisk indicates a flat face cylinder having a geometrical diameter of D inches.

TABLE 2

SUMMARY OF PUBLISHED FLUX-TEMPERATURE DATA FOR REFRACTORY MATERIALS

Material	Mach No.	P_e (atm)	i_e (BTU/lb)	D (in.)	q_{cw} (BTU/ft^2 sec)	T (^oR) (obs)	Ratio T(CALC)/T(OBS) Cold Wall Heat Transfer	Ratio T(CALC)/T(OBS) Fay-Riddell Coefficient
HfB_2 (7)								
A-94	0.18	1.03	3580	0.279*	137	4091	1.03	1.28
A-83	0.27	1.05	4840	0.269*	266	4901	1.02	1.23
A-211A	0.47	1.18	1680	0.301*	264	3443	1.19	1.20
A-212	0.73	1.74	1400	0.301*	122	4415	0.79	0.90
A-211B	0.20	1.02	6640	0.301*	440	4307	1.33	1.50
A-213	0.52	1.45	1420	0.302*	90	4865	0.69	0.80
A-201	0.36	1.06	5160	0.291*	464	4973	1.13	1.25
HfB_2-SiC (7)								
A-224	0.30	1.05	6480	0.303*	364	4163	1.32	1.59
A-196A	0.33	1.07	4640	0.300*	464	4523	1.23	1.32
A-196B	0.39	1.09	3920	0.300*	422	4559	1.17	1.25
A-238	0.43	1.10	5180	0.301*	422	4667	1.18	1.35
A-223	0.32	1.05	7580	0.302*	472	5171	1.14	1.35
ZrO_2 (8)	2.80	36.0	1925	0.250*	3500	4460	1.28	1.26
Hf-Ta Alloy (8) on Ta-10W	2.80	37.0	1910	0.500*	2430	4560	1.22	1.20
Ta (9)	3.0	0.050	5000	0.500*	180	4630	1.05	1.05
ϵ = 0.45	3.0	0.085	6000	0.500*	270	5350	0.98	1.01
	3.0	0.106	4900	0.500*	240	5180	1.02	1.01

*D is the hemispherical cap diameter of the model. An asterisk indicates a flat face cylinder having a geometrical diameter of D inches.

TABLE 3

SUMMARY OF PUBLISHED FLUX-TEMPERATURE DATA FOR REFRACTORY MATERIALS

Material	Mach No.	P_e (atm)	i_e (BTU/lb)	D (in.)	q_{cw} (BTU/ft^{2}sec)	T (^oR) (obs)	Ratio T(CALC)/T(OBS) Cold Wall Heat Transfer	Ratio T(CALC)/T(OBS) Fay-Riddell Coefficient
Pyrolytic (10) Graphite $\epsilon = 0.45$	0.51	1.00	3860	0.750*	600	5895	1.00	0.94
	0.66	1.00	1300	0.750*	270	4095	0.94	0.89
	0.50	1.00	3740	0.750*	620	5760	1.02	0.95
	0.64	1.00	1280	0.750*	250	4230	0.90	0.85
Boron-Pyrolytic Graphite (8)	2.10	72.0	2310	1.250	3500	4560	1.40	1.39
	2.10	71.0	2060	1.250	3100	4760	1.26	1.25
Hafnium-Pyrolytic Graphite (8)	2.20	68.0	2180	0.624	4150	4460	1.41	1.40
Boron-Nitride (8)	2.40	56.0	1800	0.600	3400	3900	1.42	1.42
	3.10	26.0	1720	0.600	2200	4210	1.26	1.26
	3.10	27.0	1830	0.600	2200	3260	1.65	1.65
Silicon-Carbide (8)	2.20	68.7	1970	0.600	3830	6100	0.97	0.97
	3.00	31.6	1810	0.600	2370	5750	0.94	0.94
	2.60	47.7	2190	0.600	3570	5100	1.21	1.21
	2.20	69.1	2180	0.600*	4280	5100	1.23	1.23
	2.90	36.0	1970	0.250*	3360	4060	1.42	1.40
Macrolaminate of Mo, HfO_2 and ThO_2 (8)	2.10	74.0	2270	0.400	--	4260	--	1.54
	2.10	72.0	2170	0.400	--	4760	--	1.34

*D is the hemispherical cap diameter of the model. An asterisk indicates a flat face cylinder having a geometrical diameter of D inches.

TABLE 4

SUMMARY OF PUBLISHED FLUX-TEMPERATURE DATA FOR REFRACTORY MATERIALS

Material	Mach No.	P_e (atm)	i_e (BTU/lb)	D (in.)	q_{cw} (BTU/ft^{2}sec)	T (°R) (obs)	Ratio T(CALC)/T(OBS) Cold Wall Heat Transfer	Ratio T(CALC)/T(OBS) Fay-Riddell Coefficient
Macrolaminate of Mo, HfO_2, ThO_2 (8)	2.10	72.0	2170	0.400	----	4260	----	1.49
	2.10	72.0	2120	0.400	----	4360	----	1.44
	2.10	71.0	2070	0.400	----	4160	----	1.48
	2.20	70.0	2040	0.400	----	4160	----	1.47
	2.20	68.0	1930	0.400	3000	3460	1.67	1.70
	1.90	86.0	2060	0.400	4300	4760	1.29	1.31
	2.60	48.0	1850	0.400	4300	4760	1.19	1.18
Macrolaminate of Tungsten and HfO_2 (8)	2.20	68.0	1930	0.400	----	4160	----	1.42
HfC-C (20) 13 w/o C	2.4	50	2080	0.600	4080	5715	1.06	1.05
Tungsten (11)								
EH-1	2.00	68.1	2001	0.600	3830	4850	1.23	1.23
EH-2	2.00	66.5	1860	0.600	3490	4880	1.17	1.17
EH-3	2.30	52.7	1765	0.300	4160	5480	1.01	1.01
EH-4	2.40	52.4	1531	0.300	3500	4650	1.08	1.08
EH-5	2.50	45.1	1794	0.300	3940	5550	1.00	1.00
EH-6	2.60	38.7	1796	0.300	3610	5060	1.09	1.09

*D is the hemispherical cap diameter of the model. An asterisk indicates a flat face cylinder having a geometrical diameter of D inches.

TABLE 5

SUMMARY OF PUBLISHED FLUX-TEMPERATURE DATA FOR REFRACTORY MATERIALS

Material	Mach No.	P_e (atm)	i_e (BTU/lb)	D (in.)	q_{cw} (BTU/ft^2 sec)	T (°R) (obs)	Ratio T(CALC)/T(OBS) Cold Wall Heat Transfer	Ratio T(CALC)/T(OBS) Fay-Riddell Coefficient
Tungsten (8)	2.90	36.0	2035	0.531*	2370	3660	1.57	1.54
	2.10	71.0	2180	0.280	6950	4360	1.48	1.47
	3.60	11.8	2150	0.500	1910	4060	1.39	1.39
	3.80	5.0	2015	0.500	1160	3860	1.34	1.34
	3.60	11.0	2030	0.500	1730	4560	1.20	1.20
	3.80	4.9	1875	0.500	1055	3460	1.44	1.45
	2.90	33.8	2230	1.000	2360	3760	1.59	1.56
	2.90	35.5	2190	1.000	2390	4260	1.40	1.39
	3.20	24.9	2110	0.500	2850	4460	1.31	1.31
	3.20	25.2	2060	0.500	2680	4660	1.24	1.24
	3.20	24.9	1920	0.500	2455	4560	1.21	1.21
	3.10	26.0	1810	0.600	2200	4880	1.09	1.09
	2.50	52.0	1770	0.600	3400	5220	1.05	1.04
	2.50	53.0	1530	0.300	3520	3750	1.34	1.34
	2.20	68.8	2000	0.600	3840	3700	1.61	1.61
	2.20	68.0	1860	0.600	3530	4100	1.39	1.39
	2.60	46.7	1790	0.300	4000	4500	1.23	1.23
	2.40	54.6	1770	0.300	4230	4600	1.21	1.21
Tungsten (11) ZrB_2 Coated								
EH-9	2.10	62.1	1982	0.600	3560	5500	1.07	1.07
EH-10	2.50	47.2	2118	0.600	3570	4200	1.44	1.44
EH-11	2.90	29.5	2114	0.600	2740	4000	1.47	1.45

*D is the hemispherical cap diameter of the model. An asterisk indicates a flat face cylinder having a geometrical diameter of D inches.

TABLE 6

SUMMARY OF PUBLISHED FLUX-TEMPERATURE DATA FOR REFRACTORY MATERIALS

Material	Mach No.	P_e (atm)	i_e (BTU/lb)	D (in.)	q_{cw} (BTU/ft^2 sec)	T (°R) (obs)	Ratio T(CALC)/T(OBS) Cold Wall Heat Transfer	Ratio T(CALC)/T(OBS) Fay-Riddell Coefficient
ZrB_2 (8) on Tungsten	2.10	70.4	1980	0.600	3900	4710	1.26	1.26
	2.60	47.7	2190	0.600	3570	5000	1.23	1.23
	3.00	29.8	2110	0.600	2740	3730	1.55	1.55
Tungsten (11) 11.4 w/o Ag								
EH-12	2.4	52.1	1540	0.600	2480	4530	1.10	1.10
Tungsten (8) Silver	2.50	53.1	1540	0.600	2500	3800	1.31	1.32
Tungsten (11) Durac Coated								
EH-7	2.10	61.2	1979	0.600	3500	5500	1.07	1.07
EH-8	2.50	43.5	2131	0.600	3340	5000	1.21	1.21
Durac (8) on Tungsten	2.20	68.7	1980	0.600	3860	4500	1.32	1.32
	2.70	44.4	2130	0.600	3360	5200	1.16	1.16
Tungsten (11) Sn-Al infilt.								
EH-24	2.40	50.8	1450	0.300	3240	5600	0.87	0.87

*D is the hemispherical cap diameter of the model. An asterisk indicates a flat face cylinder having a geometrical diameter of D inches.

TABLE 7

SUMMARY OF PUBLISHED FLUX-TEMPERATURE DATA FOR REFRACTORY MATERIALS

Material	Mach No.	P_e (atm)	i_e (BTU/lb)	D (in.)	q_{cw} (BTU/ft^2 sec)	T (°R) (obs)	Ratio T(CALC)/T(OBS) Cold Wall Heat Transfer	Ratio T(CALC)/T(OBS) Fay-Riddell Coefficient
Tungsten (8) Sn-Al	2.40	54.6	1450	0.300	3360	4500	1.08	1.08
Tungsten (10) 30% Zn ε = 0.40	0.5	1.0	3900	0.750	860	5700	1.12	1.07
Tungsten (8) Alloys	2.30	61.9	1900	0.600	3420	4800	1.18	1.18
	2.20	67.4	1990	0.600	3750	4040	1.47	1.47
	2.30	64.0	1920	0.600	3520	4200	1.38	1.38
	2.30	62.5	1940	0.600	3720	4370	1.35	1.33
	3.00	32.0	2185	0.600	2940	4200	1.43	1.43
	2.60	45.1	2060	0.600	3240	3870	1.53	1.53
	2.20	65.0	2150	0.600	4100	3780	1.65	1.64
	3.00	30.0	1920	0.600	2430	4040	1.38	1.38
	2.20	65.0	1900	0.600	3500	4800	1.20	1.20
	2.20	69.0	2040	0.600	3690	4380	1.38	1.38
	2.20	65.0	2000	0.600	3700	5650	1.05	1.05
	2.20	66.0	2070	0.600	3880	4200	1.45	1.47
	2.30	63.0	1950	0.600	3520	6220	0.94	0.94

*D is the hemispherical cap diameter of the model. An asterisk indicates a flat face cylinder having a geometrical diameter of D inches.

TABLE 8

SUMMARY OF PUBLISHED FLUX-TEMPERATURE DATA FOR REFRACTORY MATERIALS

Material	Mach No.	P_e (atm)	i_e (BTU/lb)	D (in.)	q_{cw} (BTU/ft^2 sec)	T (^oR) (obs)	Ratio T(CALC)/T(OBS) Cold Wall Heat Transfer	Ratio T(CALC)/T(OBS) Fay-Riddell Coefficient
Tungsten (11) 10 w/o Cu								
EH-13	2.00	64.4	2157	0.600	4070	5050	1.23	1.23
EH-14	2.30	55.8	1960	0.600	3510	6250	0.93	0.93
EH-15	2.30	53.6	1481	0.600	2410	4750	1.03	1.03
EH-16	2.50	44.3	2057	0.600	3210	4800	1.23	1.23
EH-17	2.90	31.9	2184	0.600	2930	5000	1.20	1.20
EH-18	2.30	53.8	1519	0.300	3520	5600	0.90	0.90
EH-19	2.50	43.0	1886	0.300	4040	5650	1.01	1.01
EH-20	2.90	30.6	1963	0.300	3560	4700	1.22	1.22
EH-21	2.50	45.1	1783	0.600	2760	5350	1.02	1.02
EH-22	2.60	41.2	1563	0.300	3100	4750	1.07	1.07
EH-23	2.90	28.3	1712	0.300	2910	4880	1.08	1.08
Tungsten (8)	2.20	65.0	2005	0.600	3720	4630	1.29	1.28
Copper	2.40	54.6	1520	0.300	3550	4250	1.18	1.18
	2.40	54.7	1480	0.600	2440	4000	1.22	1.22
	3.00	31.1	1960	0.300	3580	4000	1.44	1.44
	2.80	39.2	1850	0.300	3630	4400	1.27	1.28
	2.70	44.0	1890	0.300	4090	4600	1.24	1.24

*D is the hemispherical cap diameter of the model. An asterisk indicates a flat face cylinder having a geometrical diameter of D inches.

TABLE 9

SUMMARY OF PUBLISHED FLUX-TEMPERATURE DATA FOR REFRACTORY MATERIALS

Material	Mach No.	P_e (atm)	i_e (BTU/lb)	D (in.)	q_{cw} (BTU/ft^2 sec)	T (°R) (obs)	Ratio T(CALC)/T(OBS) Cold Wall Heat Transfer Coefficient	Ratio T(CALC)/T(OBS) Fay-Riddell Heat Transfer Coefficient
Graphite (10)								
ε = 0.70	0.33	1.07	8240	0.750*	1360	6230	1.15	1.02
0.64	0.58	1.18	7870	0.750*	1450	6490	1.13	1.03
0.65	0.72	1.36	6640	0.750*	1610	6470	1.12	1.00
0.66	0.82	1.46	4900	0.750*	1230	5870	1.12	1.01
0.63	0.76	1.40	3980	0.750*	918	5420	1.12	1.02
0.65	0.33	1.07	6800	0.750*	1250	6320	1.14	1.04
0.62	0.51	1.17	8090	0.750*	1410	6530	1.13	1.03
0.61	0.73	1.37	6470	0.750*	1480	6550	1.10	0.99
0.59	0.82	1.48	4940	0.750*	1230	5920	1.13	1.02
0.61	0.76	1.40	3890	0.750*	860	5310	1.13	1.04
0.66	0.50	1.16	7720	0.750*	1450	6470	1.12	1.12
0.64	0.71	1.35	6230	0.750*	1610	6430	1.12	0.99
0.65	0.81	1.46	4940	0.750*	1230	5890	1.11	1.01
0.64	0.74	1.38	3960	0.750*	918	5300	1.14	1.03
0.68	0.31	1.06	8660	0.750*	1250	6370	1.12	1.02
0.61	0.51	1.17	7670	0.750*	1410	6530	1.12	1.02
0.60	0.73	1.37	6340	0.750*	1480	6520	1.11	0.99
0.57	0.82	1.48	4900	0.750*	1230	5970	1.13	1.02
0.65	0.74	1.38	3900	0.750*	860	5150	1.15	1.06
0.66	0.50	1.16	7560	0.750*	1450	6350	1.14	1.02
0.62	0.73	1.37	6420	0.750*	1610	6380	1.14	1.01
0.64	0.82	1.48	4910	0.750*	1230	5820	1.14	1.02
0.64	0.73	1.37	3910	0.750*	918	5120	1.18	1.07
0.65	0.33	1.07	8580	0.750*	1250	6320	1.13	1.04
0.63	0.51	1.17	7960	0.750*	1410	6440	1.14	1.04
0.61	0.73	1.37	6510	0.750*	1480	6490	1.11	1.00
0.60	0.83	1.49	4970	0.750*	1230	5900	1.14	1.03
0.63	0.75	1.39	3920	0.750*	860	5070	1.18	1.08

*D is the hemispherical cap diameter of the model. An asterisk indicates a flat face cylinder having a geometrical diameter of D inches.

TABLE 10

SUMMARY OF PUBLISHED FLUX-TEMPERATURE DATA FOR REFRACTORY MATERIALS

Material	Mach No.	P_e (atm)	i_e (BTU/lb)	D (in.)	q_{cw} (BTU/ft^2 sec)	T (^oR) (obs)	Ratio T(CALC)/T(OBS) Cold Wall Heat Transfer	Fay-Riddell Coefficient
ATJ Graphite	8.8	0.008	11,880	0.250*	135	2560	1.76	2.03
(12)	8.8	0.008	11,880	0.250*	135	2450	1.84	2.12
	5.7	0.056	11,880	0.250*	490	4030	1.51	1.60
	5.7	0.056	11,880	0.250*	490	3930	1.54	1.64
(Estimated	5.7	0.056	11,880	0.250*	490	4275	1.42	1.51
Mach No.) =	9.0	0.010	13,560	1.000*	72	2295	1.70	2.06
	9.0	0.010	13,560	1.000*	72	2375	1.64	1.99
	9.0	0.010	13,560	1.000*	72	3060	1.28	1.54
	9.0	0.010	13,560	1.000*	72	2930	1.33	1.61
	8.9	0.008	11,880	0.063*	280	2745	1.94	2.21
	8.9	0.008	11,880	0.063*	280	2785	1.96	2.22
	8.9	0.008	11,880	0.063*	280	2820	1.89	2.15
	8.9	0.008	11,880	0.063*	280	2665	2.00	2.27
	8.9	0.008	11,880	0.063*	280	2660	2.01	2.28
	8.9	0.008	11,880	0.063*	280	2670	2.00	2.27
	8.9	0.008	11,880	0.063*	280	2600	2.05	2.33
	8.5	0.007	5,420	1.000*	50	2300	1.51	1.56
	8.5	0.007	5,420	1.000*	50	2270	1.53	1.56
	8.5	0.007	5,420	1.000*	50	2340	1.49	1.51
	8.5	0.007	5,420	1.000*	50	2270	1.53	1.56
	8.5	0.007	5,420	1.000*	50	2285	1.52	1.54
	8.5	0.007	5,420	1.000*	50	2295	1.52	1.54
	8.0	1.0	16,610	0.750*	2050	7200	1.19	1.22
	8.0	1.0	7,120	0.750*	805	5760	1.13	1.17

*D is the hemispherical cap diameter of the model. An asterisk indicates a flat face cylinder having a geometrical diameter of D inches.

TABLE 11

SUMMARY OF PUBLISHED FLUX-TEMPERATURE DATA FOR REFRACTORY MATERIALS

Material	Mach No.	P_e (atm)	i_e $\left(\frac{BTU}{lb}\right)$	D (in.)	q_{cw} $\left(\frac{BTU}{ft^2 sec}\right)$	T (^oR) (obs)	Ratio T(CALC)/T(OBS) Cold Wall Heat Transfer Coefficient	Ratio T(CALC)/T(OBS) Fay-Riddell Heat Transfer Coefficient
RVA (13)	8.5	0.007	5440	0.500*	67	2690	1.38	1.42
	8.7	0.008	13000	0.500*	104	2715	1.57	1.81
(Estimated Mach No.) =	8.0	1.000	16600	0.500*	2240	5800	1.51	1.58
	6.2	0.028	5400	0.250*	320	3190	1.62	1.49
	5.4	0.051	13000	0.250*	495	4530	1.35	1.45
RVA (13)	8.5	0.007	5400	0.500*	67	2420	1.54	1.58
Purified	8.7	0.008	13000	0.500*	104	2535	1.68	1.94
	5.8	0.051	13000	0.250*	495	4750	1.29	1.38
(Estimated Mach No.) =	8.0	1.000	16600	0.500*	2240	5915	1.48	1.54
PT-0178 (13)	8.5	0.007	5400	1.000*	49	2610	1.33	1.35
(Estimated Mach No.) =	8.0	1.000	16600	0.500*	2240	6340	1.38	1.44
(Estimated Mach No.) =	8.0	1.000	16600	0.500*	2240	6075	1.44	1.50
	6.2	0.028	5400	0.250*	320	3060	1.69	1.56
	5.8	0.051	13000	0.250*	495	4235	1.41	1.52
	8.5	0.007	5400	0.500*	67	2750	1.35	1.39
	8.7	0.008	13000	0.500*	104	2785	1.53	1.77
PT-0181 (13)	8.5	0.007	5400	1.000*	49	2645	1.31	1.33
	8.5	0.007	5400	0.500*	67	2640	1.41	1.44
	8.7	0.008	13000	0.500*	104	2875	1.48	1.71
(Estimated	5.8	0.051	13000	0.250*	495	4200	1.45	1.56
Mach No.) =	8.0	1.000	16600	0.500*	2240	6620	1.32	1.38

*D is the hemispherical cap diameter of the model. An asterisk indicates a flat face cylinder having a geometrical diameter of D inches.

TABLE 12

SUMMARY OF PUBLISHED FLUX-TEMPERATURE DATA FOR REFRACTORY MATERIALS

Material	Mach No.	P_e (atm)	i_e (BTU/lb)	D (in.)	q_{cw} (BTU/ft^2sec)	T (^oR) (obs)	Ratio T(CALC)/T(OBS) Cold Wall Heat Transfer	Ratio T(CALC)/T(OBS) Fay-Riddell Coefficient
PT-0182 (13)	8.5	0.007	5400	1.000*	49	2690	1.29	1.31
	8.5	0.007	5400	0.500*	67	2740	1.35	1.39
	8.7	0.008	13000	0.500*	104	2825	1.51	1.74
	5.8	0.051	13000	0.250*	495	4395	1.39	1.49
(Estimated Mach No.) =	8.0	1.000	16600	0.500*	2240	6735	1.30	1.36
JTA (13)	5.4	0.051	13000	0.250*	400	4320	1.35	1.52
	5.4	0.051	13000	0.250*	400	4320	1.35	1.52
	6.2	0.028	5400	0.250*	280	2880	1.75	1.65
	6.2	0.028	5400	0.250*	280	2880	1.75	1.65
	5.8	0.051	13000	0.250*	400	4320	1.35	1.52
(Estimated Mach No.) =	8.0	1.000	16600	0.500*	2240	5400	1.60	1.69
70% Dense	0.76	1.00	6550	0.750*	1460	6390	1.20	1.07
Tungsten (10)	0.80	1.00	4061	0.750*	905	6230	1.04	0.93
	0.79	1.00	7168	0.750*	1415	6970	1.18	1.01
ϵ = 0.41	0.59	1.00	10363	0.750*	1280	6880	1.18	1.14
Hf-20Ta	----	0.002	8208	3.000*	20	2560	1.22	1.27
Coating on	----	0.006	8203	3.000*	51	3010	1.29	1.23
Ta-10W (14)	----	0.035	8180	3.000*	99	3760	1.20	1.21

*D is the hemispherical cap diameter of the model. An asterisk indicates a flat face cylinder having a geometrical diameter of D inches.

TABLE 13

SUMMARY OF PUBLISHED FLUX-TEMPERATURE DATA FOR REFRACTORY MATERIALS

Material	Mach No.	P_e (atm)	i_e $\left(\frac{BTU}{lb}\right)$	D (in.)	q_{cw} $\left(\frac{BTU}{ft^2\ sec}\right)$	T (°R) (obs)	Ratio T(CALC)/T(OBS) Cold Wall Heat Transfer	Ratio T(CALC)/T(OBS) Fay-Riddell Coefficient
W-3 Coated	3.00	0.005	13900	1.00*	80	2680	1.44	1.56
TZM Alloy (15, 10)	3.00	0.009	16100	1.00*	140	3000	1.48	1.55
	3.00	0.007	15400	1.00*	144	3030	1.47	1.48
ε = 0.70	3.00	0.008	15600	1.00*	146	3000	1.49	1.52
(one inch	3.00	0.006	14900	1.00*	127	3000	1.44	1.45
diameter arc	3.00	0.007	17100	1.00*	130	3080	1.42	1.49
impinging on	3.00	0.006	17700	1.00*	120	3090	1.38	1.47
two inch	3.00	0.009	15800	1.00*	130	3070	1.42	1.51
square foil)	3.00	0.005	16800	1.00*	126	3070	1.41	1.43
	3.00	0.008	16800	1.00*	148	3070	1.46	1.51
	3.00	0.007	17100	1.00*	136	3070	1.44	1.50
Cr-Ti-Si	3.00	0.006	13800	1.00*	138	3000	1.46	1.42
Coated Cb752	3.00	0.005	12700	1.00*	112	3020	1.38	1.35
Alloy (15, 10)	3.00	0.008	13100	1.00*	140	3060	1.44	1.42
ε = 0.70	3.00	0.008	12400	1.00*	124	3090	1.38	1.38
(exposure same	3.00	0.008	12900	1.00*	140	3060	1.44	1.42
as above)	3.00	0.006	13000	1.00*	124	3090	1.38	1.36
JTA (16)	3.00	0.016	12000	2.00	175	4280	1.05	1.07
ε = 0.80	3.00	0.012	7180	2.00	91	4830	0.78	0.80
	3.00	0.020	18000	2.00	305	5140+	1.01	1.02
	3.00	0.015	11080	2.00	170	4460	1.00	1.00
	3.00	0.015	9770	2.00	153	4430	0.98	0.9[illegible]
	3.00	0.020	18060	2.00	292	5180+	0.99	1.0[illegible]
	3.00	0.035	5900	2.00	139	3110	1.33	1.33
	3.00	0.042	13450	2.00	336	3810+	1.38	1.39
	3.00	0.046	11100	2.00	290	3740+	1.35	1.36

*D is the hemispherical cap diameter of the model. An asterisk indicates a flat face cylinder having a geometrical diameter of D inches.

+Surface melting reported.

TABLE 14

SUMMARY OF PUBLISHED FLUX-TEMPERATURE DATA FOR REFRACTORY MATERIALS

Material	Mach No.	P_e (atm)	i_e $\left(\frac{BTU}{lb}\right)$	D (in.)	q_{cw} $\left(\frac{BTU}{ft^2 sec}\right)$	T (^oR)	Ratio T(CALC)/T(OBS) Cold Wall Heat Transfer	Ratio T(CALC)/T(OBS) Fay-Riddell Coefficient
ZrO_2 foam (16)	3.00	0.016	12230	2.00	173	4200	1.07	1.10
ϵ = 0.8	3.00	0.016	12000	2.00	170	4760	0.94	0.96
	3.00	0.016	11930	2.00	170	4750	0.94	0.96
ZrO_2 fibrous (16)	3.00	0.016	11890	2.00	174	4020	1.12	1.14
ϵ = 0.8	3.00	0.016	11985	2.00	176	4370	1.03	1.05
	3.00	0.016	12120	2.00	175	4550	0.99	1.01
Ir coated C (17) ϵ = 0.3	Sub-sonic	1.00	5380	0.50	80	4180	1.08	1.81
			cylinder side					
JTA (17) ϵ = 0.60	Sub-sonic	1.00	4170	0.500	80	4180	0.91	1.48
			cylinder side					
Ir coated (17) ϵ = 0.3	3.5	0.06	4565	0.500	80	4180	1.06	..35
			cylinder side					
JTA (17)	3.5	0.06	4510	0.500	80	3515	1.09	1.41

TABLE 15

SUMMARY OF PUBLISHED FLUX-TEMPERATURE DATA FOR REFRACTORY MATERIALS

Material	Mach No.	P_e (atm)	i_e (BTU/lb)	D (in.)	q_{cw} (BTU/ft^2 sec)	T (°R) (obs)	Ratio T(CALC)/T(OBS) Cold Wall Heat Transfer	Ratio T(CALC)/T(OBS) Fay-Riddell Coefficient
ThO_2 (18)	0.90	1.00	6620	0.500*	700	6120	1.02	1.07
BPG	0.90	1.00	6260	0.500*	700	5940	1.05	1.10
PG	0.90	1.00	6260	0.500*	700	5760	1.08	1.14
ThO_2 + $CuSO_4$	0.90	1.00	6260	0.500*	700	5580	1.12	1.17
TiC (HP)	0.90	1.00	6260	0.500*	700	5400	1.16	1.21
TaC-C (HP)	0.90	1.00	6260	0.500*	700	5400	1.16	1.21
PG	0.90	1.00	6260	0.500*	700	5400	1.16	1.21
HfC-C (AC)	0.90	1.00	6260	0.500*	700	5400	1.16	1.21
TiC-C (AC)	0.90	1.00	6260	0.500*	700	5220	1.20	1.25
HfC-C (AC)	0.90	1.00	6260	0.500*	700	5400	1.16	1.21
TiC-C (AC)	0.90	1.00	6260	0.500*	700	5220	1.20	1.25
ZrC-C (AC)	0.90	1.00	6260	0.500*	700	5220	1.20	1.25
TiB_2 (AC)	0.90	1.00	6260	0.500*	700	5220	1.20	1.25
ATJ	0.90	1.00	6260	0.500*	700	5040	1.24	1.30
BN	0.90	1.00	6260	0.500*	700	4860	1.28	1.35
PT0179	0.90	1.00	6260	0.500*	700	4860	1.28	1.35
W (forged)(18)	0.90	1.00	6260	0.500*	700	4860	1.28	1.35
JTA	0.90	1.00	6260	0.500*	700	4860	1.28	1.35
SiC (HP)	0.90	1.00	6260	0.500*	700	4680	1.33	1.40
PT0178	0.90	1.00	6260	0.500*	700	4500	1.39	1.45
W + (Cu-Zn)	0.90	1.00	6260	0.500*	700	4320	1.45	1.52
W + (Cu-Zn)	0.90	1.00	6260	0.500*	700	4320	1.45	1.52
W + (Cu-Si)	0.90	1.00	6260	0.500*	700	3960	1.56	1.65

*D is the hemispherical cap diameter of the model. An asterisk indicates a flat face cylinder having a geometrical diameter of D inches.

TABLE 16

SUMMARY OF PUBLISHED FLUX-TEMPERATURE DATA FOR REFRACTORY MATERIALS

Material	Mach No.	P_e (atm)	i_e (BTU/lb)	D (in.)	q_{cw} (BTU/ft^2sec)	T (°R) (obs)	Ratio T(CALC)/T(OBS) Cold Wall Heat Transfer Coefficient	Ratio T(CALC)/T(OBS) Fay-Riddell Heat Transfer Coefficient
W + (Sn-Al)	0.90	1.00	6260	0.500*	700	3780	1.65	1.73
BPG	0.90	1.00	10500	0.400*	2400	6480	1.31	1.22
HfC (HP)	0.90	1.00	10500	0.400*	2400	6300	1.34	1.25
ATJ	0.90	1.00	10500	0.400*	2400	6300	1.34	1.25
TaC-C (HP)	0.90	1.00	10500	0.400*	2400	6120	1.38	1.29
JTA	0.90	1.00	10500	0.400*	2400	5940	1.43	1.33
HfC-C (AC)	0.90	1.00	10500	0.400*	2400	5940	1.43	1.33
W + (Sn-Al)	0.90	1.00	10500	0.400*	2400	5760	1.47	1.37
W + (ThO_2)	0.90	1.00	10500	0.400*	2400	5760	1.47	1.37
HfC-C (AC)	0.90	1.00	10500	0.400*	2400	5580	1.52	1.41
W (forged)	0.90	1.00	10500	0.400*	2400	5400	1.57	1.46
BN	0.90	1.00	10500	0.400*	2400	4860	1.74	1.62
W (forged) (19)	0.90	1.00	6260	0.500*	700	3460	1.80	1.89
W (forged)	0.90	1.00	10500	0.400*	2400	5460	1.55	1.44

*D is the hemispherical cap diameter of the model. An asterisk indicates a flat face cylinder having a geometrical diameter of D inches.

TABLE 17

TEMPERATURE AND PRESSURE DEPENDENCE OF THE ENTHALPY OF AIR (BTU/LB)*

T °R	Log P +2	+1	0	-1	-2
2700	704	704	704	704	704
	707	707	709	709	709
	(644)	(625)	(605)	(585)	(566)
	(430)	(462)	(494)	(526)	(558)
3600	968	968	968	971	980
	980	980	981	983	991
	(917)	(937)	(956)	(975)	(995)
	(764)	(821)	(879)	(936)	(993)
4500	1238	1244	1263	1318	1485
	1274	1279	1295	1346	1497
	(1220)	(1300)	(1382)	(1462)	(1543)
	(1194)	(1284)	(1373)	(1462)	(1551)
5400	1530	1574	1707	2055	2641
	1596	1634	1750	2063	2630
	(1551)	(1716)	(1881)	(2046)	(2211)
	(1720)	(1848)	(1977)	(2106)	(2234)
6300	1867	2053	2485	3060	3293
	1967	2115	2489	3047	3341
	(1911)	(2183)	(2456)	(2727)	(3000)
	(2341)	(2516)	(2691)	(2866)	(3041)
7200	2321	2746	3329	3596	3719
	2416	2759	3301	3631	3789
	(2301)	(2703)	(3104)	(3506)	(3908)
	(3058)	(3286)	(3515)	(3743)	(3972)
8100	2890	3495	3879	4073	4523
	2943	3447	3877	4131	4585
	(2720)	(3274)	(3828)	(4382)	(4936)
	(3870)	(4159)	(4448)	(4738)	(5027)
9000	3536	4086	4382	4913	6468
	3515	4037	4412	4964	6469
	(3168)	(3897)	(4626)	(5354)	(6084)
	(4778)	(5135)	(5492)	(5847)	(6206)

*The sequence of values is, Reference (21) Reference (10) (Equation (4)) and(Equation (5)).

TABLE 18

AVERAGED VALUES OF TOTAL NORMAL EMITTANCE AND RATIOS OF CALCULATED AND OBSERVED TEMPERATURES DERIVED FROM HOT GAS/COLD WALL ARC PLASMA TESTS

Material/Code		ϵ_N Computed Normal Emittance (Solid)	(Melting)	Calculated Temperature Ratio T(CALC)/T (OBS) - Cold Wall Heat Transfer Coefficient (Solid)	(Melting)
$HfB_{2.1}$	A-2	0.45	0.39	1.16	0.98
ZrB_2	A-3	0.47 (0.500")	0.39 (0.500")	1.09 (0.500")	1.08 (0.500")
ZrB_2	A-3	0.57 (0.750")	---- (0.750")	1.12 (0.750")	---- (0.750")
HfB_2 + 20 v/o SiC	A-4	0.62	0.48	1.22	1.07
Boride Z	A-5	0.75	----	1.20	----
$HfB_{2.1}$ + 20 v/o SiC	A-7	0.55	0.47	1.25	0.99
$ZrB_{2.1}$ + 20 v/o SiC	A-8	0.59	0.50	1.34	1.02
$HfB_{2.1}$ + 35 v/o SiC	A-9	0.55	0.52	1.17	0.99
ZrB_2 + 14 v/o SiC + 30 v/o C	A-10	0.62	0.55	1.20	1.11
RVA	B-5	0.52	0.75	1.17	1.20
		(0.500 inch)	(0.740 inch)	(0.500 inch)	(0.740 inch)
PG	B-6	0.41 ⊥ to C	0.41 ∥ to C	1.19 ⊥ to C	1.04 ∥ to C
BPG	B-7	0.37 ⊥ to C	0.43 ∥ to C	1.18 ⊥ to C	1.03 ∥ to C
Si/RVC	B-8	0.69 Coated	0.56 Bare	1.36 Coated	1.07 Bare

TABLE 18 (Cont'd.)

AVERAGED VALUES OF TOTAL NORMAL EMITTANCE AND RATIOS OF CALCULATED AND OBSERVED TEMPERATURES DERIVED FROM HOT GAS/COLD WALL ARC PLASMA TESTS

Material/Code		ϵ_N Computed Normal Emittance (Solid)	ϵ_N Computed Normal Emittance (Melting)	Calculated Temperature Ratio T(CALC)/T(OBS)-Cold Wall Heat Transfer Coefficient (Solid)	Calculated Temperature Ratio T(CALC)/T(OBS)-Cold Wall Heat Transfer Coefficient (Melting)
PT0178	B-9	0.65	----	1.07	----
Poco Graphite	B-10	0.64	----	1.18	----
Glassy Carbon	B-11	0.50	----	1.00	----
HfC + C	C-11	0.57	0.50	1.10	1.05
ZrC + C	C-12	0.60	0.42	1.08	1.01
JTA	D-13	0.52	0.55	1.13	0.93
KT-SiC	E-14	0.63	----	1.43	----
JT0992	F-15	0.48	0.60	1.04	1.08
JT0981	F-16	0.49	0.51	1.11	1.05
WSi_2/W	G-18	0.58 Coated	0.32 Bare	1.54 Coated	1.13 Bare
Sn-Al/Ta-10W	G-19	0.59 Coated	0.44 Bare	1.41 Coated	1.09 Bare
W + Zr + Cu	G-20	0.52	0.49	1.31	1.12
W + Ag	G-21	0.54	0.33	1.35	1.01
SiO_2 + 68.5 w/o W	H-22	0.61	----	1.12	----
SiO_2 + 60 w/o W	H-23	0.56	----	1.27	----
Hf-20Ta-2Mo	I-23	0.60 (0.500")	0.45 (0.500")	1.20 (0.500")	1.00 (0.500")
		0.59 (0.750")	---- (0.750")	1.14 (0.750")	---- (0.750")
Ir/C	I-24	0.36 Coated	0.83 Bare	1.21 Coated	1.15 Bare
		0.51 Oxide Coated		1.06 Oxide Coated	

TABLE 19

COMPARISON OF CALCULATED AND OBSERVED RECESSION RATES FOR RVA(B5), PT0178(B9), POCO(B10) AND ATJ GRAPHITES (FLAT FACED CYLINDERS)

Sample No.	$\dot{S}(OBS)$ Observed Recession Rate (mils/sec)	T ^{o}R	P_e (atm)	Density (lbs/ft^3)	Mach No.	Diameter Initial/Final (mils)	Effective Radius R_B	$\dot{S}(CALC)$ Calculated Recession Rate (mils/sec)	$\dot{S}(OBS)$/$\dot{S}(CALC)$
B5-2M	2.630	5040	1.070	112	0.33	500/221	0.0375	2.553	1.029
B5-3M	1.630	4500	1.050	112	0.30	500/282	0.0407	2.281	0.714
B5-5M	3.410	6180	1.100	112	0.39	500/333	0.0434	2.639	1.291
B5-6M	4.160	6250	1.150	112	0.49	500/337	0.0435	2.864	1.452
B5-7M	3.390	5830	1.120	112	0.43	500/308	0.0420	2.756	1.229
B5-1R	1.800	5165	0.187	112	3.20	486/430	0.0476	1.381	1.302
B5-2R	0.510	4110	0.029	112	3.20	487/299	0.0409	0.562	0.906
B5-3R	0.550	4865	0.013	112	3.20	487/273	0.0395	0.479	1.147
B5-4R	1.260	4665	[illegible]	112	3.20	487/384	0.0452	1.280	0.984
B5-5R	0.520	4470	[illegible]	112	3.20	486/276	0.0336	0.457	1.136
B5-6R	0.500	4570	0.016	112	3.20	487/376	0.0449	0.422	1.184
B5-7R	1.900	5890	0.299	112	3.20	486/401	0.0461	1.801	1.054
B5-11M	1.850	4375	1.060	112	0.31	741/644	0.0715	1.815	1.018
B5-12M	2.100	4630	1.070	112	0.32	741/643	0.0720	1.863	1.126
B5-13M	2.500	4995	1.070	112	0.34	741/630	0.0713	1.934	1.292
B5-14R	0.310	4010	0.012	112	3.20	741/579	0.0686	0.294	1.051
B5-15R	0.410	4500	0.024	112	3.20	741/588	0.0691	0.420	0.974
B5-16R	1.460	5855	0.218	112	3.20	739/602	0.0698	1.271	1.148
B5-L1*	1.000	3300	1.000	112	0.23	500/500	0.0520	1.459	0.685
B5-L2*	2.330	3400	1.000	112	0.23	*/*	0.0052	2.186	1.065
B5-L3*	2.800	4000	1.000	112	0.23	*/*	0.0052	3.081	0.908
B5-L4	3.200	4400	1.000	112	0.23	*/*	0.0052	3.608	0.886
B5-GE1	0.039	2410	0.007	115	8.00	500/500	0.0520	0.119	0.325
B5-GE2	0.092	2660	0.007	115		500/500	0.0520	0.158	0.580
B5-GE3	0.084	2750	0.007	115		500/500	0.0520	0.171	0.493
B5-GE4	0.081	2790	0.007	115		500/500	0.0520	0.176	0.458
B5-GE5	0.055	2660	0.007	115		500/500	0.0520	0.158	0.347
B5-GE6	0.138	2680	0.008	115		500/500	0.0520	0.169	0.812
B5-GE7	0.149	2680	0.008	115		500/500	0.0520	0.177	0.838
B5-GE8	0.094	2680	0.008	115		500/500	0.0520	0.182	0.516
B5-GE9	3.590	5130	1.000	115		500/500	0.0520	2.921	1.228
B5-GE13	0.666	3010	0.028	115		250/250	0.0260	0.402	1.654
B5-GE14	0.765	3120	0.028	115		250/250	0.0260	0.436	1.753
B5-GE15	0.898	3260	0.028	115		250/250	0.0260	0.477	1.882
B5-GE16	1.115	3320	0.028	115		250/250	0.0260	0.493	2.259
B5-GE17	1.134	4320	0.051	115		250/250	0.0260	0.880	1.288
B5-GE18	1.178	4320	0.051	115		250/250	0.0260	0.880	1.336
B5-GE19	1.178	4650	0.051	115		250/250	0.0260	0.922	1.276
MED514	0.307	2718	0.008	107	8.00	63/63	0.006	0.233	1.315
MED513	0.305	2691	0.008	107				0.225	1.349
MED557	0.391	2952	0.008	107				0.298	1.308
MED521	0.306	2790	0.008	107				0.253	1.208
MED520	0.293	2799	0.008	107				0.255	1.145
MED519	0.361	2835	0.008	107				0.265	1.358
MED518	0.312	2844	0.008	107				0.268	1.162
MED517	0.321	2871	0.008	107				0.275	1.163
MED516	0.334	2844	0.008	107				0.268	1.244
MED515	0.311	2799	0.008	107				0.255	1.216
MED514	0.284	2763	0.008	107				0.245	1.155
MED513	0.290	2736	0.005	107				0.238	1.217
MED557	0.205	2664	0.008	107				0.218	0.937
MED521	0.335	2601	0.008	107				0.201	1.659
MED520	0.311	2637	0.008	107				0.211	1.471
MED518	0.343	2691	0.008	107				0.225	1.518
MED517	0.363	2718	0.008	107				0.233	1.555
MED516	0.365	2691	0.008	107				0.225	1.615
MED515	0.326	2646	0.008	107				0.213	1.524
MED514	0.289	2610	0.008	107				0.204	1.415
MED513	0.288	2583	0.008	107				0.197	1.461
MED521	0.279	2664	0.008	107				0.218	1.276
MED518	0.241	2718	0.008	107				0.233	1.033
MED517	0.262	2655	0.008	107				0.216	1.211
MED516	0.315	2718	0.008	107				0.233	1.350
MED515	0.274	2673	0.008	107				0.221	1.239
MED514	0.255	2637	0.008	107				0.211	1.206
MED513	0.263	2610	0.008	107				0.204	1.287
MED521	0.298	2655	0.008	107				0.216	1.378
MED516	0.388	2709	0.008	107				0.230	1.680
MED515	0.307	2664	0.008	107				0.218	1.404
MED514	0.262	2628	0.008	107				0.208	1.253
B10-8R	0.490	4360	0.015	114	3.20	500/399	0.0467	0.391	1.253
B10-9R	0.770	5380	0.034	114	3.20	502/384	0.0461	0.605	1.271
B10-10R	2.120	5810	0.218	114	3.20	502/340	0.0438	1.551	1.366

Sample No.	$\dot{S}(OBS)$ Observed Recession Rate (mils/sec)	T ^{o}R	P_e (atm)	Density (lbs/ft^3)	Mach No.	Diameter Initial/Final (mils)	Effective Radius R_B (ft.)	$\dot{S}(CALC)$ Calculated Recession Rate (mils/sec)	$\dot{S}(OBS)$/$\dot{S}(CALC)$
B5-GP1	0.077	2290	0.007	115	8.00	500/500	0.0520	0.100	0.763
B5-GP2	0.106	2450	0.007	115		500/500	0.0520	0.126	0.840
B5-GP3	0.106	2580	0.007	115		500/500	0.0520	0.146	0.724
B5-GP4	0.125	2500	0.008	115		500/500	0.0520	0.140	0.887
B5-GP5	0.180	2540	0.008	115		500/500	0.0520	0.147	1.220
B5-GP6	1.090	4560	0.051	115		250/250	0.0260	0.912	1.194
B5-GP7	1.000	4830	0.051	115		250/250	0.0260	0.939	1.063
B5-GP8	0.770	5000	0.051	115		250/250	0.0260	0.953	0.807
B5-GP9	0.655	4720	0.051	115		250/250	0.0260	0.929	0.704
B5-GP10	0.624	4780	0.051	115		250/250	0.0260	0.935	0.667
B5-GP11	4.430	5580	1.000	115		500/500	0.0520	3.013	1.470
B5-GP12	4.320	5650	1.000	115		500/500	0.0520	3.023	1.428
B5-GP13	4.450	6060	1.000	115		500/500	0.0520	3.074	1.447
B5-GP14	4.380	5580	1.000	115		500/500	0.0520	3.013	1.45[illegible]
B9-1M	3.920	5375	1.050	81	0.28	495/163	0.0342	3.517	1.114
B9-2M	2.750	4650	1.030	81	0.24	495/148	0.0334	3.203	0.858
B9-3M	4.420	5410	1.050	81	0.29	495/246	0.0335	3.379	1.307
B9-4M	4.760	6280	1.060	81	0.31	495/235	0.0330	3.559	1.337
B9-5M	5.170	6445	1.070	81	0.33	495/204	0.03[illegible]3	3.738	1.383
B9-6R	0.480	4250	0.011	81	3.20	495/307	0.04[illegible]7	0.495	0.969
B9-7R	0.720	4680	0.023	81	3.20	495/321	0.04[illegible]4	0.717	1.003
B9-8R	0.900	5180	0.028	81	3.20	495/346	0.04[illegible]6	0.783	1.148
B9-9R	1.040	5500	0.030	81	3.20	495/363	0.04[illegible]3	0.845	1.229
B9-10R	4.40	6355	0.213	81	3.20	495/500	0.04[illegible]8	2.242	1.962
B9-GE1	0.089	2660	0.007	94	8.00	1000/1000	0.10[illegible]0	0.169	0.526
B9-GE7	1.070	3080	0.028	94		250/250	0.02[illegible]0	0.518	2.061
B9-GE8	1.080	3080	0.028	94		250/250	0.02[illegible]0	0.518	2.081
B9-GE10	1.780	4250	0.051	94		250/250	0.02[illegible]0	1.063	1.673
B9-GE11	0.130	2560	0.007	94		500/500	0.0520	0.175	0.741
B9-GE12	0.150	2650	0.007	94		500/500	0.0520	0.192	0.781
B9-GE13	0.160	2810	0.007	94		500/500	0.0520	0.219	0.728
B9-GE14	0.180	2770	0.007	94		500/500	0.0520	0.212	0.845
B9-GE15	0.220	2770	0.008	94		500/500	0.0520	0.224	0.979
B9-GE16	0.230	2770	0.008	94		500/500	0.0520	0.224	1.024
B9-GE17	0.280	2810	0.008	94		500/500	0.0520	0.231	1.206
B9-GE18	0.180	2840	0.008	94		500/500	0.0520	0.236	0.760
MED305	0.114	2223	0.010	107	8.00	1000/1000	0.104	0.104	1.091
MED308	0.112	2241	0.010	107				0.107	1.043
MED311	0.105	2241	0.010	107				0.107	0.977
MED316	0.100	2241	0.010	107				0.107	0.931
MED307	0.131	2304	0.010	107				0.117	1.112
MED303	0.126	2322	0.010	107				0.120	1.043
MED308	0.115	2340	0.010	107				0.123	0.929
MED311	0.106	2340	0.010	107				0.123	0.857
MED306	0.104	2340	0.010	107				0.123	0.840
MED307	0.121	2340	0.010	107				0.123	0.978
MED307	0.111	2358	0.010	107				0.126	0.876
MED311	0.102	2358	0.010	107				0.126	0.805
MED316	0.101	2358	0.010	107				0.126	0.797
MED308	0.108	2376	0.010	107				0.129	0.833
MED311	0.099	2376	0.010	107				0.129	0.764
MED303	0.100	2376	0.010	107				0.129	0.771
MED308	0.091	2394	0.010	107				0.132	0.687
MED316	0.097	2394	0.010	107				0.132	0.732
MED311	0.101	2394	0.010	107				0.132	0.762
MED323	0.280	3006	0.010	107				0.208	1.345
MED326	0.279	3033	0.010	107				0.210	1.327
MFD322	0.276	3141	0.010	107				0.217	1.270
MED325	0.259	3033	0.010	107				0.210	1.232
MED327	0.284	3024	0.010	107				0.209	1.355
MED324	0.284	3051	0.010	107				0.211	1.342
MED322	0.282	3159	0.010	107				0.218	1.291
MED325	0.261	3051	0.010	107				0.211	1.234
MED327	0.295	3042	0.010	107				0.210	1.399
MED326	0.299	3078	0.010	107				0.213	1.401
MED325	0.300	3186	0.010	107				0.219	1.364
MED327	0.290	3150	0.010	107				0.217	1.331
MED322	0.299	3186	0.010	107				0.219	1.360
MED326	0.286	3042	0.010	107				0.210	1.356
B10-1M	1.960	4820	1.060	114	0.30	501/321	0.042[illegible]	2.267	0.864
B10-2M	3.130	6040	1.080	114	0.36	501/303	0.0411	2.549	1.227
B10-3M	2.620	5600	1.070	114	0.53	501/337	0.0434	2.400	1.091
B10-4M	3.260	6260	1.090	114	0.38	501/353	0.0443	2.541	1.282
B10-5M	3.680	6580	1.110	114	0.42	501/394	0.0465	2.587	1.422
B10-6M	2.350	4800	1.060	114	0.31	501/342	0.0438	2.262	1.038
B10-7R	0.450	4980	0.025	114	3.20	502/364	0.0450	0.522	0.861

*One-half inch diameter-30° half angle cylinder cones. R_B assumed equal to 62 mils.

TABLE 19 (CONT.)

COMPARISON OF CALCULATED AND OBSERVED RECESSION RATES FOR RVA(B5), PT0178(B9), POCO(B10) AND ATJ GRAPHITES (FLAT FACED CYLINDERS)

Sample No.	$\dot{s}$(OBS) Observed Recession Rate (mils/sec)	T °R	P_e (atm)	Density (lbs/ft³)	Mach No.	Diameter Initial/Final (mils)	Effective Radius R_B ft.	$\dot{s}$(CALC) Calculated Recession Rate (mils/sec)	$\dot{s}$(OBS)/$\dot{s}$(CALC)
MED323	0.224	2430	0.010	107	8.00	1000/1000	0.104	0.138	1.620
MED323	0.223	2610	0.010	107				0.165	1.349
MED325	0.240	2610	0.010	107				0.165	1.452
MED322	0.260	3150	0.010	107				0.217	1.193
MED325	0.265	2934	0.010	107				0.202	1.310
MED327	0.269	2860	0.010	107				0.197	1.364
MED330	0.547	3690	0.044	107				0.478	1.143
MED331	0.547	3285	0.044	107				0.440	1.241
MED342	0.566	3222	0.044	107				0.432	1.310
MED336	0.604	3528	0.044	107				0.466	1.294
MED342	0.544	3807	0.044	107				0.484	1.122
MED332	0.610	3843	0.044	107				0.486	1.254
MED342	0.561	2880	0.044	107				0.367	1.527
MED331	0.573	3690	0.044	107				0.478	1.198
MED330	0.619	2880	0.044	107				0.367	1.685
MED521	0.310	2727	0.008	107		63/63	0.006	0.235	1.314
MED520	0.308	2736	0.008	107				0.238	1.292
MED519	0.325	2772	0.008	107				0.248	1.309
MED518	0.314	2781	0.008	107				0.250	1.252
MED517	0.316	2808	0.008	107				0.258	1.223
MED516	0.321	2781	0.008	107				0.250	1.280
MED515	0.312	[illegible]	0.008	107				0.238	1.309
MED514	0.306	[illegible]	0.008	107				0.228	1.322
MED513	0.301	2673	0.008	107				0.222	1.361
MED557	0.263	2907	0.008	107				0.286	0.919
MED521	0.317	2745	0.008	107				0.240	1.316
MED520	0.320	2748	0.008	107				0.240	1.329
MED519	0.345	2790	0.008	107				0.253	1.362
MED518	0.325	2799	0.008	107				0.255	1.271
MED517	0.328	2826	0.008	107				0.263	1.246
MED516	0.335	2799	0.008	107				0.255	1.310
MED515	0.321	2754	0.008	107				0.243	1.319
MED513	0.270	2601	0.008	107	8.00	63/63	0.006	0.201	1.337
MED521	0.287	2691	0.008	107				0.225	1.270
MED516	0.368	2745	0.008	107				0.240	1.528
MED515	0.287	2700	0.008	107				0.228	1.256
MED514	0.251	2664	0.008	107				0.218	1.149
MED513	0.263	2637	0.008	107				0.211	1.244
MED516	0.207	2646	0.008	107				0.213	0.968
MED513	0.212	2592	0.008	107				0.199	1.062
MED521	0.287	2655	0.008	107				0.216	1.327
MED514	0.216	2628	0.008	107				0.208	1.038
MED515	0.251	2601	0.008	107				0.201	1.243
MED521	0.217	2601	0.008	107				0.201	1.075
MED514	0.287	2601	0.008	107				0.201	1.422
MED521	0.279	2520	0.008	107				0.180	1.542
MED516	0.261	2628	0.008	107				0.208	1.248
MED520	0.296	2538	0.008	107				0.185	1.596
MED631	0.114	2304	0.008	107		1000/1000	0.104	0.108	1.052
MED634	0.116	2286	0.008	107				0.105	1.098
MED642	0.124	2304	0.008	107				0.108	1.144
MED635	0.123	2313	0.008	107				0.109	1.121
MED633	0.115	2218	0.008	107				0.102	1.117
MED639	0.140	2313	0.008	107				0.109	1.276
MED638	0.141	2295	0.008	107				0.106	1.317
MED643	0.139	2340	0.008	107				0.113	1.222
MED644	0.142	2331	0.008	107				0.112	1.263
MED632	0.081	2268	0.008	107				0.102	0.786
MED634	0.073	2259	0.007	107				0.096	0.755
MED642	0.080	2268	0.007	107				0.097	0.816
MED635	0.074	2286	0.007	107				0.100	0.736
MED633	0.052	2241	0.007	107				0.094	0.552
MED635	0.081	2376	0.007	107	8.00	1000/1000	0.104	0.113	0.716
MED641	0.056	2232	0.007	107				0.092	0.603
MED641	0.096	2259	0.007	107				0.096	0.992
MED634	0.087	2286	0.007	107				0.100	0.865
MED642	0.120	2295	0.007	107				0.101	1.179
MED635	0.105	2313	0.007	107				0.104	1.006
MED635	0.093	2241	0.007	107				0.094	0.988
MED642	0.070	2322	0.007	107				0.105	0.663
MED634	0.151	2313	0.007	107				0.104	1.447

Sample No.	$\dot{s}$(OBS) Observed Recession Rate (mils/sec)	T °R	P_e (atm)	Density (lbs/ft³)	Mach No.	Diameter Initial/Final (mils)	Effective Radius R_B ft.	$\dot{s}$(CALC) Calculated Recession Rate	$\dot{s}$(OBS)/$\dot{s}$(CALC)
MED496	1.288	3870	0.056	107	8.00	250/250	0.026	0.885	1.454
MED501	1.397	3825	0.056	107				0.872	1.600
MED495	1.248	3915	0.056	107				0.897	1.390
MED494	1.264	4014	0.056	107				0.922	1.369
MED490	1.279	4788	0.056	107				1.050	1.217
MED498	1.325	3888	0.056	107				0.890	1.487
MED497	1.270	3888	0.056	107				0.890	1.426
MED488	1.310	4176	0.056	107				0.958	1.366
MED501	1.263	3924	0.056	107				0.900	1.403
MED489	1.331	3996	0.056	107				0.918	1.449
MED501	1.332	3924	0.056	107				0.900	1.479
MED496	1.360	3888	0.056	107				0.890	1.527
MED490	1.273	4788	0.056	107				1.050	1.211
MED497	1.266	3888	0.056	107				0.890	1.421
MED488	1.450	4176	0.056	107				0.958	1.512
MED498	1.363	3843	0.056	107				0.878	1.438
MED488	1.407	4122	0.056	107				0.947	1.484
MED495	1.380	4833	0.056	107				1.055	1.307
MED495	1.320	3933	0.056	107				0.902	1.462
MED488	1.320	4230	0.056	107				0.969	1.361
MED498	1.240	3906	0.056	107				0.895	1.384
MED501	1.240	3780	0.056	107				0.859	1.442
MED489	1.310	4932	0.056	107				1.064	1.230
MED497	1.320	4104	0.056	107				0.943	1.398
MED501	1.310	4842	0.056	107				1.056	1.240
MED497	1.310	3942	0.056	107				0.904	1.447
MED490	1.320	4806	0.056	107				1.052	1.254
MED641	0.066	2295	0.007	107	8.00	1000/1000	0.104	0.101	0.648
MED639	0.069	2286	0.007	107				0.100	0.686
MED638	0.037	2268	0.007	107				0.097	0.377
MED646	0.028	2178	0.007	107				0.085	0.328
MED644	0.100	2277	0.007	107				0.099	1.007
MED634	0.099	2325	0.007	107				0.106	0.933
MED642	0.110	2259	0.007	107				0.096	1.137
MED635	0.106	2412	0.007	107				0.118	0.898
MED633	0.083	2367	0.007	107				0.111	0.742
MED641	0.106	2286	0.007	107				0.100	1.054
MED639	0.136	2412	0.007	107				0.118	1.152
MED638	0.138	2394	0.007	107				0.115	1.194
MED634	0.089	2304	0.007	107				0.103	0.863
MED642	0.101	2313	0.007	107				0.104	0.968
MED635	0.095	2331	0.007	107				0.106	0.889
MED633	0.066	2256	0.007	107				0.096	0.685
MED641	0.090	2205	0.007	107				0.089	1.011
MED639	0.114	2351	0.007	107				0.106	1.066
MED638	0.070	2313	0.007	107				0.104	0.671
MED638	0.096	2205	0.007	107				0.089	1.078
MED634	0.091	2313	0.007	107				0.104	0.872
MED642	0.105	2322	0.007	107				0.105	0.994
MED635	0.098	2340	0.007	107				0.108	0.906
MED633	0.066	2295	0.007	107				0.101	0.648
MED641	0.048	2214	0.007	107				0.090	0.531
MED639	0.133	2340	0.007	107				0.108	1.230
MED642	0.083	2250	0.007	107				0.095	0.870
MED639	0.088	2241	0.007	107				0.094	0.934
MED634	0.077	2331	0.007	107				0.106	0.720
MED642	0.093	2205	0.007	107				0.089	1.044
MED463	0.216	2565	0.008	107		250/250	0.026	0.176	1.224
MED472	0.224	2673	0.008	107				0.198	1.123
MED462	0.242	2664	0.008	107				0.197	1.227
MED474	0.246	2529	0.008	107				0.169	1.460
MED473	0.262	2583	0.008	107				0.179	1.456
MED463	0.215	2520	0.008	107				0.166	1.291
MED461	0.172	2493	0.008	107				0.160	1.069
MED458	0.287	2466	0.008	107				0.155	1.850
MED474	0.290	2538	0.008	107				0.170	1.702
MED459	0.345	2520	0.008	107				0.166	2.071
MED461	0.344	2538	0.008	107				0.170	2.019
MED462	0.343	2529	0.008	107				0.168	2.036
MED473	0.338	2565	0.008	107				0.176	1.919
MED472	0.244	2592	0.008	107				0.181	1.342
MED463	0.134	2340	0.008	107				0.129	1.037
MED461	0.157	2376	0.008	107				0.136	1.150
NED473	0.188	2340	0.008	107				0.129	1.455
MED462	0.200	2412	0.008	107				0.143	1.389
MED474	0.207	2340	0.008	107				0.129	1.602

TABLE 19 (CONT)

COMPARISON OF CALCULATED AND OBSERVED RECESSION RATES FOR RVA(B-5), PT0178(B-9), POCO(B-10) AND ATJ GRAPHITES (FLAT FACE CYLINDERS)

Sample No.	S(OBS) Observed Recession Rate	T ^{o}R	P_e (atm)	Density (lbs/ft^3)	Mach No.	Diameter Initial/Final (mils)	Effective Radius R_B ft.	S(CALC) Calculated Recession Rate (mils/sec)	$\frac{S(OBS)}{S(CALC)}$
B5-23M	0.878	3725	1.000	112	0.10	502/350	0.0443	1.275	0.689
B5-24M	0.992	4105	1.000	112	0.13	502/330	0.0433	1.525	0.650
B5-25M	0.522	3420	1.000	112	0.15	503/400	0.0449	1.420	0.368
B5-26M	0.269	3035	1.000	112	0.15	503/380	0.0460	1.192	0.226
B5-27M	0.430	2995	1.000	112	0.15	502/340	0.0438	1.175	0.366
B5-31M	0.538	3285	1.000	112	0.10	501/350	0.0443	1.174	0.458
B5-32M	0.422	3475	1.000	112	0.10	502/405	0.0472	1.199	0.352
B5-16R	1.463	5855	0.218	112	3.20	739/620	0.0707	1.266	1.156
B5-28R	0.018	2165	0.005	112	3.20	503/500	0.0522	0.074	0.243
B5-29R	0.086	2780	0.008	112	3.20	504/490	0.0517	0.188	0.457
B5-30R	0.244	3465	0.011	112	3.20	502/470	0.0505	0.298	0.819

TABLE 20

CALCULATION OF FLUX-ENTHALPY CONDITIONS CORRESPONDING TO THE TRAJECTORY FOR THE FDL-7MC HYPERSONIC RE-ENTRY VEHICLE UNDER MAXIMUM CROSS RANGE CONDITIONS

(R_B = 3")

Time (sec)	Altitude (kft)	Velocity kft/sec	i_e BTU/lb	q BTU/ft^{2}sec	P_e (atm)
200	260	26	13500	210	0.03
400	200	25	12500	480	0.21
600	190	23	10600	450	0.25
800	180	22	9700	480	0.34
1000	180	20	8000	360	0 28
1200	180	18	6500	260	0.23
1400	170	16	5100	210	0.24
1600	160	14	3900	170	0.28
1800	150	13	3400	170	0.36
2000	140	12	2900	160	0.43
2200	130	10	2000	110	0.45
2400	120	8	1300	70	0.42
2600	110	7	1000	60	0.48
2800	100	5	500	30	0.38
3000	80	3	200	10	0.30
3200	60	2	100	5	0.31

$W/S = 53\ lbs/ft^2$
$W/C_L S = 312\ lbs/ft^2$

TABLE 21

SUMMARY OF DATA USED IN THEORETICAL CALCULATIONS OF RECESSION RATES AS A FUNCTION OF FLUX-ENTHALPY CONDITIONS

Material Code	T^oR*	ϵ	ΔH_f** (BTU/lb)	Density (lb/ft³)	(gms / g. at.)	ΔS_f* (cal/g. at° K)
$HfB_{2.1}$(A-2)	6570	0.40	490	625	66.7	5.0
ZrB_2(A-3)	6335	0.37	840	350	37.6	5.0
HfB_2+20v/oSiC (A-4)	5700	0.48	495	585	57.5	5.0
Boride Z(A-5)	5300	0.55	705	355	37.5	5.0
$HfB_{2.1}$(A-6)	6570	0.50	490	665	66.7	5.0
HfB_2+20v/oSiC (A-7)	5700	0.48	480	565	59.0	5.0
ZrB_2+20v/oSiC (A-8)	5300	0.55	740	340	35.8	5.0
HfB_2+35v/oSiC (A-9)	5500	0.59	560	485	49.3	5.0
ZrB_2+SiC+C (A-10)	5500	0.62	1150	280	28.7	6.0
HfC+C(C-11)	6210	0.55	730	565	59.5	7.0
ZrC+C(C-12)	5725	0.45	1050	340	38.0	7.0
JTA(D-13)	5000	0.57	2000	190	17.5	7.0
JT0992(F-15)	5800	0.60	1400	290	28.8	7.0
JT0981(F-16)	5170	0.51	1880	195	19.2	7.0
WSi_2/W(G-18)	6570	0.28	70	1200	184.0	2.0
Sn-Al/Ta-W(G-19)	5890	0.46	65	1055	181.3	2.0
Hf-Ta-Mo(I-23)	4320	0.54	50	840	179.0	2.0
Ir/C(I-24)	4950	0.30	50	1400	192.0	2.0

* Estimated values.

** Calculated value, $\Delta H_f = T \Delta S_f$.

TABLE 22

CALCULATION OF TEMPERATURE GRADIENTS THROUGH ARC PLASMA TEST SAMPLE ZrB_2(A-3)-2MC

Input Values			Observed Values		
q	=	365 BTU/ft^2 sec	T_f	=	4930°R
i_e	=	3230 BTU/lb	T	=	3400°R at x = 101 mils
P_e	=	1.060 atm			
ϵ_S	=	ϵ = 0.47			
R	=	0.020 ft. (246 mils)			
L	=	0.035 ft. (429 mils)			
I	=	0.0011 ft. (14 mils)			
k_F	=	0.0001 BTU/ft sec°R for oxide			
k_S	=	0.0120 BTU/ft sec°R for boride			

x mils	Computed Temperature °R	x mils	Computed Temperature °R
0.0	4633	231	3325
21.0	3424	273	3314
42.0	3411	315	3306
63.0	3398	357	3300
105.0	3376	399	3297
126.0	3366	420	3297
168.0	3347		

TABLE 23

COMPARISON OF OBSERVED AND CALCULATED INTERNAL TEMPERATURE RESULTS

Test	T_f observed (^oR)	T(d mils) observed (^oR)	ϵ_S	$10^3 k_S$ (BTU/ft sec ^oR)	$10^3 k_F$ (BTU/ft sec ^oR)	R/L/I (mils)	$\frac{T_f\ (CALC)}{T_f\ (OBS)}$	$\frac{T(d)\ (CALC)}{T_f\ (CALC)}$	$\frac{T(d)\ (OBS)}{T_f\ (OBS)}$
ZrB_2 + SiC(A-8)									
-25M	3560	3310(96)	0.59	10.0	0.5	213/696/8	1.12	0.89	0.93
	q = 360 BTU/ft^2sec, i_e = 5280 BTU/lb, P_e = 1.01 atm								
-26M	3560	3060(395)	0.59	10.0	0.5	218/696/6	1.12	0.81	0.87
	q = 370 BTU/ft^2sec, i_e = 5430 BTU/lb, P_e = 1.01 atm								
-27R	3380	3100(102)	0.59	10.0	0.5	213/696/7	1.27	0.88	0.92
	q = 452 BTU/ft^2sec, i_e = 7970 BTU/lb, P_e = 0.117 atm								
-28R	4140	2680(400)	0.59	10.0	0.5	213/696/8	1.04	0.78	0.64
	q = 452 BTU/ft^2sec, i_e = 7350 BTU/lb, P_e = 0.111 atm								
-29M	3710	3260(96)	0.59	10.0	0.5	213/686/8	1.07	0.89	0.83
	q = 358 BTU/ft^2sec, i_e = 5330 BTU/lb, P_e = 1.00 atm								
-30MS	2975	2570(395)	0.59	10.0	0.5	214/688/6	1.30	0.82	0.85
	q = 350 BTU/ft^2sec, i_e = 4840 BTU/lb, P_e = 1.01 atm								
-31RS	3110	2820(95)	0.59	10.0	0.5	214/688/5	1.35	0.90	0.9[illegible]
	q = 440 BTU/ft^2sec, i_e = 7390 BTU/lb, P_e = 0.226 atm								
-32RS	3260	2720(399)	0.59	10.0	0.5	214/688/5	1.29	0.80	0.83
	q = 437 BTU/ft^2sec, i_e = 7270 BTU/lb, P_e = 0.228 atm								
ZrB_2(A-3)									
-2MC	4930	3400(101)	0.47	12.0	0.1	246/422/14	0.94	0.73	0.69
	q = 365 BTU/ft^2sec, i_e = 3230 BTU/lb, P_e = 1.05 atm								
-3MC	5170	3760(102)	0.47	12.0	0.1	246/429/31	0.99	0.60	0.73
	q = 460 BTU/ft^2sec, i_e = 3380 BTU/lb, P_e = 1.06 atm								

TABLE 24

COMPARISON OF OBSERVED AND CALCULATED INTERNAL TEMPERATURE RESULTS

Test	T_f observed (^oR)	T (d mils) observed (^oR)	ϵ_S	$10^3 k_S$ (BTU/ft sec ^oR)	$10^3 k_F$ (BTU/ft sec ^oR)	R/L/I (mils)	$\frac{T_f\ (CALC)}{T_f\ (OBS)}$	$\frac{T(d)\ (CALC)}{T_f\ (CALC)}$	$\frac{T(d)\ (OBS)}{T_f\ (OBS)}$
HfB_2+SiC(A-7)									
-36MH	4370	3980(109)	0.55	8.0	0.5	219/699/13	1.00	0.84	0.91
	q = 513 BTU/ft^2sec, i_e = 3500 BTU/lb, P_e = 1.02 atm								
-37MH	4230	3570(405)	0.55	8.0	0.5	219/690/10	1.02	0.75	0.84
	q = 495 BTU/ft^2sec, i_e = 3640 BTU/lb, P_e = 1.02 atm								
-39RH	3190	2860(401)	0.55	8.0	0.5	219/682/0	1.34	0.80	0.90
	q = 487 BTU/ft^2sec, i_e = 6540 BTU/lb, P_e = 0.162 atm								
-44MS	3220	3060(101)	0.55	8.0	0.5	219/684/0	1.31	0.94	0.95
	q = 493 BTU/ft^2sec, i_e = 4360 BTU/lb, P_e = 1.04 atm								
-45MS	3230	2740(399)	0.55	8.0	0.5	219/690/0	1.33	0.80	0.85
	q = 522 BTU/ft^2sec, i_e = 4580 BTU/lb, P_e = 1.04 atm								
-46RS	3730	3160(97)	0.55	8.0	0.5	219/702/0	1.14	0.94	0.85
	q = 503 BTU/ft^2sec, i_e = 5750 BTU/lb, P_e = 0.169 atm								
-47RS	3660	2830(400)	0.55	8.0	0.5	219/738/0	1.16	0.79	0.77
	q = 489 BTU/ft^2sec, i_e = 6290 BTU/lb, P_e = 0.169 atm								
-48RH	2970	2840(100)	0.55	8.0	0.5	488/690/0	1.59	0.95	0.96
	q = 492 BTU/ft^2sec, i_e = 7030 BTU/lb, P_e = 0.145 atm								
-50RH	2940	2780(401)	0.55	8.0	0.5	488/690/0	1.61	0.86	0.95
	q = 492 BTU/ft^2sec, i_e = 7250 BTU/lb, P_e = 0.150 atm								
-49RHS	3310	3010(101)	0.55	8.0	0.5	488/690/0	1.44	0.95	0.91
	q = 512 BTU/ft^2sec, i_e = 6800 BTU/lb, P_e = 0.167 atm								
-51RHS	3180	2640(399)	0.55	8.0	0.5	488/675/0	1.48	0.86	0.83
	q = 497 BTU/ft^2sec, i_e = 6510 BTU/lb, P_e = 0.167 atm								

TABLE 25

COMPARISON OF OBSERVED AND CALCULATED INTERNAL TEMPERATURE RESULTS

Test	T_f observed (^oR)	T (d mils) observed (^oR)	ϵ_S	$0^3 k_S$ (BTU/ft sec ^oR)	$10^3 k_F$ (BTU/ft sec ^oR)	R/L/I (mils)	$\frac{T_f \text{ (CALC)}}{T_f \text{ (OBS)}}$	$\frac{T(d) \text{ (CALC)}}{T_f \text{ (CALC)}}$	$\frac{T(d) \text{ (OBS)}}{T_f \text{ (OBS)}}$
HfB_2 + SiC (A-7)									
-40M	4670	3940(100)	0.55	8.0	0.5	219/689/14	0.96	0.83	0.84
	q = 495 BTU/ft^{2}sec, i_e = 4390 BTU/lb, P_e = 1.04 atm								
-41M	5010	3810(397)	0.55	8.0	0.5	219/687/62	0.95	0.66	0.76
	q = 502 BTU/ft^{2}sec, i_e = 4400 BTU/lb, P_e = 1.04 atm								
-42R	3110	2860(102)	0.55	8.0	0.5	219/690/0	1.39	0.93	0.92
	q = 498 BTU/ft^{2}sec, i_e = 7140 BTU/lb, P_e = 0.138 atm								
-43R	3260	2700(400)	0.55	8.0	0.5	219/690/0	1.33	0.79	0.83
	q = 503 BTU/ft^{2}sec, i_e = 7520 BTU/lb, P_e = 0.134 atm								
ZrB_2+SiC+C(A-10)									
-38M	3840	3550(96)	0.62	10.0	0.5	219/690/6	1.02	0.90	0.92
	q = 400 BTU/ft^{2}sec, i_e = 3870 BTU/lb, P_e = 1.02 atm								
-39M	4745	3440(389)	0.62	10.0	0.5	213/692/16	0.86	0.76	0.72
	q = 400 BTU/ft^{2}sec, i_e = 3990 BTU/lb, P_e = 1.02 atm								
-40R	5020	3360(101)	0.62	10.0	0.5	219/690/12	0.87	0.84	0.67
	q = 495 BTU/ft^{2}sec, i_e = 6320 BTU/lb, P_e = 0.147 atm								
-41R	5170	2930(400)	0.62	10.0	0.5	213/690/17	0.87	0.73	0.57
	q = 495 BTU/ft^{2}sec, i_e = 6460 BTU/lb, P_e = 0.147 atm								
RVA(B-5)									
-31M	3310	3100(202)	0.52	6.5	---	251/670/0	0.90	0.94	0.94
	q = 135 BTU/ft^{2}sec, i_e = 2530 BTU/lb, P_e = 1.00 atm								
-32M	3480	2850(463)	0.52	6.5	---	251/671/0	0.87	0.89	0.82
	q = 135 BTU/ft^{2}sec, i_e = 2930 BTU/lb, P_e = 1.00 atm								

TABLE 26

COMPARISON OF OBSERVED AND CALCULATED INTERNAL TEMPERATURE RESULTS

Test	T_f observed (^oR)	T (d mils) observed (^oR)	ϵ_S	$10^3 k_S$ (BTU/ft sec ^oR)	$10^3 k_F$ (BTU/ft sec ^oR)	R/L/I (mils)	$\frac{T_f\ (CALC)}{T_f\ (OBS)}$	$\frac{T(d)\ (CALC)}{T_f\ (CALC)}$	$\frac{T(d)\ (OBS)}{T_f\ (OBS)}$
ZrB_2+SiC+C(A-10)									
-34MH	3975	3630(102)	0.62	10.0	0.5	219/691/18	1.04	0.82	0.91
	q = 416 BTU/ft^{2}sec, i_e = 3950 BTU/lb, P_e = 1.01 atm								
-35MH	3960	3320(391)	0.62	10.0	0.5	219/686/5	0.98	0.82	0.84
	q = 420 BTU/ft^{2}sec, i_e = 3500 BTU/lb, P_e = 1.01 atm								
-36RH	3770	3280(109)	0.62	10.0	0.5	219/698/5	1.13	0.89	0.87
	q = 492 BTU/ft^{2}sec, i_e = 7250 BTU/lb, P_e = 0.147 atm								
-37RH	3740	2980(393)	0.62	10.0	0.5	219/682/5	1.14	0.79	0.80
	q = 482 BTU/ft^{2}sec, i_e = 7710 BTU/lb, P_e = 0.144 atm								
-42MS	2920	2880(102)	0.62	10.0	0.5	214/688/0	1.29	0.95	0.99
	q = 393 BTU/ft^{2}sec, i_e = 4000 BTU/lb, P_e = 1.03 atm								
-43MS	3060	2600(395)	0.62	10.0	0.5	214/693/0	1.24	0.85	0.85
	q = 403 BTU/ft^{2}sec, i_e = 4040 BTU/lb, P_e = 1.03 atm								
-44RS	4750	3220(94)	0.62	10.0	0.5	214/681/11	0.93	0.85	0.68
	q = 495 BTU/ft^{2}sec, i_e = 7400 BTU/lb, P_e = 0.226 atm								
-45RS	5210	2870(399)	0.62	10.0	0.5	213/684/14	0.87	0.73	0.55
	q = 498 BTU/ft^{2}sec, i_e = 7470 BTU/lb, P_e = 0.229 atm								
-46RH	3110	3020(108)	0.62	10.0	0.5	488/695/0	1.48	0.96	0.97
	q = 501 BTU/ft^{2}sec, i_e = 7220 BTU/lb, P_e = 0.155 atm								
-48RH	3000	2770(404)	0.62	10.0	0.5	488/693/0	1.51	0.88	0.92
	q = 492 BTU/ft^{2}sec, i_e = 6350 BTU/lb, P_e = 0.155 atm								
-47RHS	4830	3210(103)	0.62	10.0	0.5	488/692/13	0.98	0.88	0.66
	q = 507 BTU/ft^{2}sec, i_e = 6010 BTU/lb, P_e = 0.167 atm								
-49RHS	4190	2830(392)	0.62	10.0	0.5	488/671/5	1.11	0.85	0.68
	q = 522 BTU/ft^{2}sec, i_e = 6010 BTU/lb, P_e = 0.167 atm								

TABLE 27

COMPARISON OF OBSERVED AND CALCULATED INTERNAL TEMPERATURE RESULTS

Test	T_f observed (^oR)	T(d mils) observed (^oR)	ϵ_S	$10^3 k_S$ (BTU/ft sec ^oR)	$10^3 k_F$ (BTU/ft sec ^oR)	R/L/I (mils)	$\frac{T_f\ (CALC)}{T_f\ (OBS)}$	$\frac{T(d)\ (CALC)}{T_f\ (CALC)}$	$\frac{T(d)\ (OBS)}{T_f\ (OBS)}$
Hf-Ta-Mo(I-23)									
-45MS	3700	3170(99)	0.60	7.5	0.5	196/793/11	1.11	0.85	0.86
	$q = 445$ BTU/ft^{2}sec, $i_e = 3700$ BTU/lb, $P_e = 1.05$ atm								
-46MS	4210	2790(393)	0.60	7.5	0.5	199/794/13	1.01	0.72	0.66
	$q = 470$ BTU/ft^{2}sec, $i_e = 3760$ BTU/lb, $P_e = 1.05$ atm								
-47RS	4840	3160(102)	0.60	7.5	0.5	196/700/37	1.00	0.70	0.65
	$q = 498$ BTU/ft^{2}sec, $i_e = 7340$ BTU/lb, $P_e = 0.222$ atm								
-48RS	4840	2720(400)	0.60	7.5	0.5	199/700/26	0.98	0.66	0.58
	$q = 498$ BTU/ft^{2}sec, $i_e = 7090$ BTU/lb, $P_e = 0.229$ atm								
WSi_2/W(G-18)									
-17M	3600	3310(102)	0.58	16.7	2.0	252/455/4	1.04	0.97	0.92
	$q = 320$ BTU/ft^{2}sec, $i_e = 3150$ BTU/lb, $P_e = 1.02$ atm								
-18M	3490	3110(200)	0.58	16.7	2.0	252/444/4	1.08	0.96	0.89
	$q = 316$ BTU/ft^{2}sec, $i_e = 3280$ BTU/lb, $P_e = 1.02$ atm								
-19MS	2860	2770(96)	0.58	16.7	2.0	252/444/4	1.31	0.97	0.97
	$q = 310$ BTU/ft^{2}sec, $i_e = 3380$ BTU/lb, $P_e = 1.02$ atm								
-20MS	2760	2620(200)	0.58	16.7	2.0	253/447/4	1.35	0.96	0.95
	$q = 306$ BTU/ft^{2}sec, $i_e = 3160$ BTU/lb, $P_e = 1.02$ atm								

TABLE 28

COMPARISON OF OBSERVED AND CALCULATED
INTERNAL TEMPERATURE RESULTS

Test	T_f observed (°R)	T (dmils) observed (°R)	ϵ_S	$10^3 k_S$ (BTU/ft sec °R)	$10^3 k_F$ (BTU/ft sec °R)	R/L/I (mils)	$\frac{T_f\ (CALC)}{T_f\ (OBS)}$	$\frac{T(d)\ (CALC)}{T_f\ (CALC)}$	$\frac{T(d)\ (OBS)}{T_f\ (OBS)}$
Hf-Ta-Mo (I-23)									
-54M	4650	3560(106)	0.60	7.5	0.5	252/764/42	0.98	0.72	0.76
	q = 455 BTU/ft²sec, i_e = 3800 BTU/lb, P_e = 1.04 atm								
-55M	4800	3260(408)	0.60	7.5	0.5	254/795/36	0.94	0.67	0.68
	q = 455 BTU/ft²sec, i_e = 3820 BTU/lb, P_e = 1.04 atm								
-43R	4530	3560(120)	0.60	7.5	0.5	200/750/26	0.98	0.76	0.79
	q = 403 BTU/ft²sec, i_e = 7690 BTU/lb, P_e = 0.104 atm								
-1MC	5220	3990(97)	0.60	7.5	0.5	251/443/46	0.86	0.76	0.76
	q = 425 BTU/ft²sec, i_e = 3220 BTU/lb, P_e = 1.05 atm								
-2MC	5310	3640(93)	0.60	7.5	0.5	252/448/69	0.90	0.68	0.65
	q = 505 BTU/ft²sec, i_e = 3350 BTU/lb, P_e = 1.05 atm								
-4MC	5395	3840(99)	0.60	7.5	0.5	252/437/99	0.90	0.64	0.71
	q = 480 BTU/ft²sec, i_e = 3560 BTU/lb, P_e = 1.06 atm								
-53MH	4460	3690(100)	0.60	7.5	0.5	252/721/57	1.03	0.69	0.83
	q = 452 BTU/ft²sec, i_e = 3560 BTU/lb, P_e = 1.02 atm								
-38MH	4680	3330(398)	0.60	7.5	0.5	257/752/48	0.95	0.65	0.71
	q = 435 BTU/ft²sec, i_e = 3220 BTU/lb, P_e = 1.04 atm								
-39RH	4160	3680(100)	0.60	7.5	0.5	252/670/22	1.07	0.81	0.88
	q = 412 BTU/ft²sec, i_e = 6740 BTU/lb, P_e = 0.137 atm								
-40RH	4150	3300(410)	0.60	7.5	0.5	253/710/22	1.06	0.72	0.80
	q = 388 BTU/ft²sec, i_e = 6950 BTU/lb, P_e = 0.132 atm								
-49RH	4270	3460(206)	0.60	7.5	0.5	500/860/23	1.10	0.80	0.81
	q = 408 BTU/ft²sec, i_e = 7480 BTU/lb, P_e = 0.111 atm								
-51RH	4340	3240(400)	0.60	7.5	0.5	500/968/24	1.06	0.74	0.75
	q = 398 BTU/ft²sec, i_e = 6900 BTU/lb, P_e = 0.114 atm								
-50RHS	4370	3370(104)	0.60	7.5	0.5	500/905/25	1.04	0.83	0.77
	q = 402 BTU/ft²sec, i_e = 5750 BTU/lb, P_e = 0.115 atm								
-52RHS	4500	2980(398)	0.60	7.5	0.5	500/1035/26	1.01	0.74	0.66
	q = 398 BTU/ft²sec, i_e = 5890 BTU/lb, P_e = 0.118 atm								

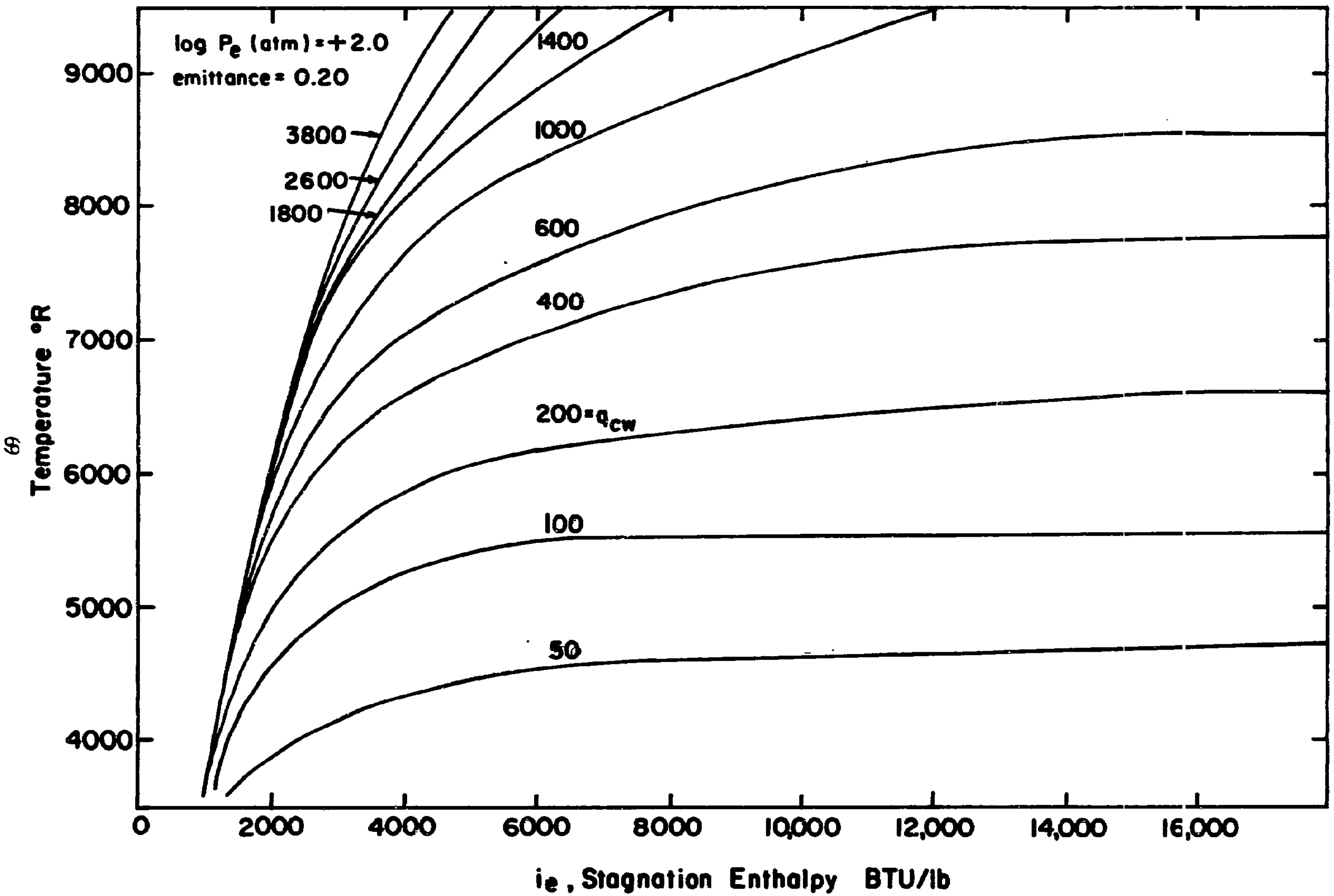

Figure 1. Surface Temperature-Heat Flux Relations As A Function of Stagnation Pressure, Enthalpy And Surface Emittance.

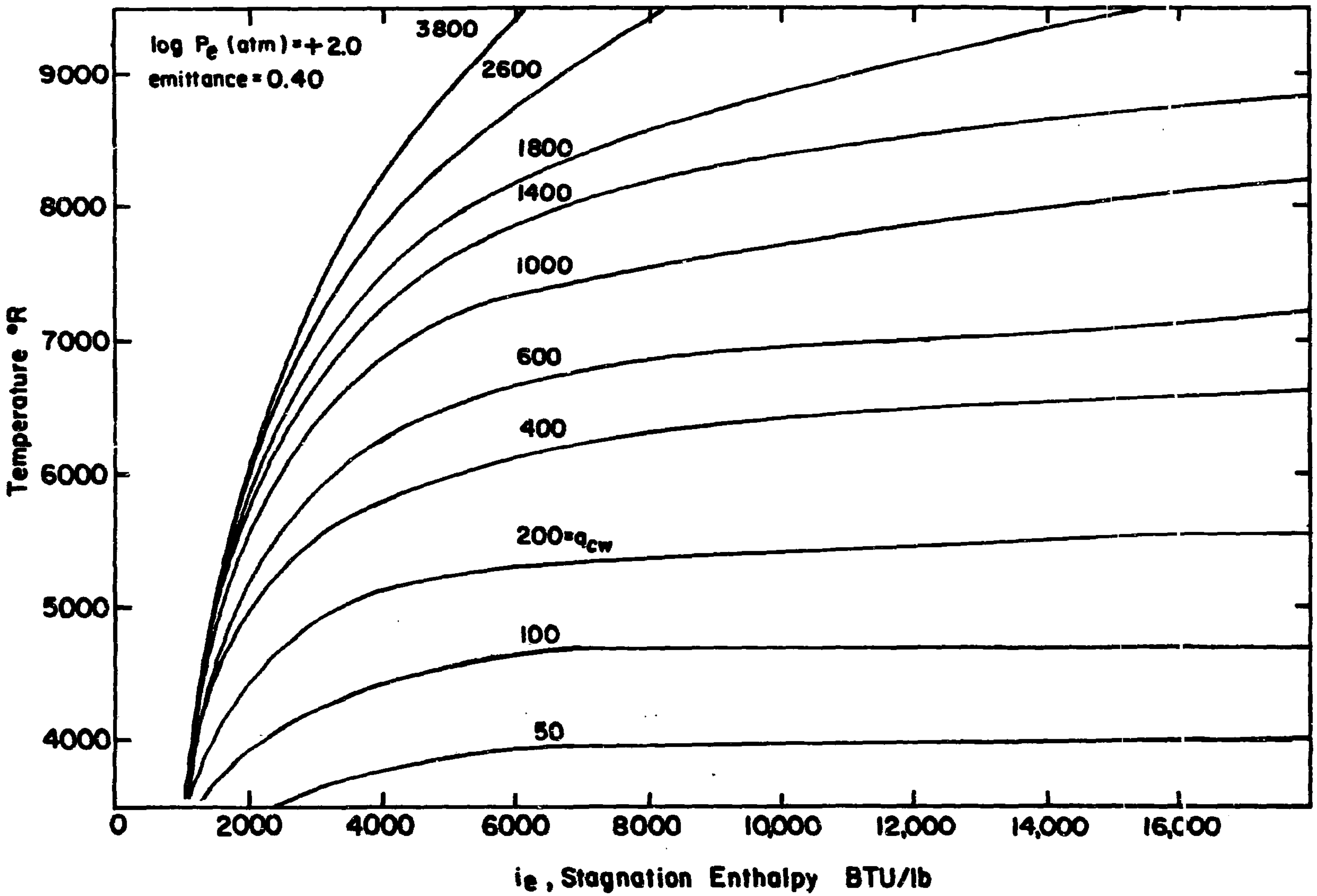

Figure 2. Surface Temperature-Heat Flux Relations As A Function of Stagnation Pressure, Enthalpy And Surface Emittance.

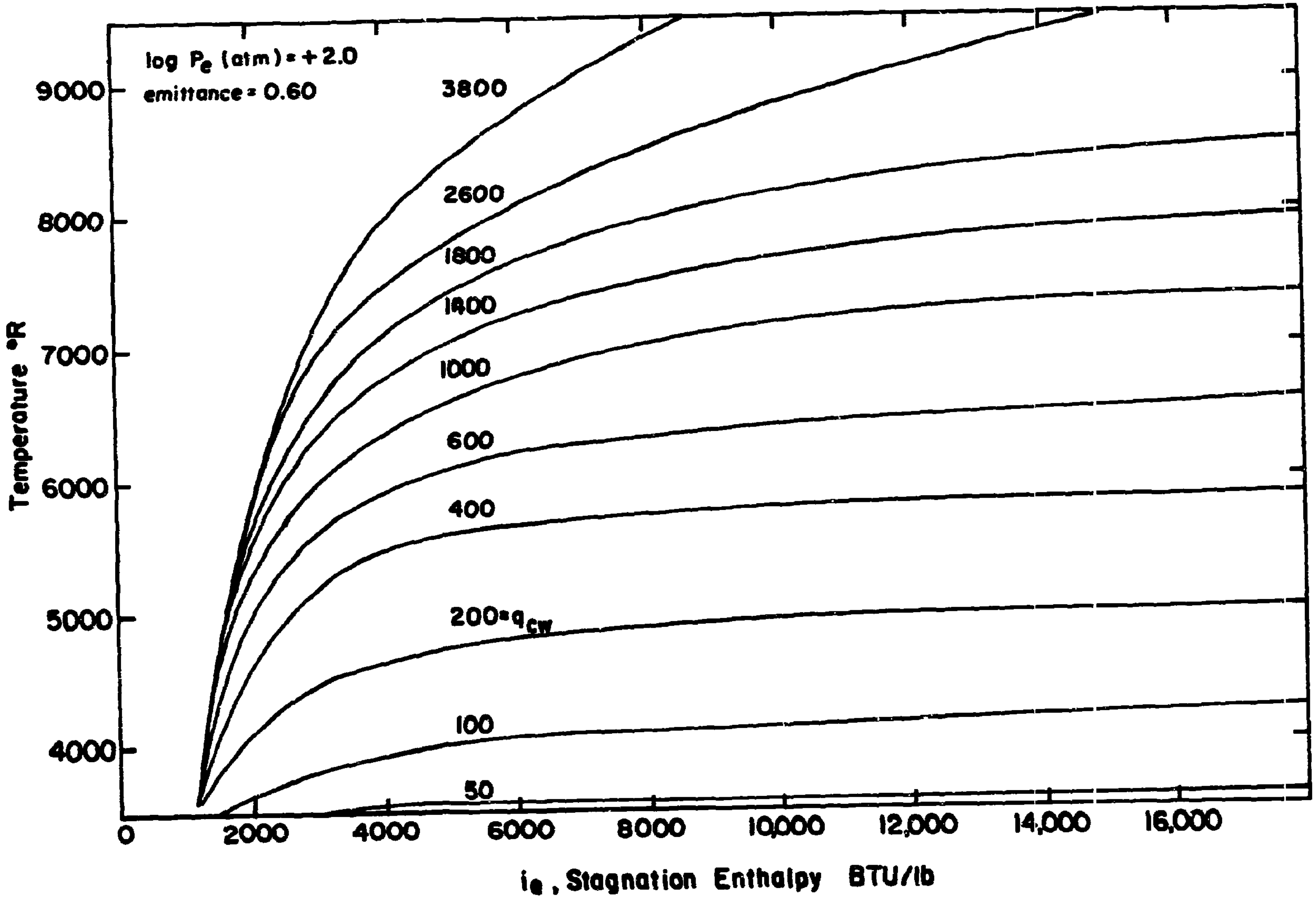

Figure 3. Surface Temperature-Heat Flux Relations As A Function of Stagnation Pressure, Enthalpy And Surface Emittance.

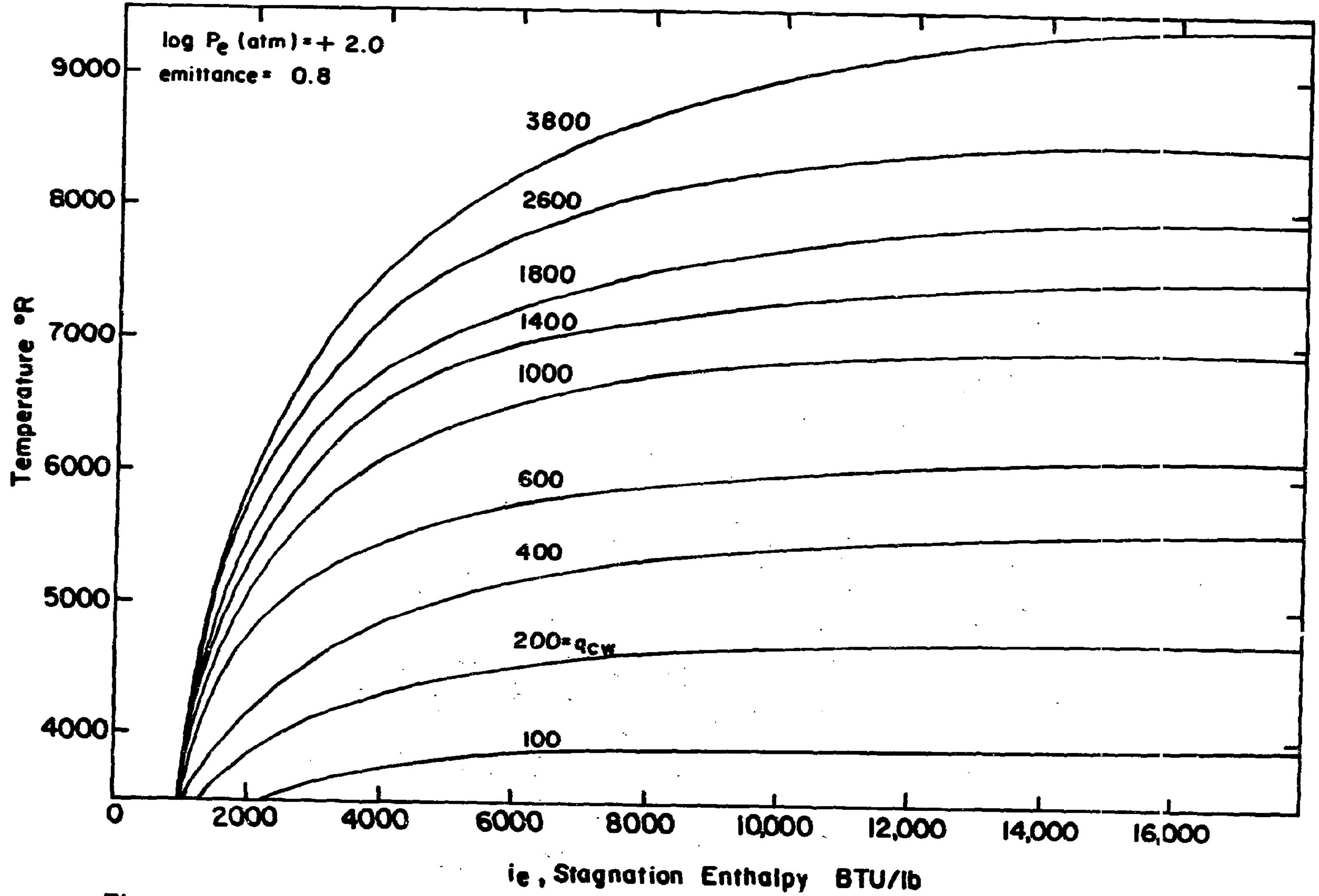

Figure 4. Surface Temperature-Heat Flux Relations As A Function of Stagnation Pressure, Enthalpy And Surface Emittance.

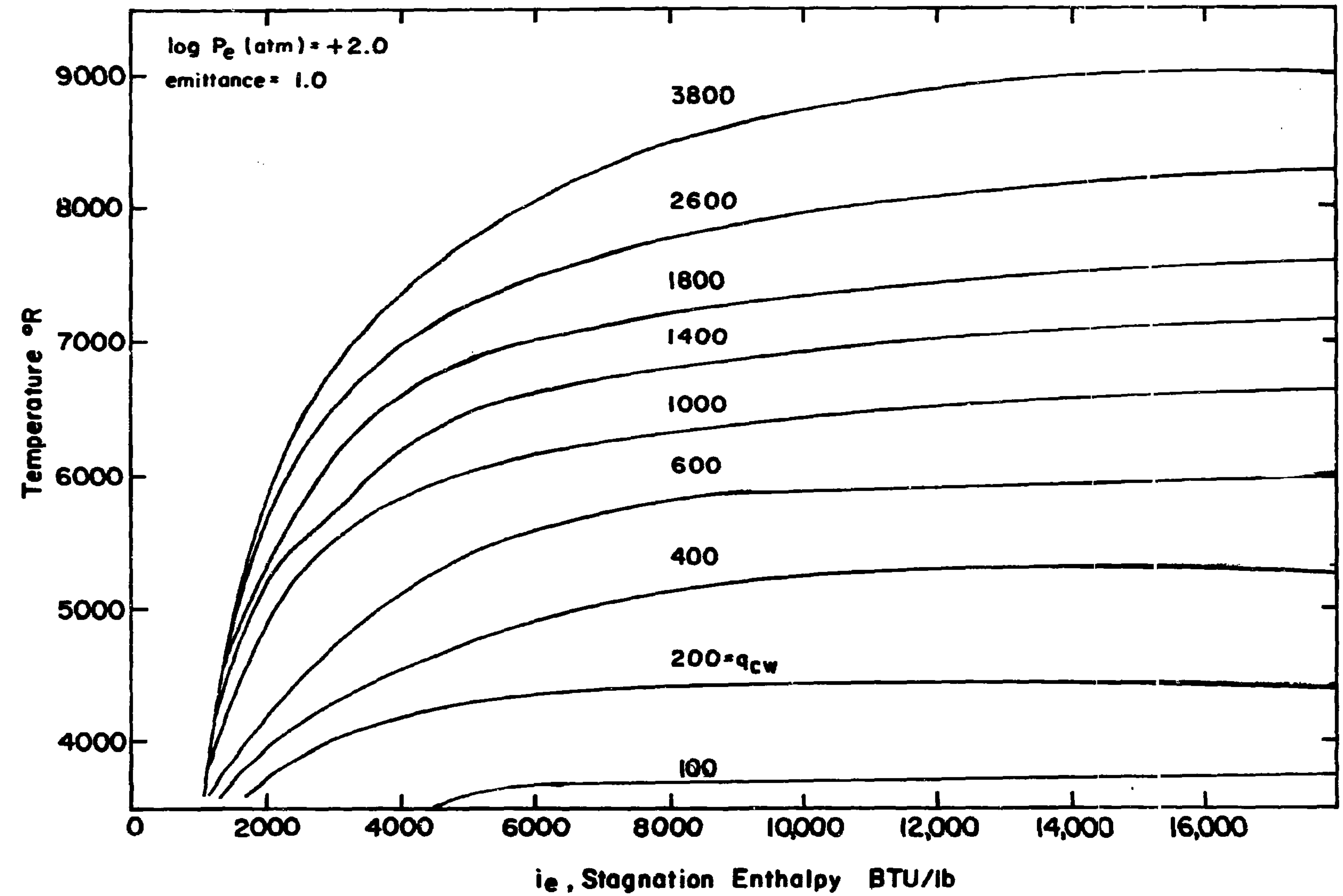

Figure 5. Surface Temperature-Heat Flux Relations As A Function of Stagnation Pressure, Enthalpy And Surface Emittance.

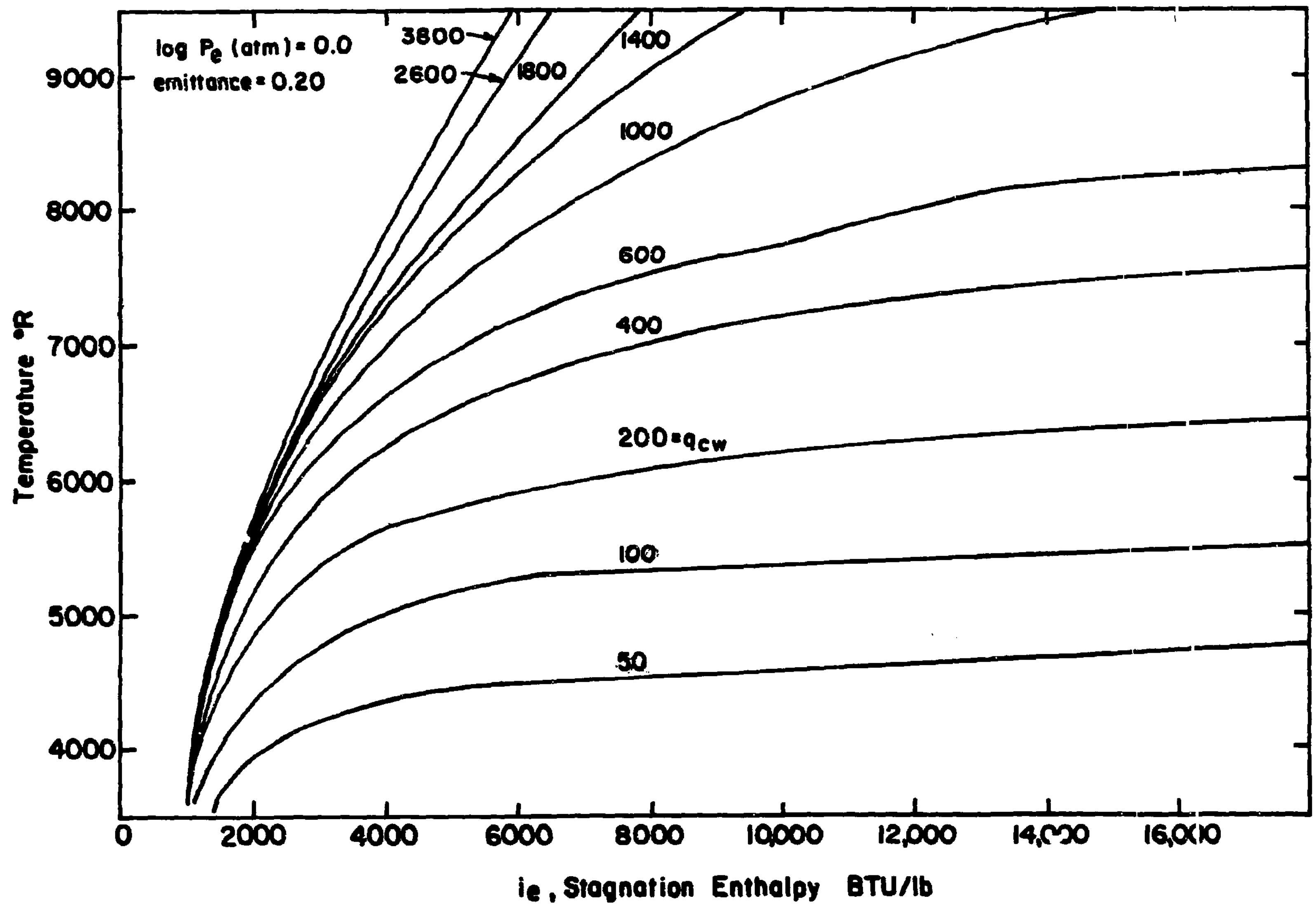

Figure 6.. Surface Temperature-Heat Flux Relations As A Function of Stagnation Pressure, Enthalpy and Surface Emittance.

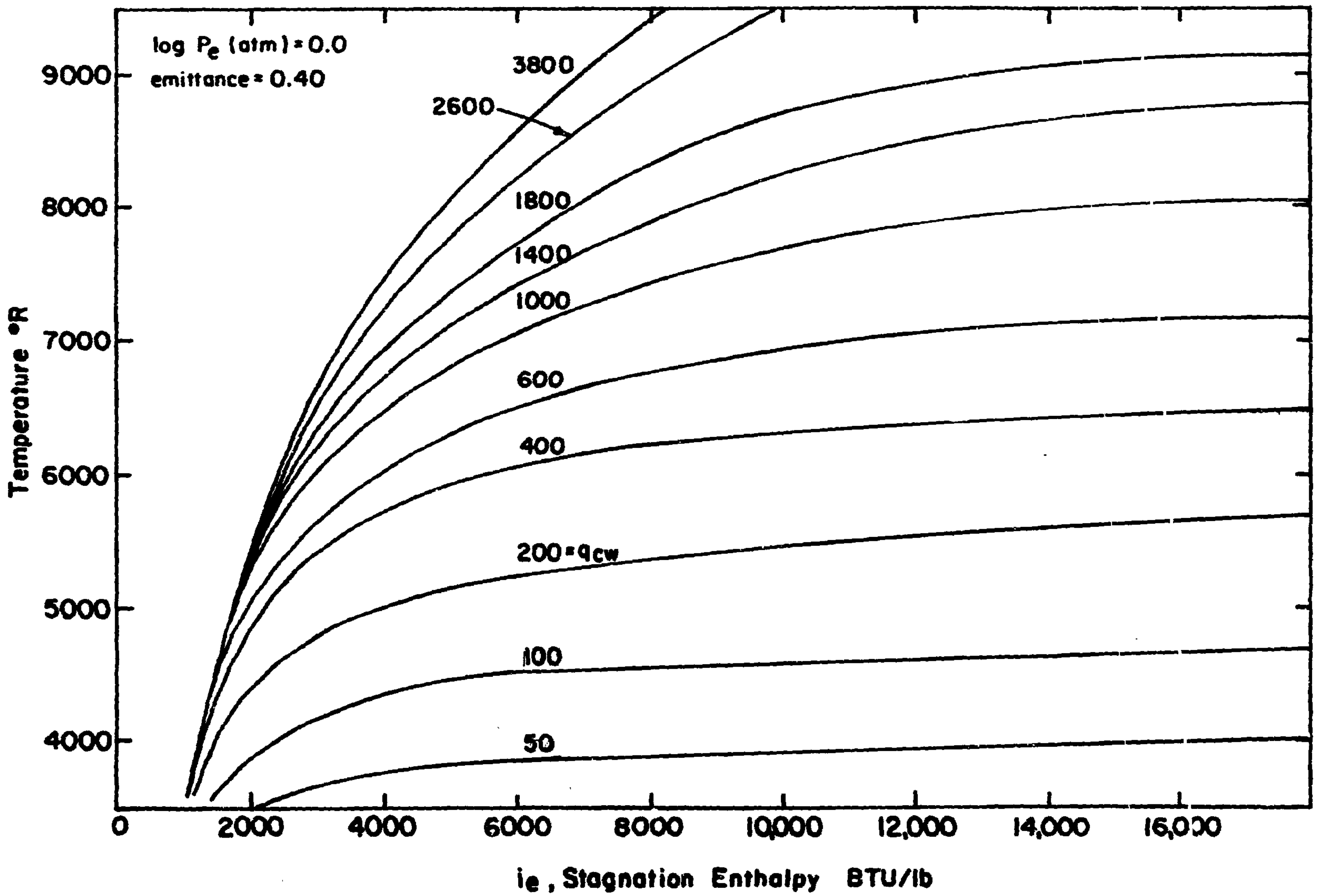

Figure 7. Surface Temperature-Heat Flux Relations As A Function of Stagnation Pressure, Enthalpy And Surface Emittance.

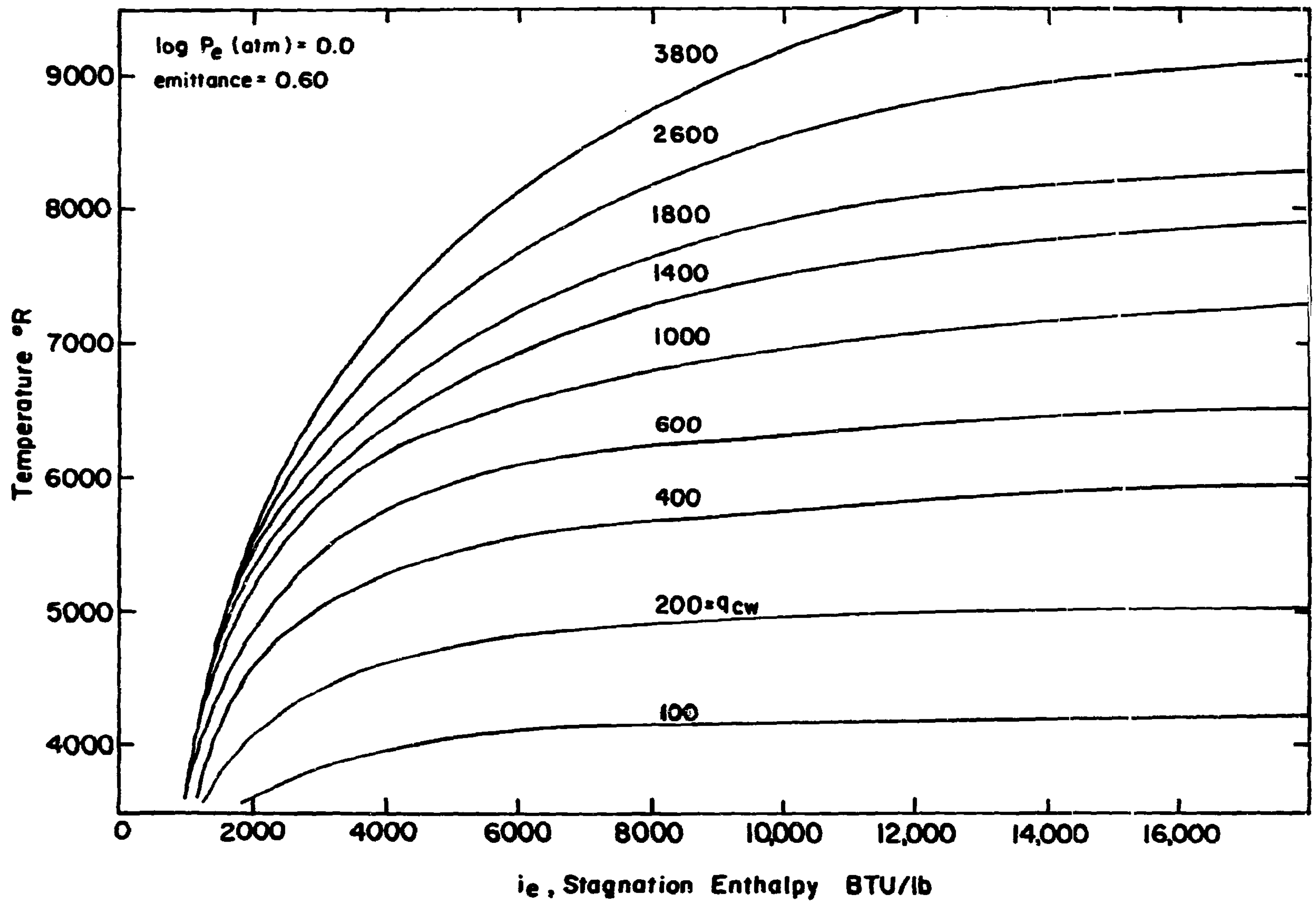

Figure 8. Surface Temperature-Heat Flux Relations As A Function of Stagnation Pressure, Enthalpy And Surface Emittance.

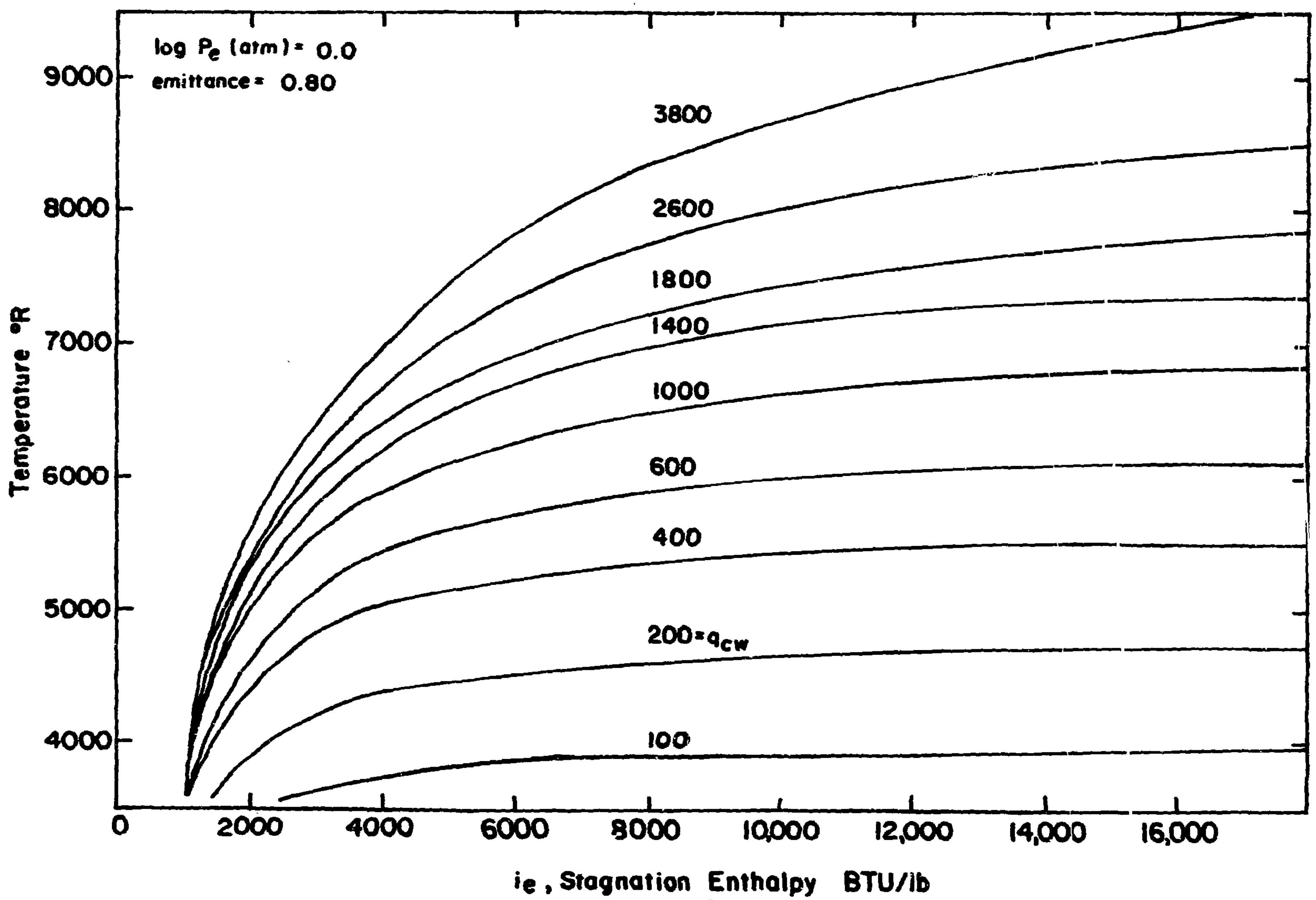

Figure 9. Surface Temperature-Heat Flux Relations As A Function of Stagnation Pressure, Enthalpy And Surface Emittance.

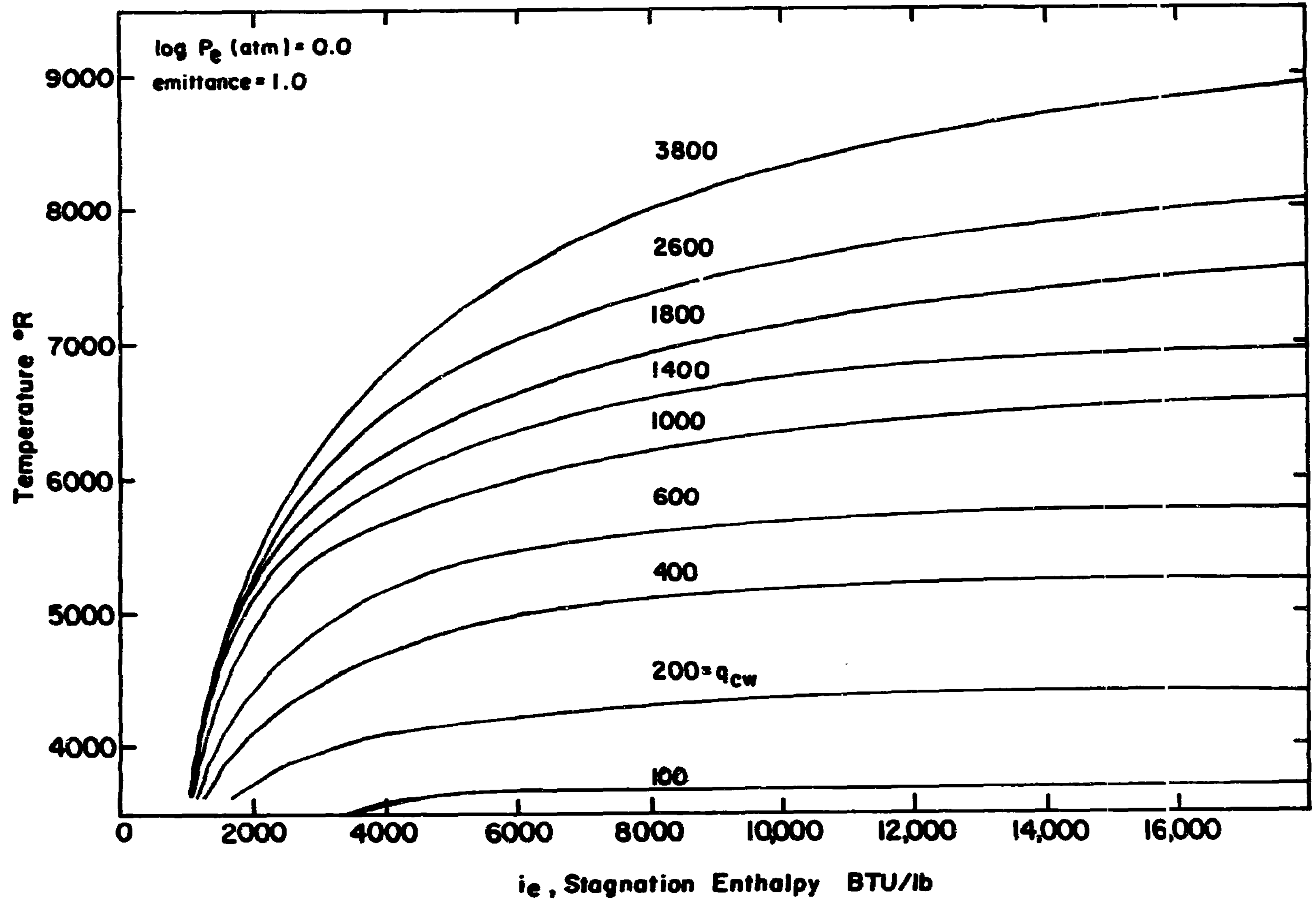

Figure 10. Surface Temperature-Heat Flux Relations As A Function of Stagnation Pressure, Enthalpy And Surface Emittance.

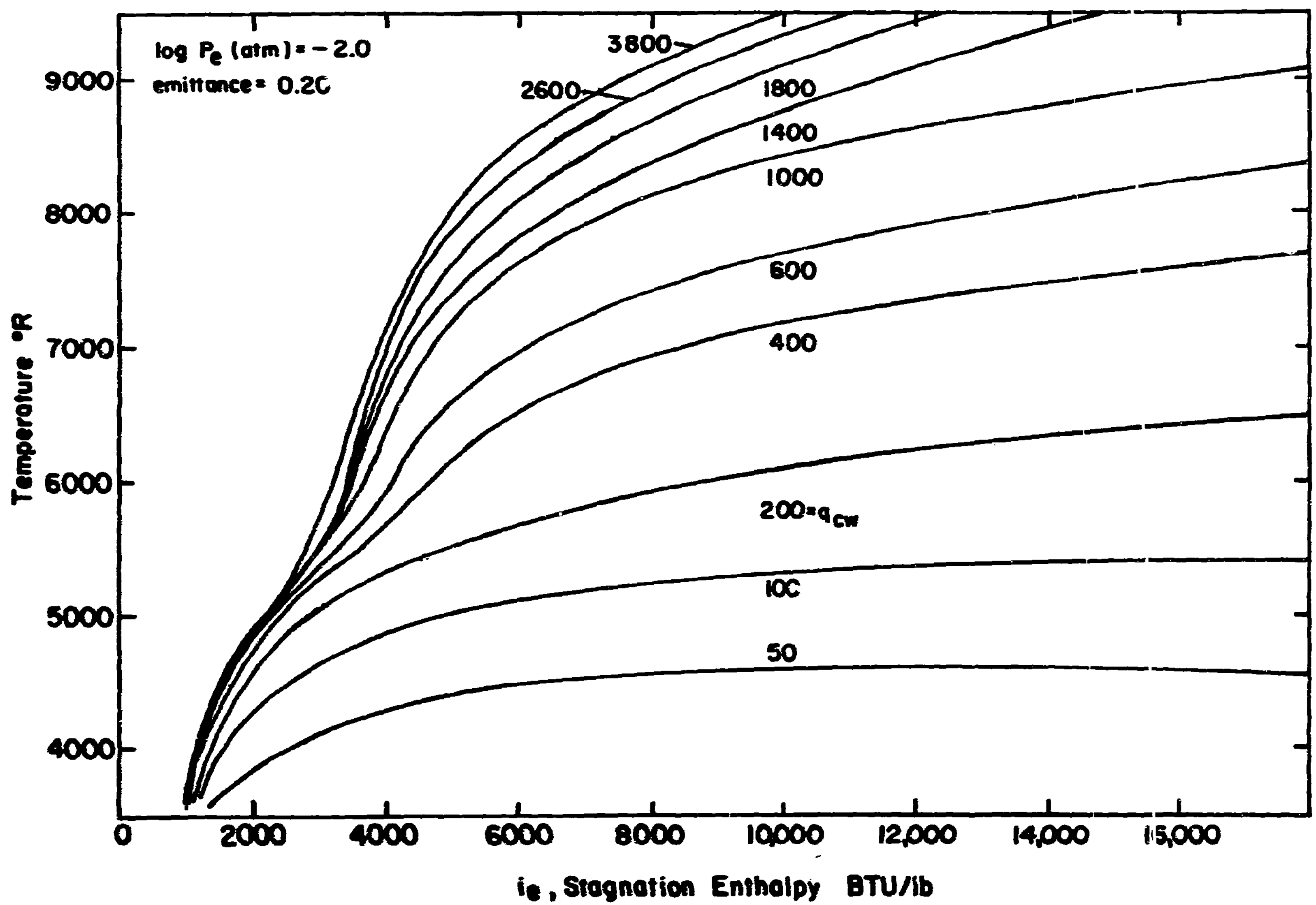

Figure 11. Surface Temperature-Heat Flux Relations As A Function of Stagnation Pressure, Enthalpy And Surface Emittance.

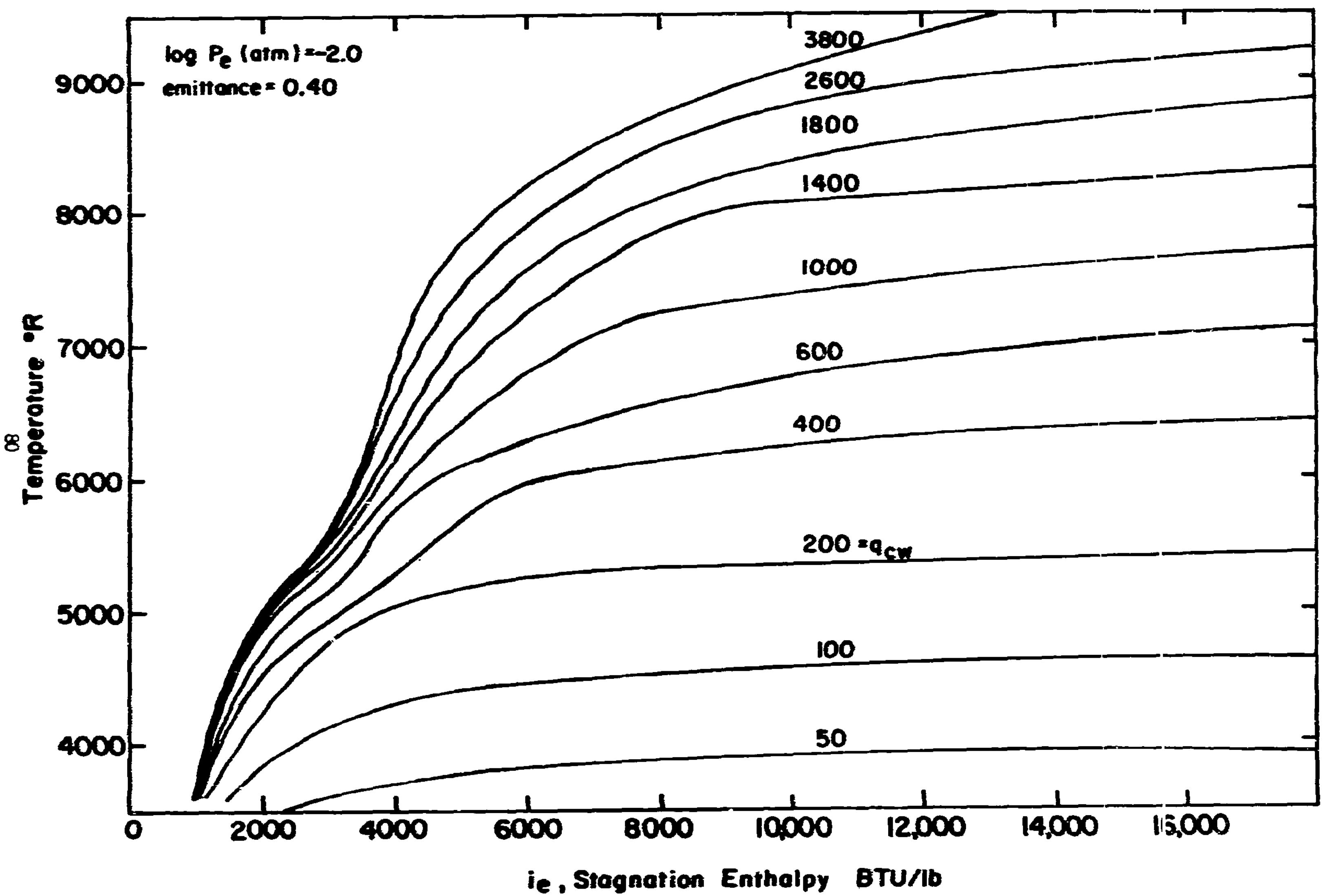

Figure 12.. Surface Temperature-Heat Flux Relations As A Function of Stagnation Pressure, Enthalpy And Surface Emittance.

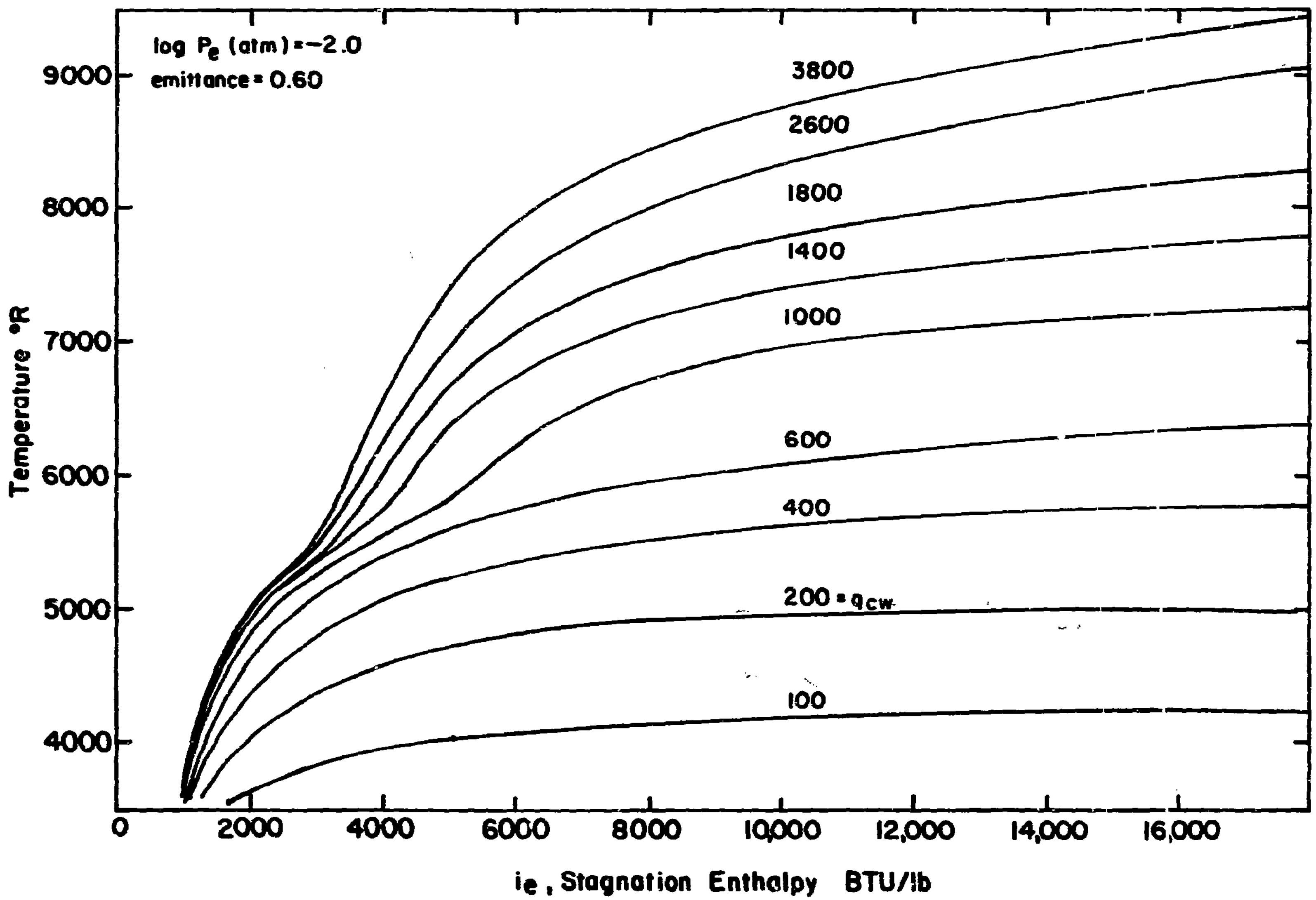

Figure 13. Surface Temperature-Heat Flux Relations As A Function of Stagnation Pressure, Enthalpy And Surface Emittance.

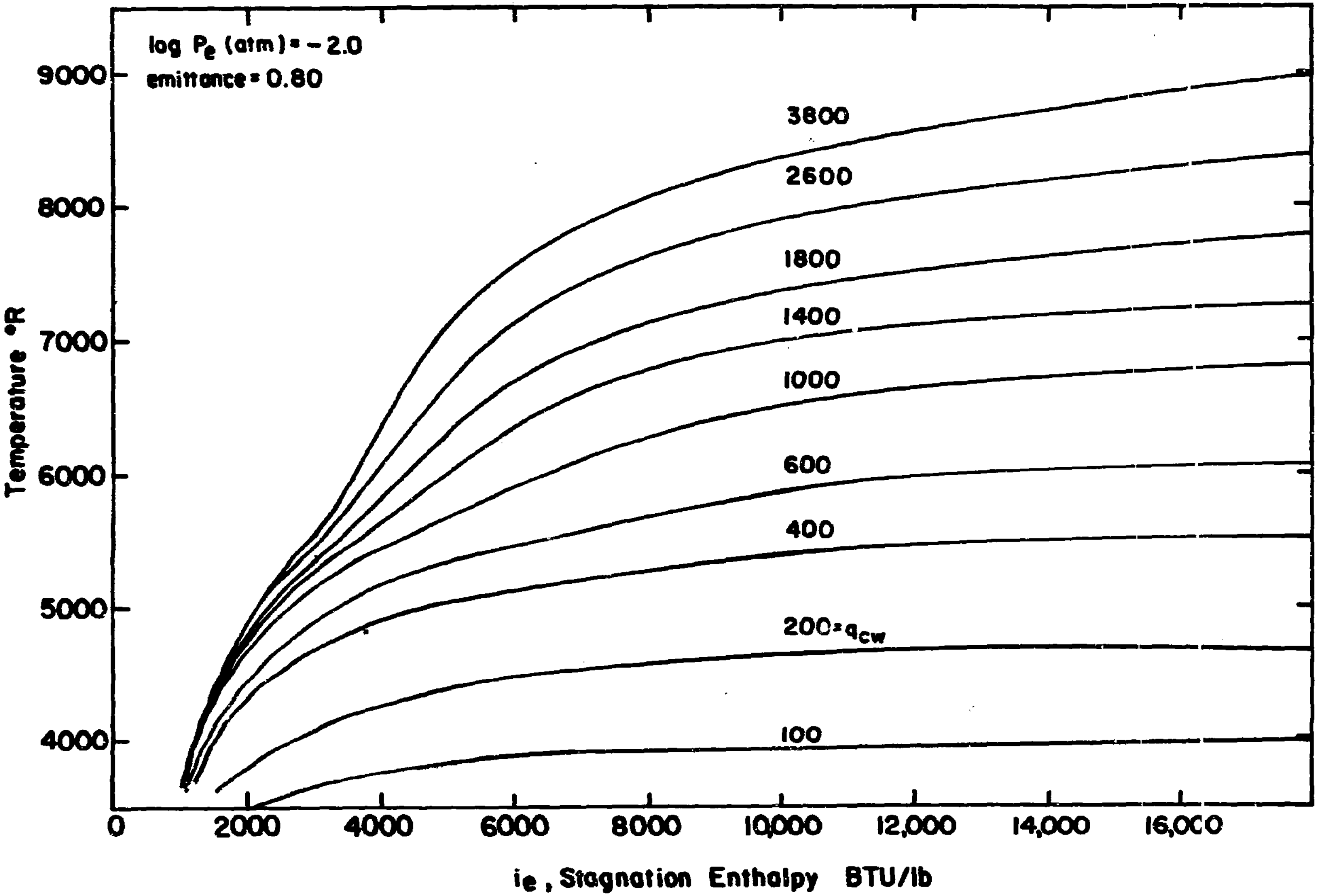

Figure 14. Surface Temperature-Heat Flux Relations As A Function of Stagnation Pressure, Enthalpy And Surface Emittance.

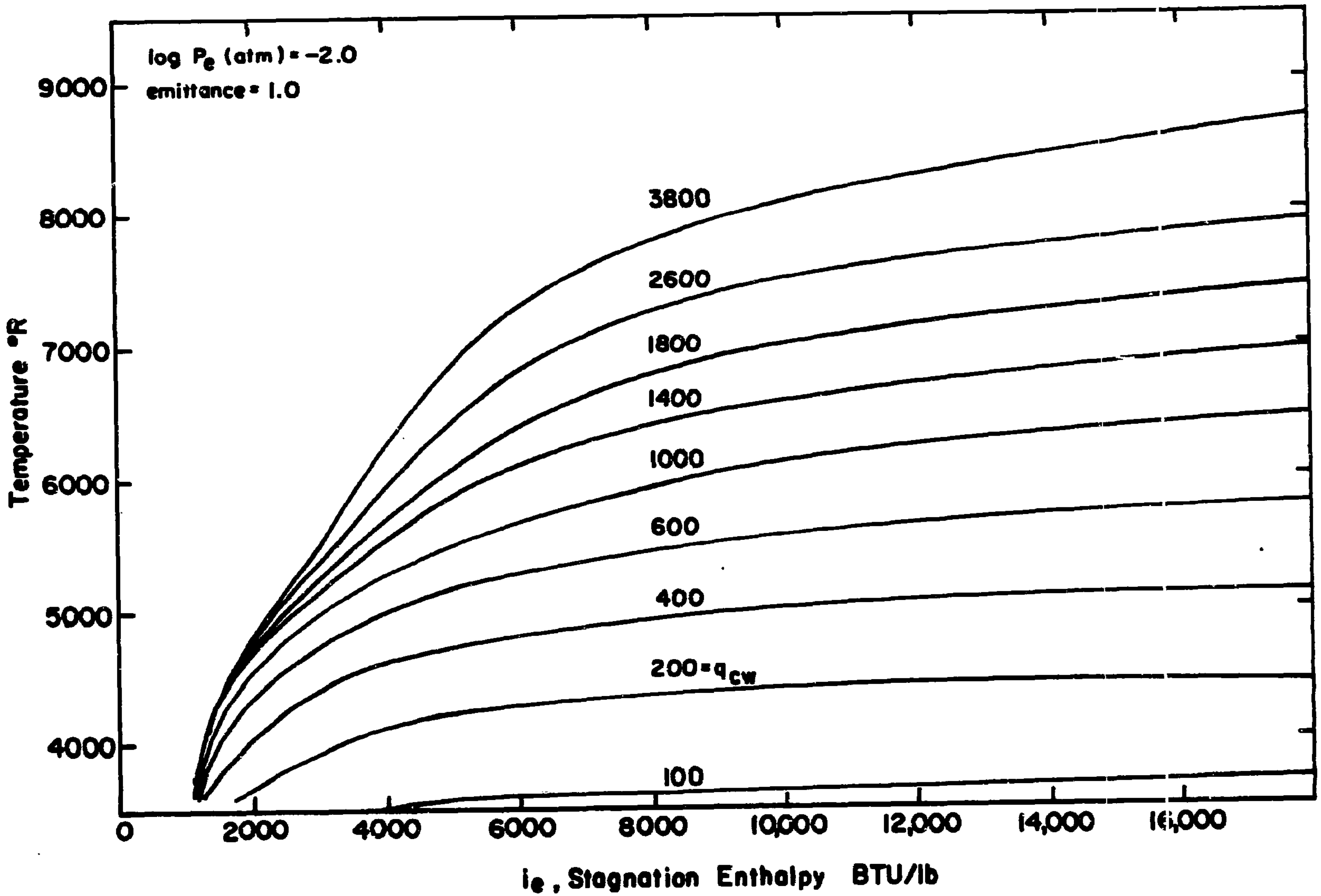

Figure 15. Surface Temperature-Heat Flux Relations As A Function of Stagnation Pressure, Enthalpy And Surface Emittance.

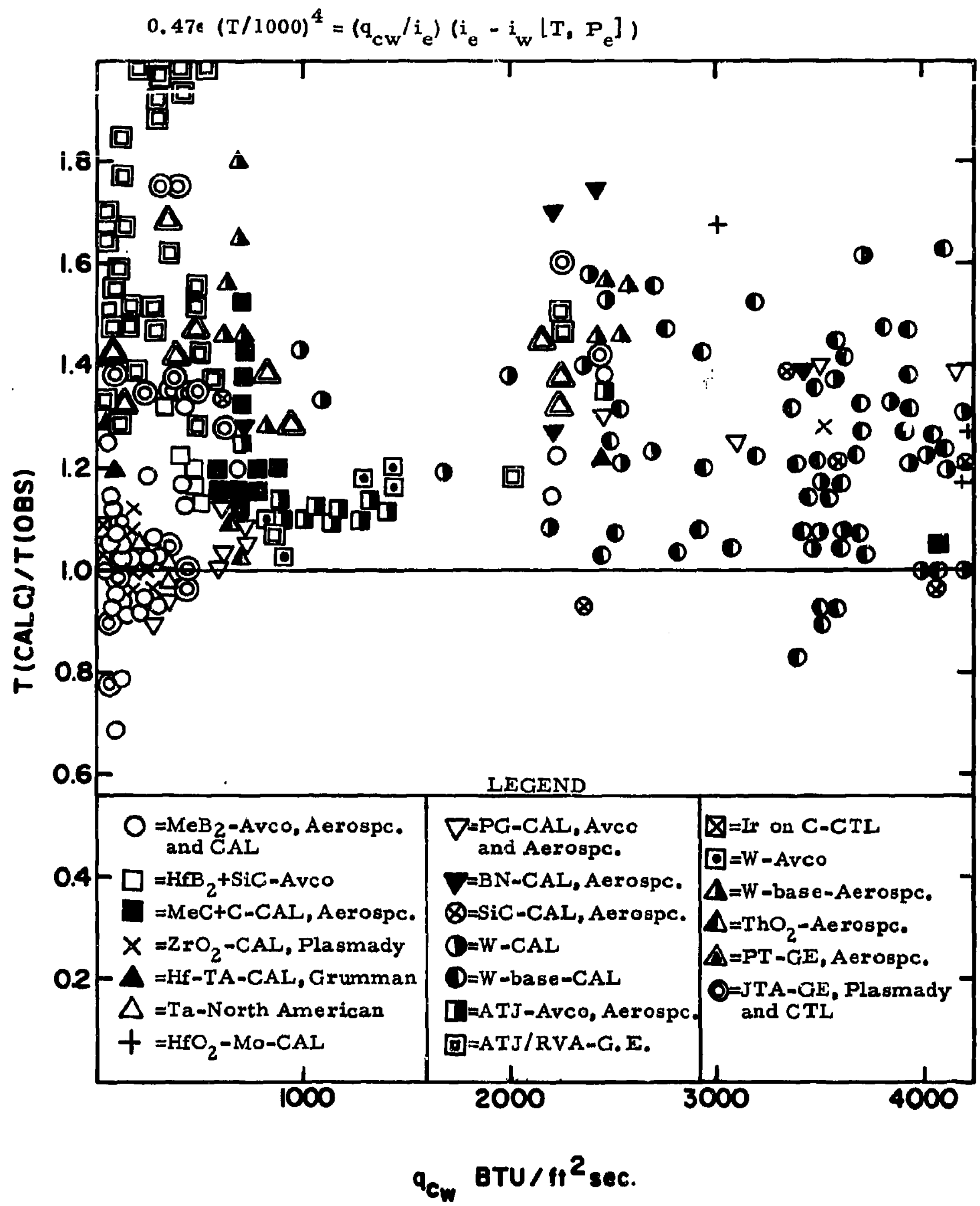

Figure 16. Ratio of Calculated to Observed Surface Temperatures Based on the Cold Wall Heat Transfer Coefficient and Radiation Equilibrium Vs. Cold Wall Heat Flux.

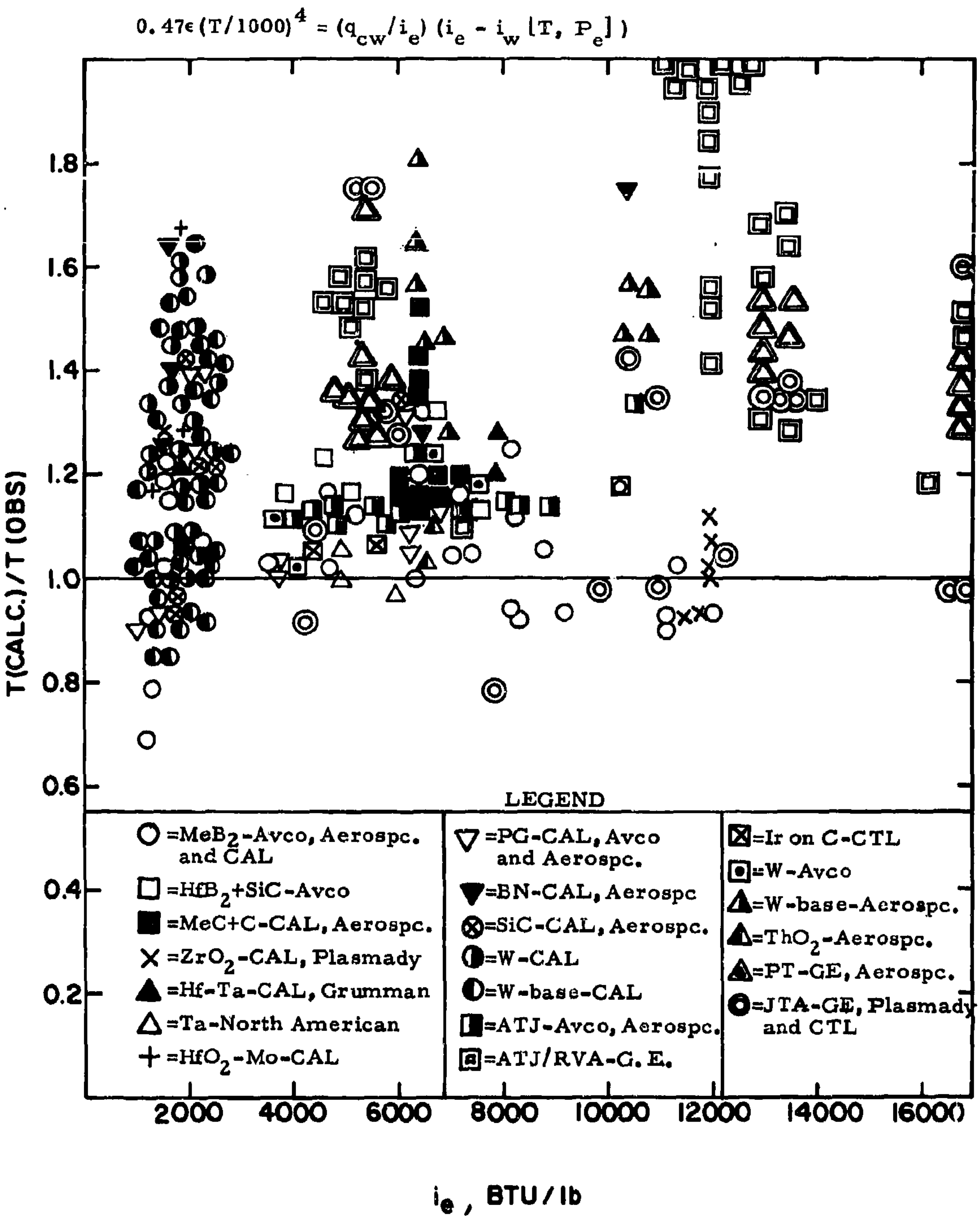

Figure 17. Ratio of Calculated to Observed Surface Temperatures Based on the Cold Wall Heat Transfer Coefficient and Radiation Equilibrium Vs. Stagnation Enthalpy.

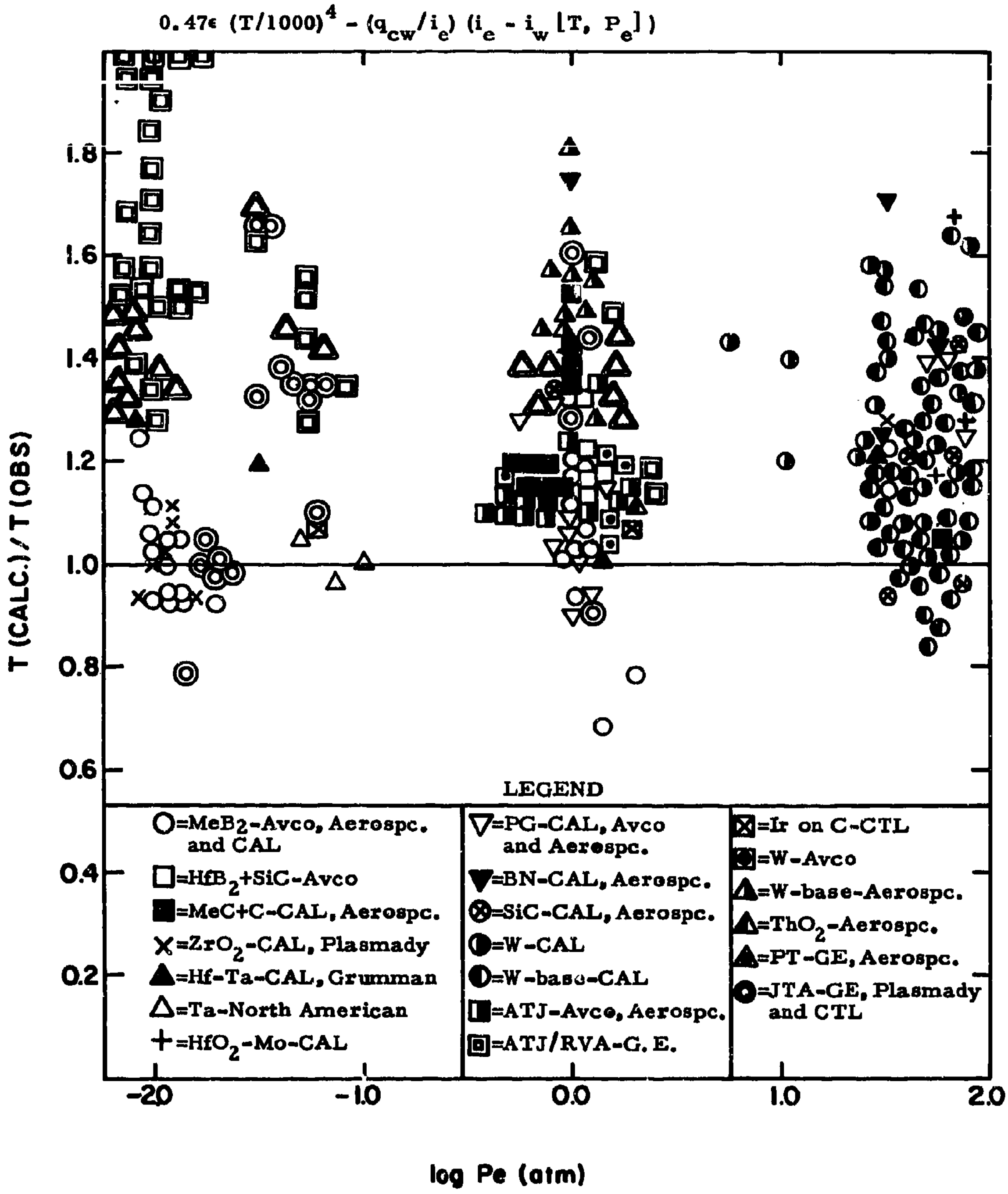

Figure 18. Ratio of Calculated to Observed Surface Temperatures Based on the Cold Wall Heat Transfer Coefficient and Radiation Equilibrium Vs. Stagnation Pressure.

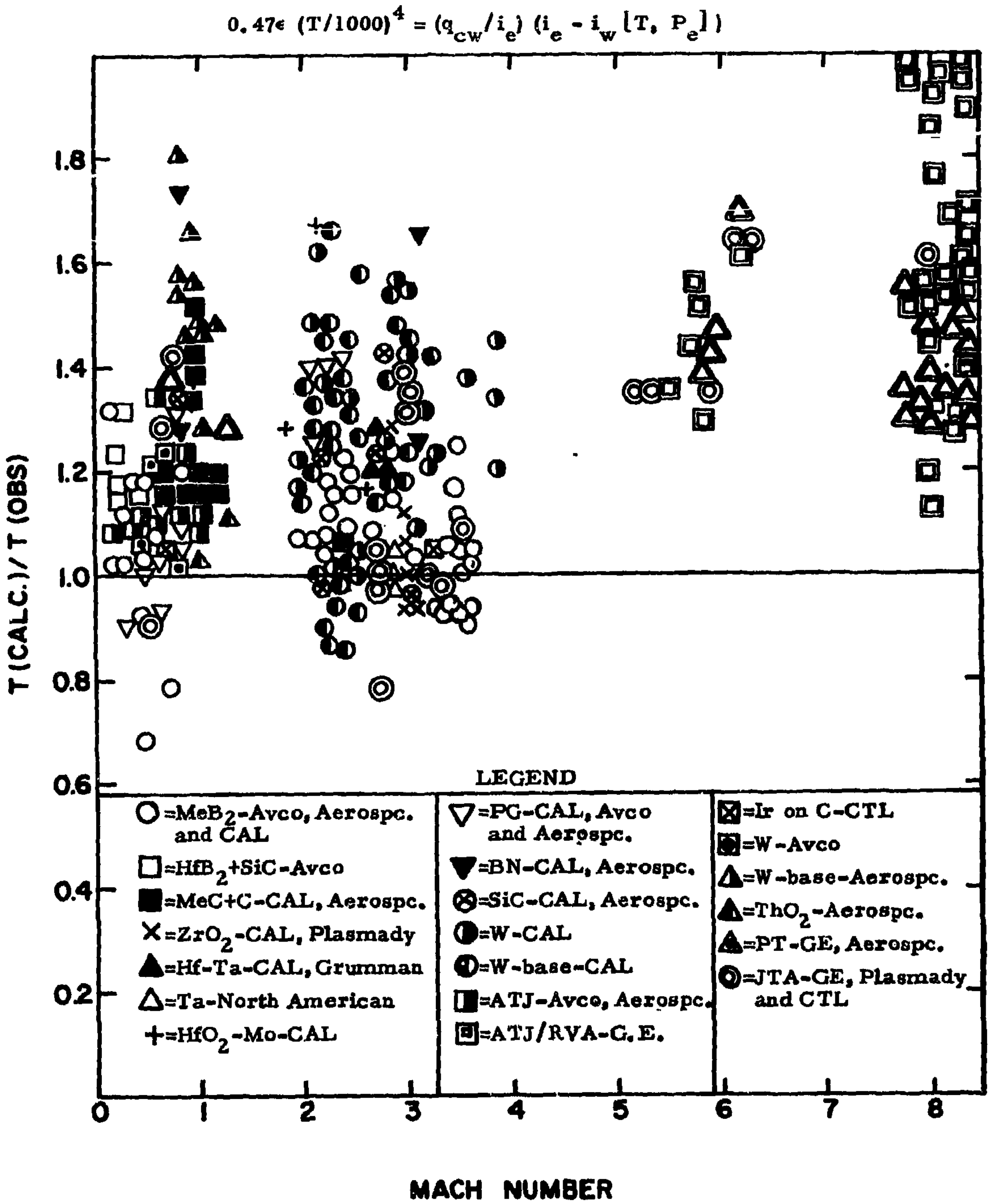

Figure 19. Ratio of Calculated to Observed Surface Temperatures Based on the Cold Wall Heat Transfer Coefficient and Radiation Equilibrium Vs. Mach Number.

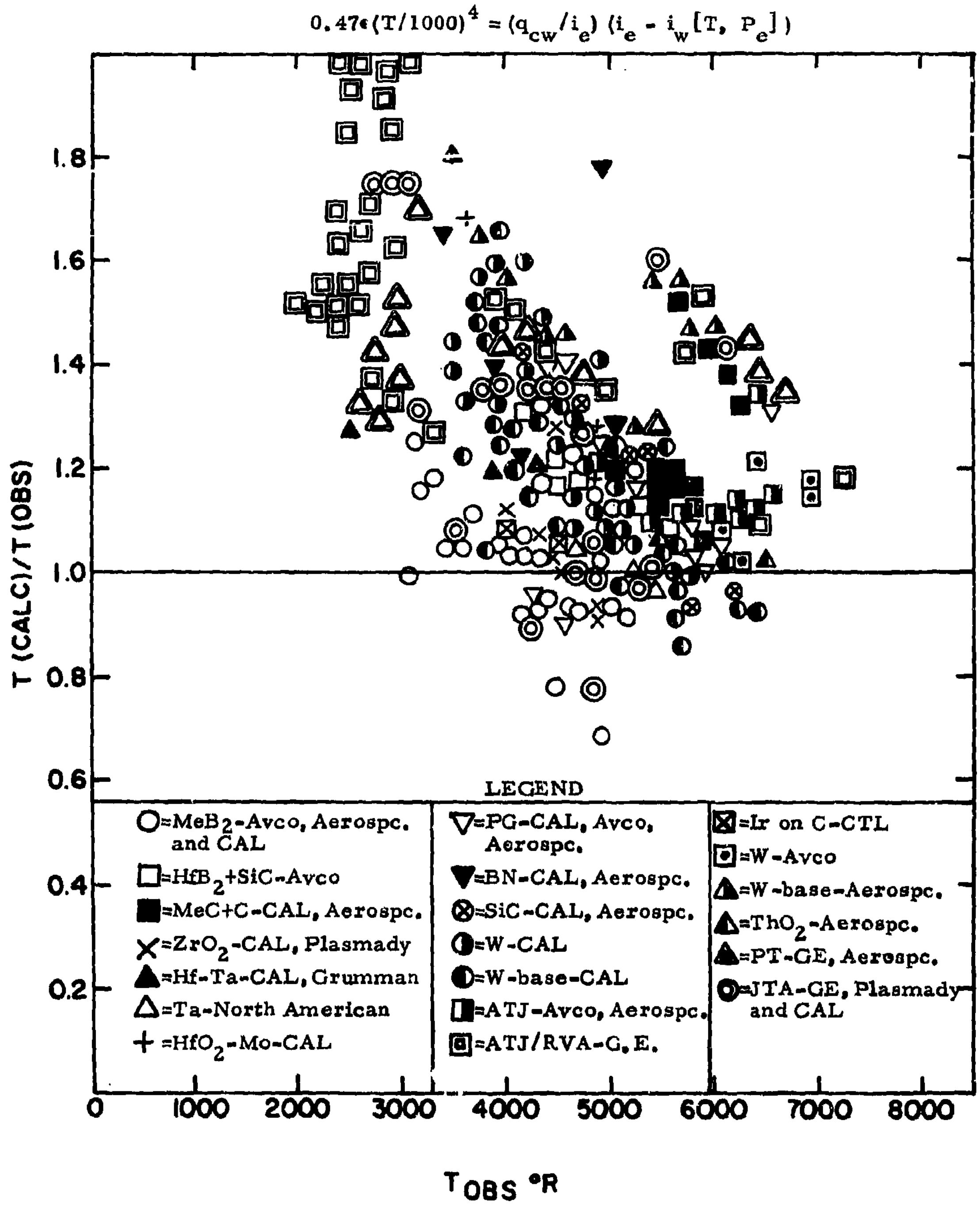

Figure 20. Ratio of Calculated to Observed Surface Temperatures Based on the Cold Wall Heat Transfer Coefficient and Radiation Equilibrium Vs. Observed Temperature.

$$0.47\epsilon (T/1000)^4 = 0.0386 (1 + 0.17 M^{-1})^{-1} (nP_e/D)^{1/2} (i_e - i_w [T, P_e])$$

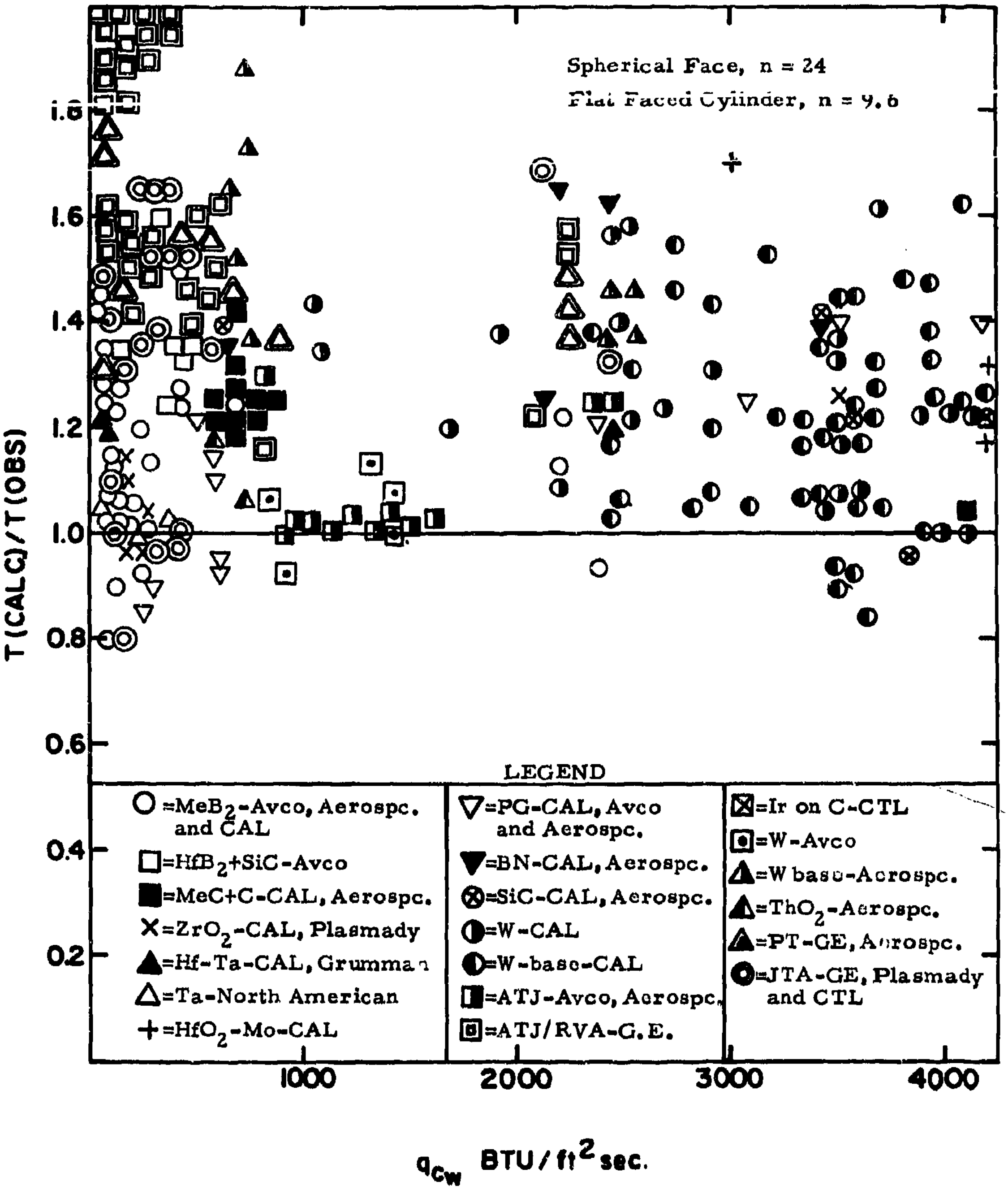

Figure 21. Ratio of Calculated to Observed Surface Temperatures Based on the Fay-Riddell Heat Transfer Coefficient and Radiation Equilibrium Vs. Cold Wall Heat Flux.

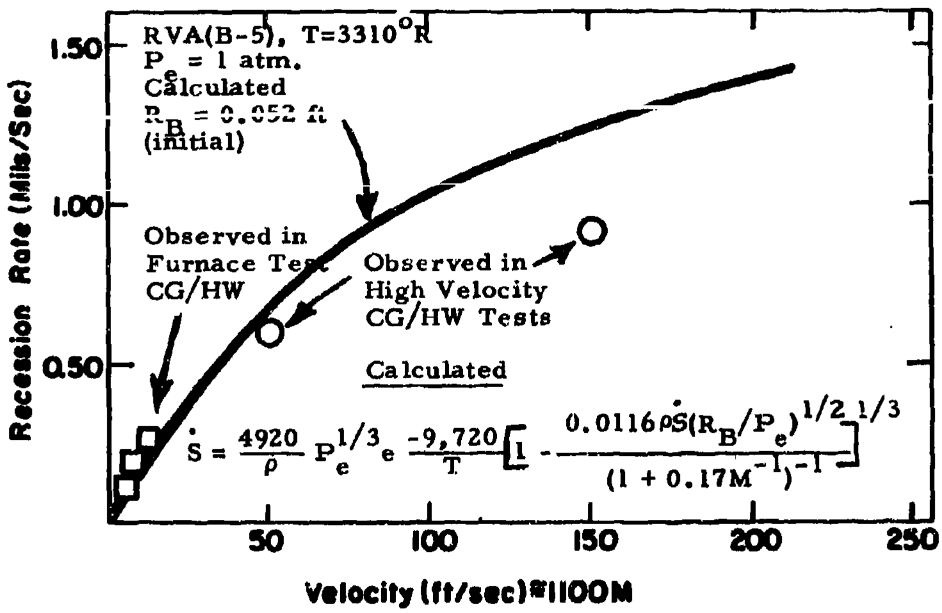

Figure 22. Comparison of Observed and Calculated Recession Rates for RVA(B-5) Graphite Cylinders at 3310°R

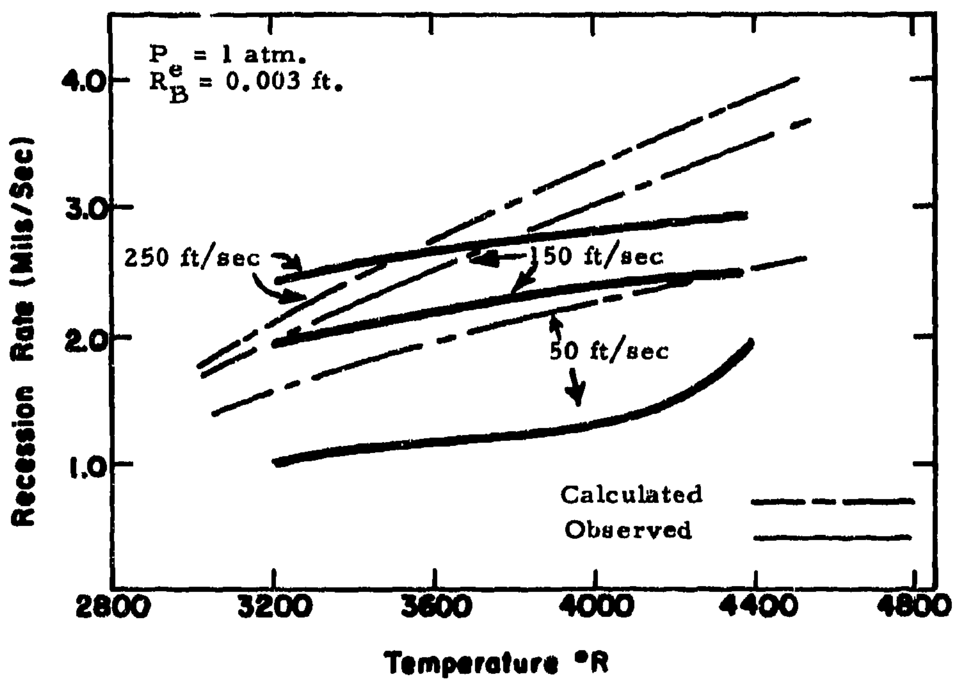

Figure 23. Comparison of Observed and Calculated Recession Rates for Graphite Cones, as a Function of Temperature and Air Velocity

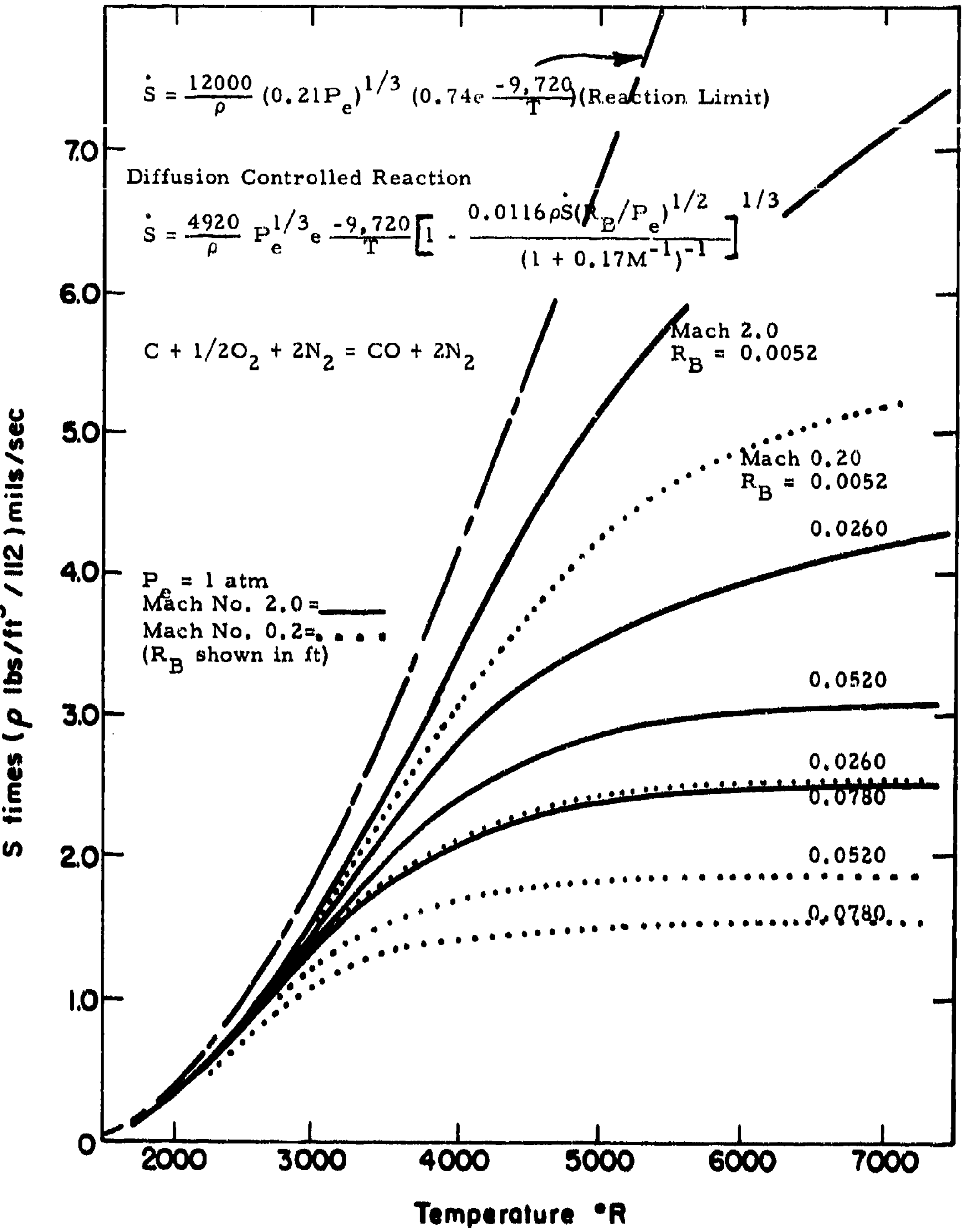

Figure 24. Calculated Effects of Mach Number and Body Radius on the Oxidation of Graphite at P_e = 1 atm.

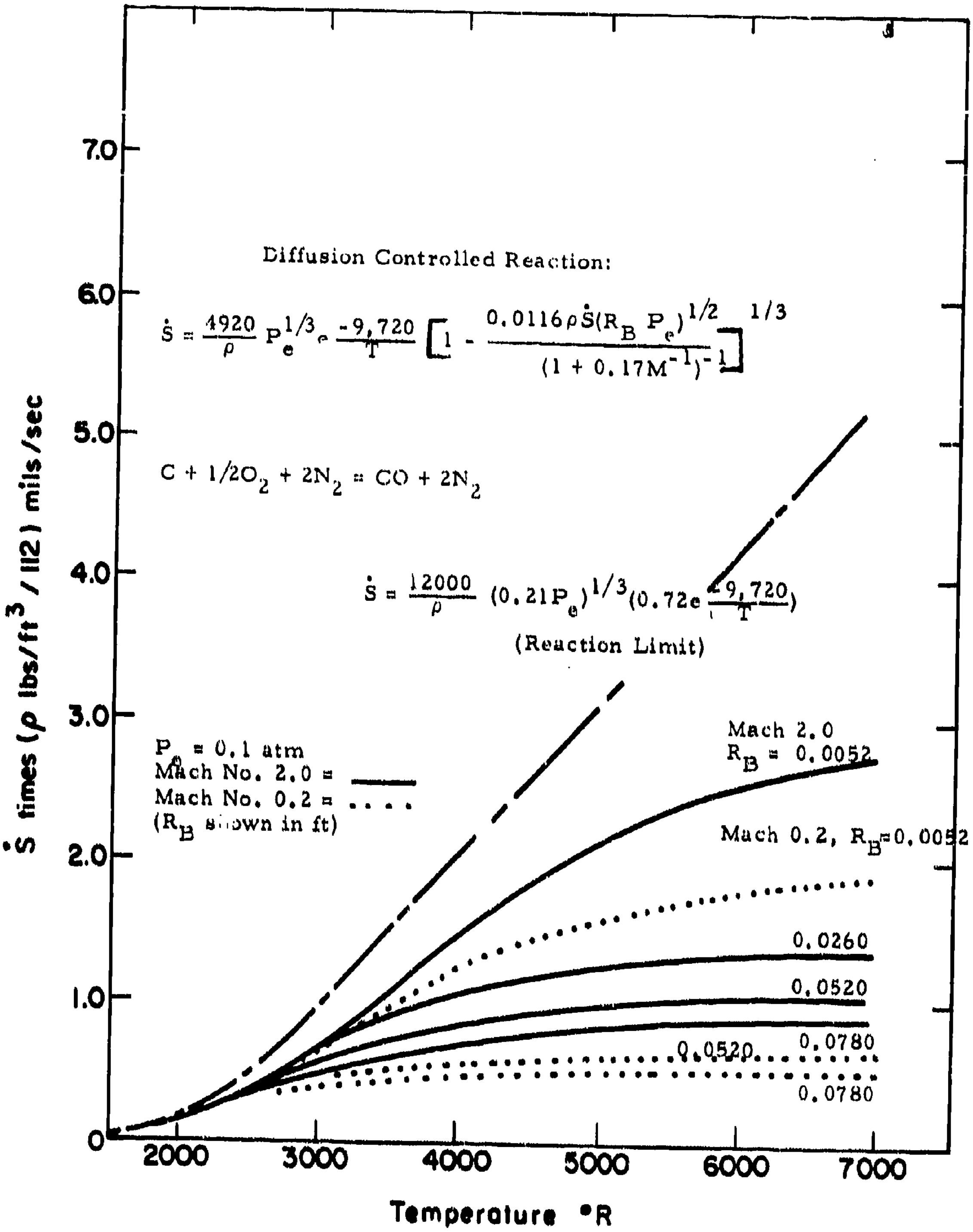

Figure 25. Calculated Effects of Mach Number and Body Radius on the Oxidation of Graphite at P_e = 0.1 atm.

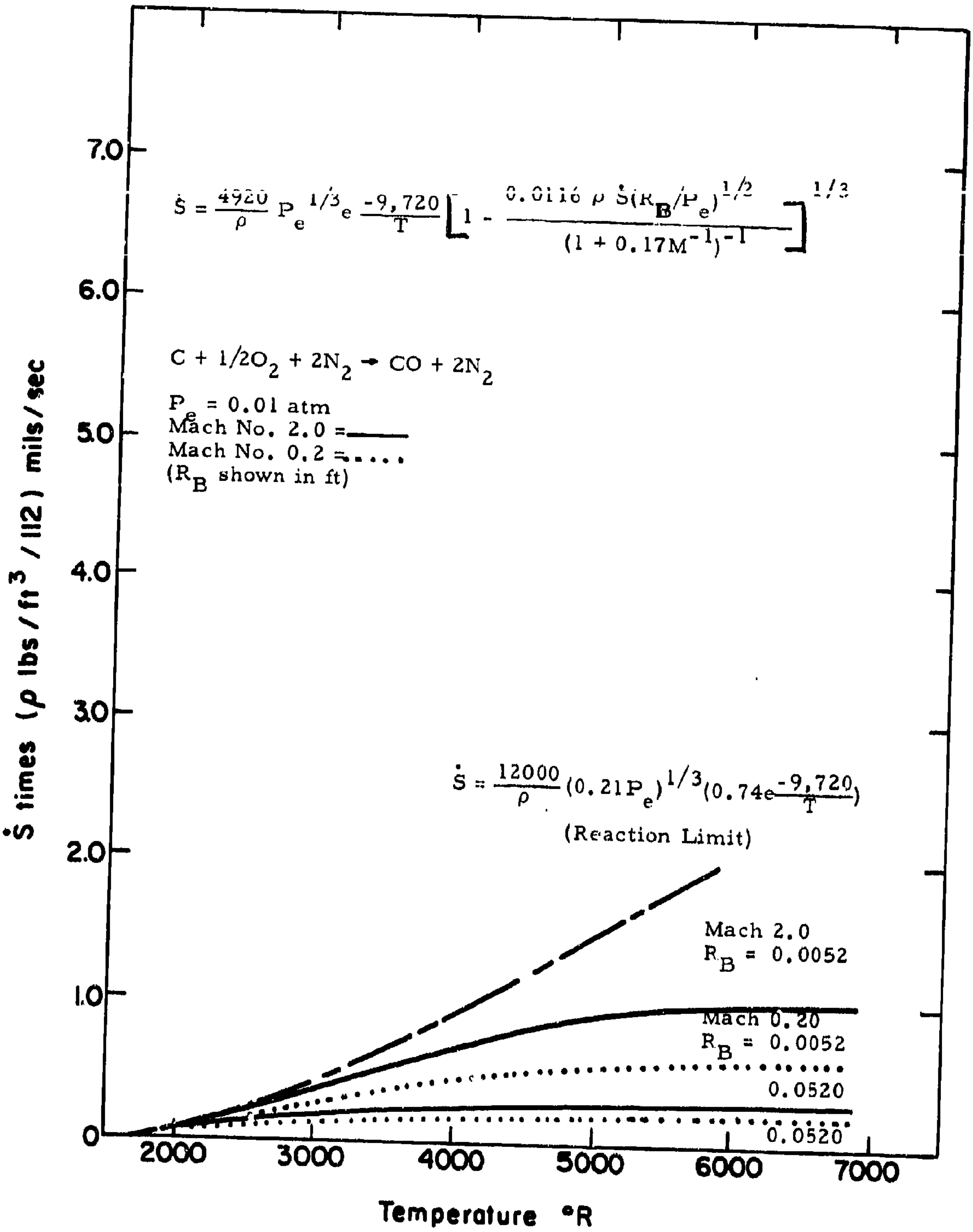

Figure 26. Calculated Effects of Mach Number and Body Radius on the Oxidation of Graphite at P_e = 0.001 atm.

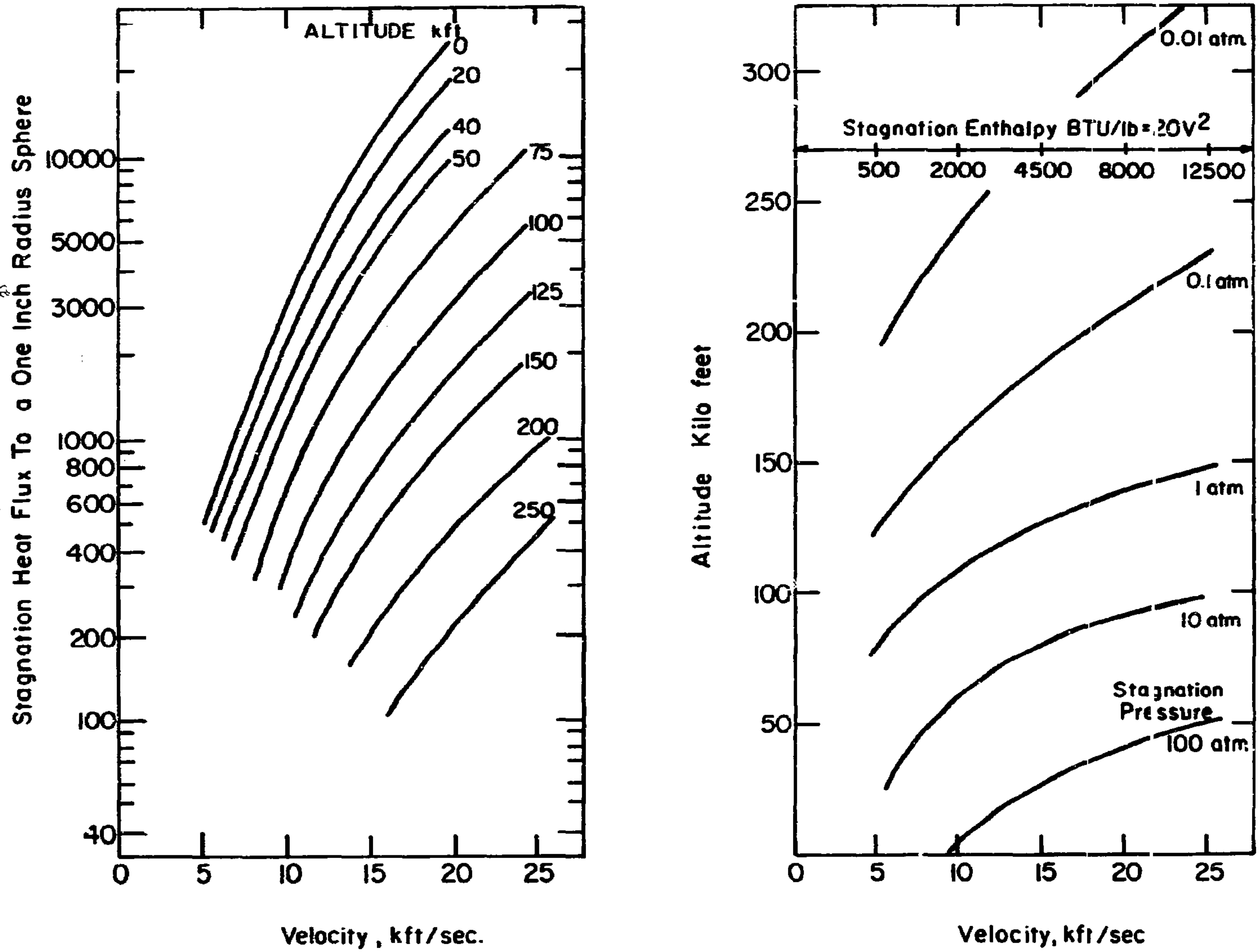

Figure 27. (Altitude/Velocity) Vs. Stagnation (Enthalpy/Flux) Relations for a One Inch Sphere (39-41).

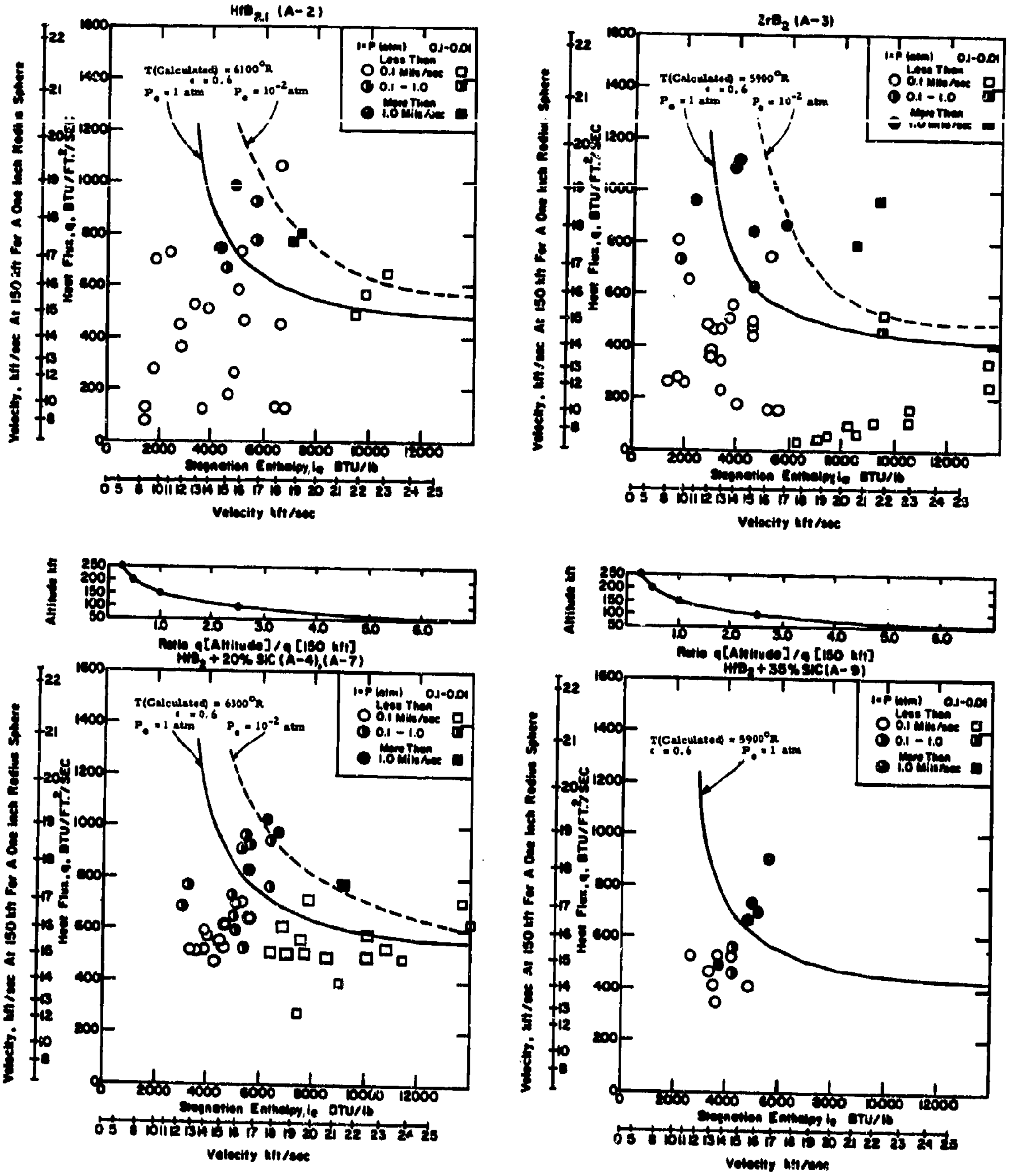

Figure 28. Recession Rates of $HfB_{2.1}$ (A-2), ZrB_2(A-3), HfB_2+ 20%SiC(A-4)(A-7) and HfB_2 + 35%SiC(A-9) as a Function of Heat Flux and Stagnation Enthalpy.

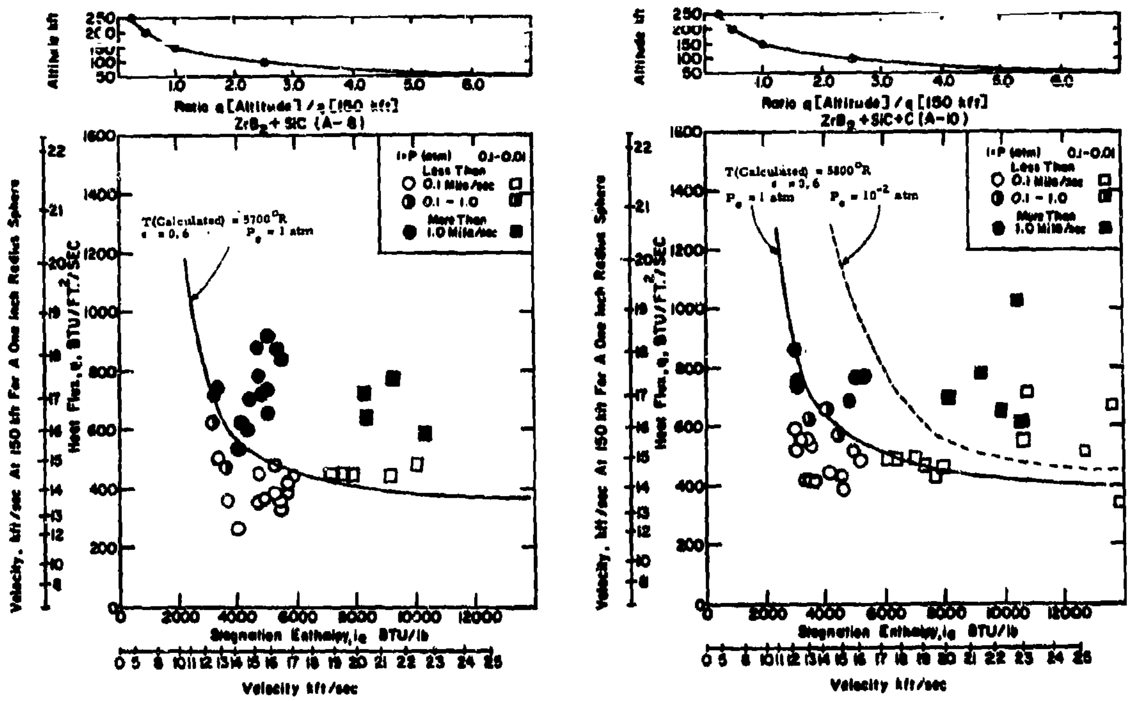

Figure 29. Recession Rates of ZrB_2+20%SiC(A-8) and ZrB_2+14%SiC+30%C (A-10) as a Function of Heat Flux and Stagnation Enthalpy.

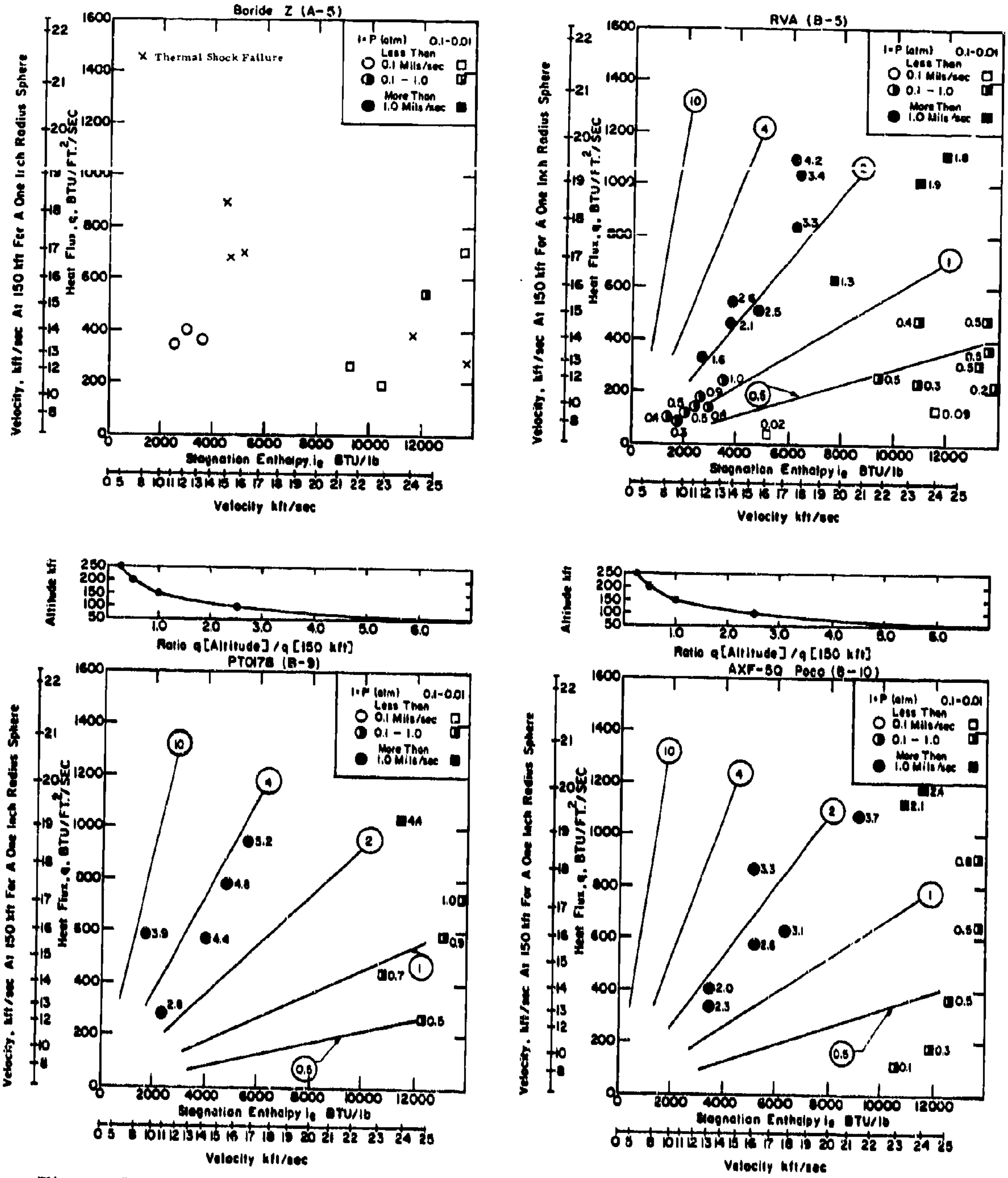

Figure 30. Recession Rates of Boride Z(A-5), RVA(B-5), PT0178(B-9) and POCO(B-10) as a Function of Heat Flux and Stagnation Enthalpy. Lines Indicate Theoretical Recession Rates Calculated from the Equation $\dot{S} = q/1.17V^2$. Numbers on Points Show Measured Recession Rates.

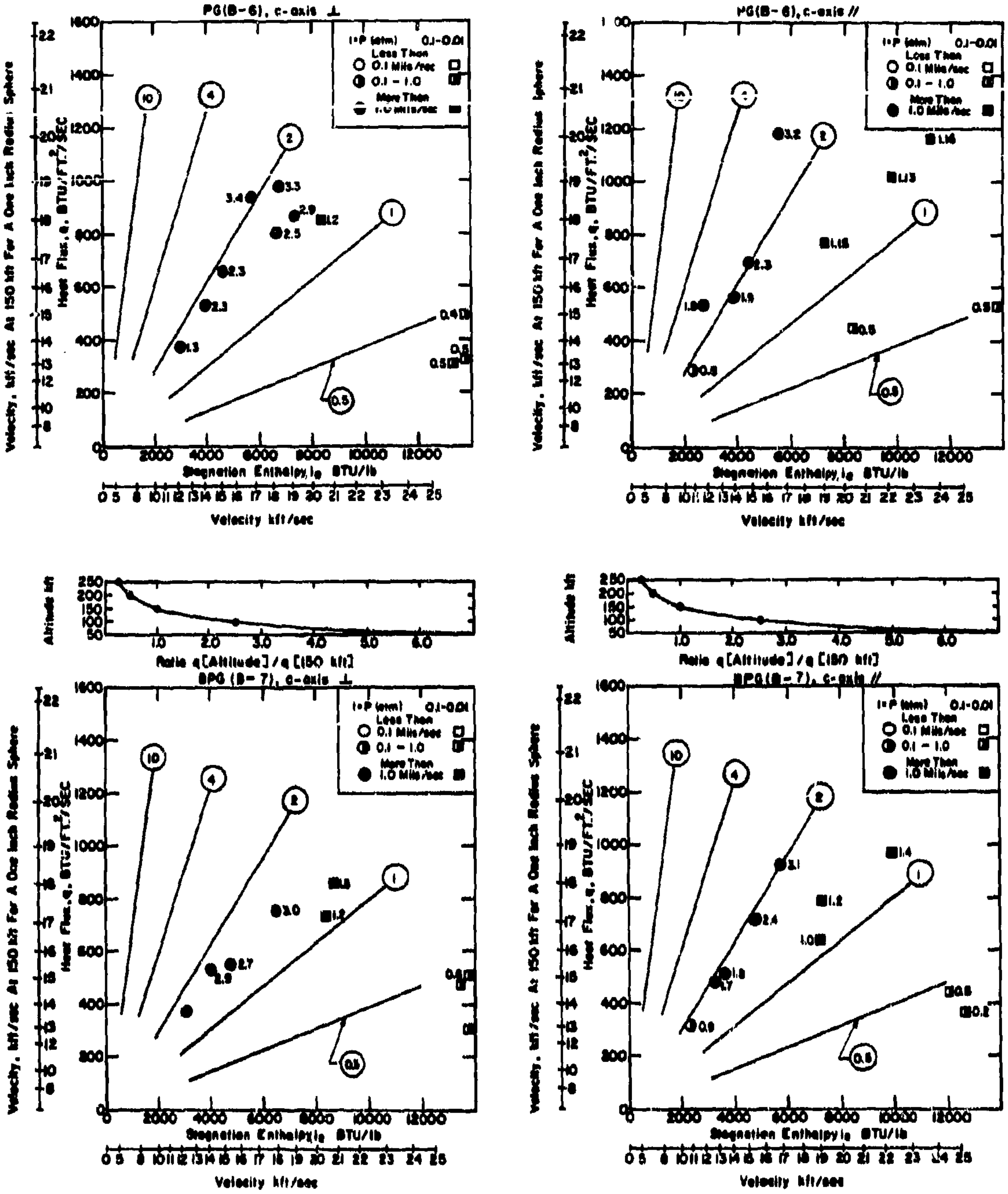

Figure 31. Recession Rates of PG(B-6) and BPG(B-7) as a Function of Heat Flux and Stagnation Enthalpy. Lines Indicate Theoretical Recession Rates Calculated From the Equation $S = q/1.17V^2$. Numbers on Points Show Measured Recession Rates.

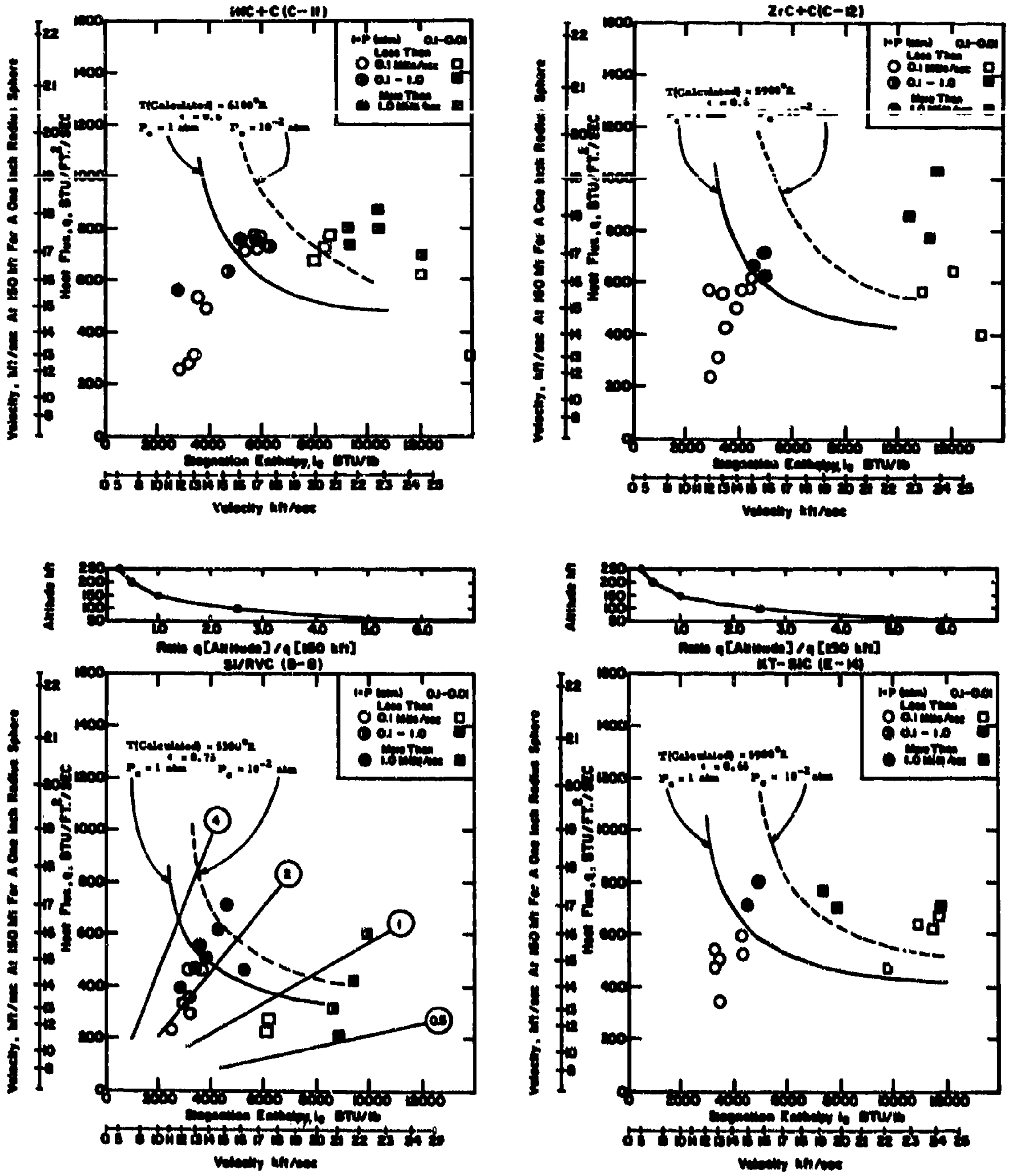

Figure 32. Recession Rates of HfC+C(C-11), ZrC+C(C-12), Si/RVC(B-8) and KT-SiC(E-14) as a Function of Heat Flux and Stagnation Enthalpy. Lines on (B-8) Plot Indicate Theoretical Graphite Recession Rates Calculated From the Equation $S = q/1.17V^2$.

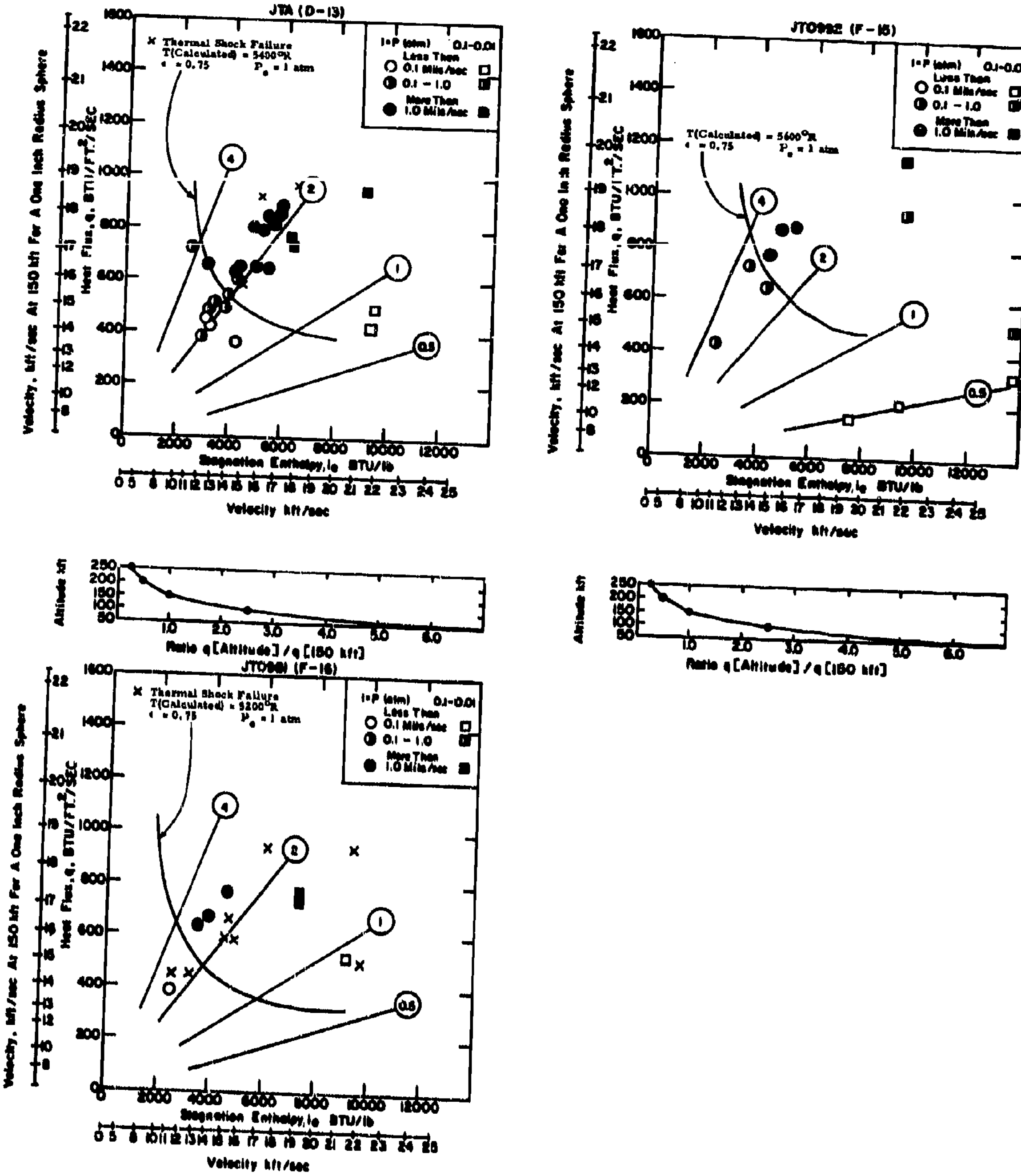

Figure 33.. Recession Rates of JTA(D-13), JT0992(F-15), and JT0981(F-16) as a Function of Heat Flux and Stagnation Enthalpy. Lines Indicate Theoretical Graphite Recession Rates Calculated From the Equation $\dot{S} = q/1.17V^2$.

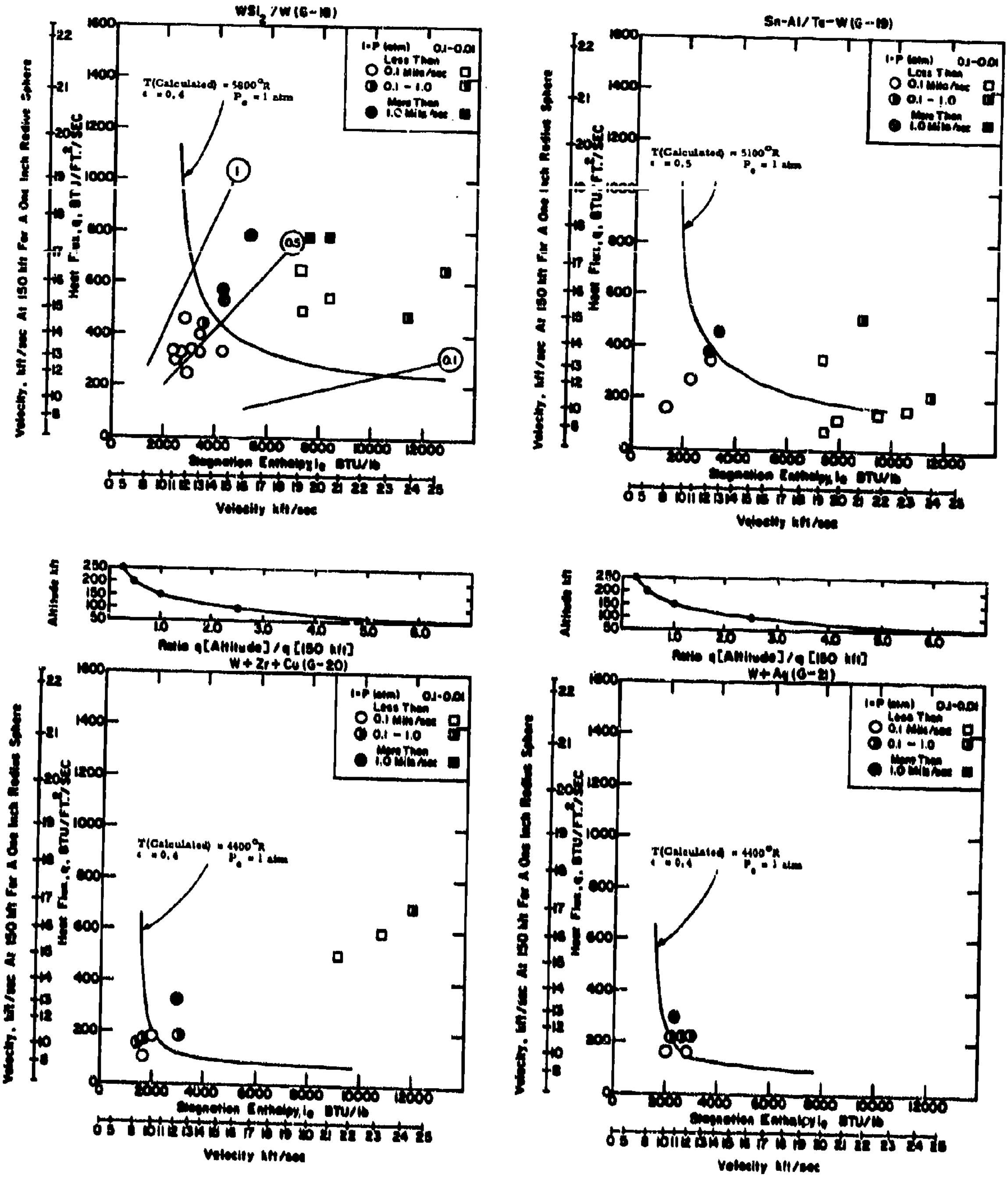

Figure 34. Recession Rates of WSi_2/W(G-18), Sn-Al/Ta-W(G-19), W+Zr+Cu (G-20) and W + Ag(G-21) as a Function of Heat Flux and Stagnation Enthalpy. Lines on (G-18) Plot Indicate Theoretical Tungsten Recession Rates.

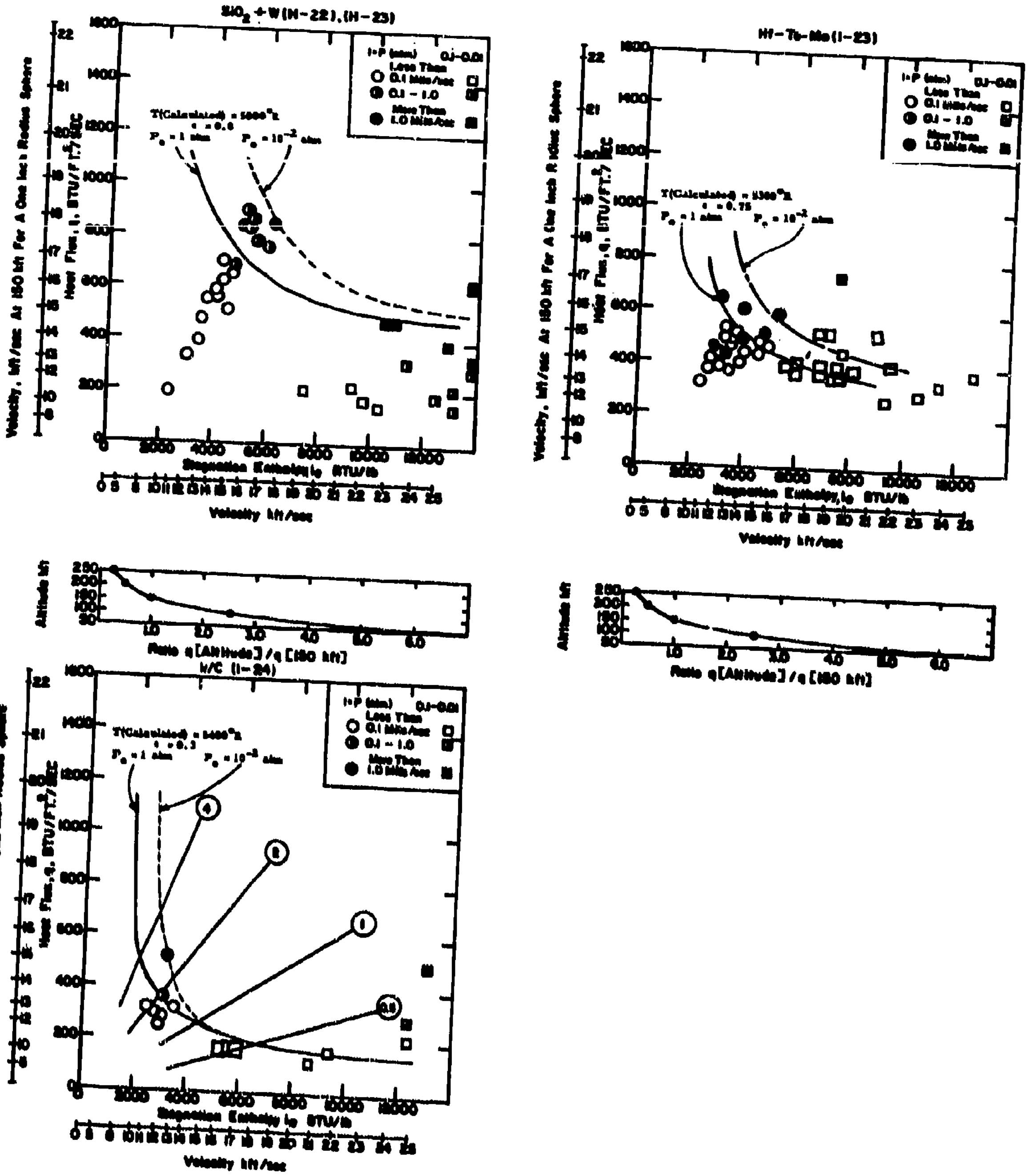

Figure 35. Recession Rates of SiO_2 + W(H-22)(H-23), Hf-Ta-Mo(I-23) and Ir/C(I-24) as a Function of Heat Flux and Stagnation Enthalpy. Lines on (I-24) Plot Indicate Theoretical Graphite Recession Rates.

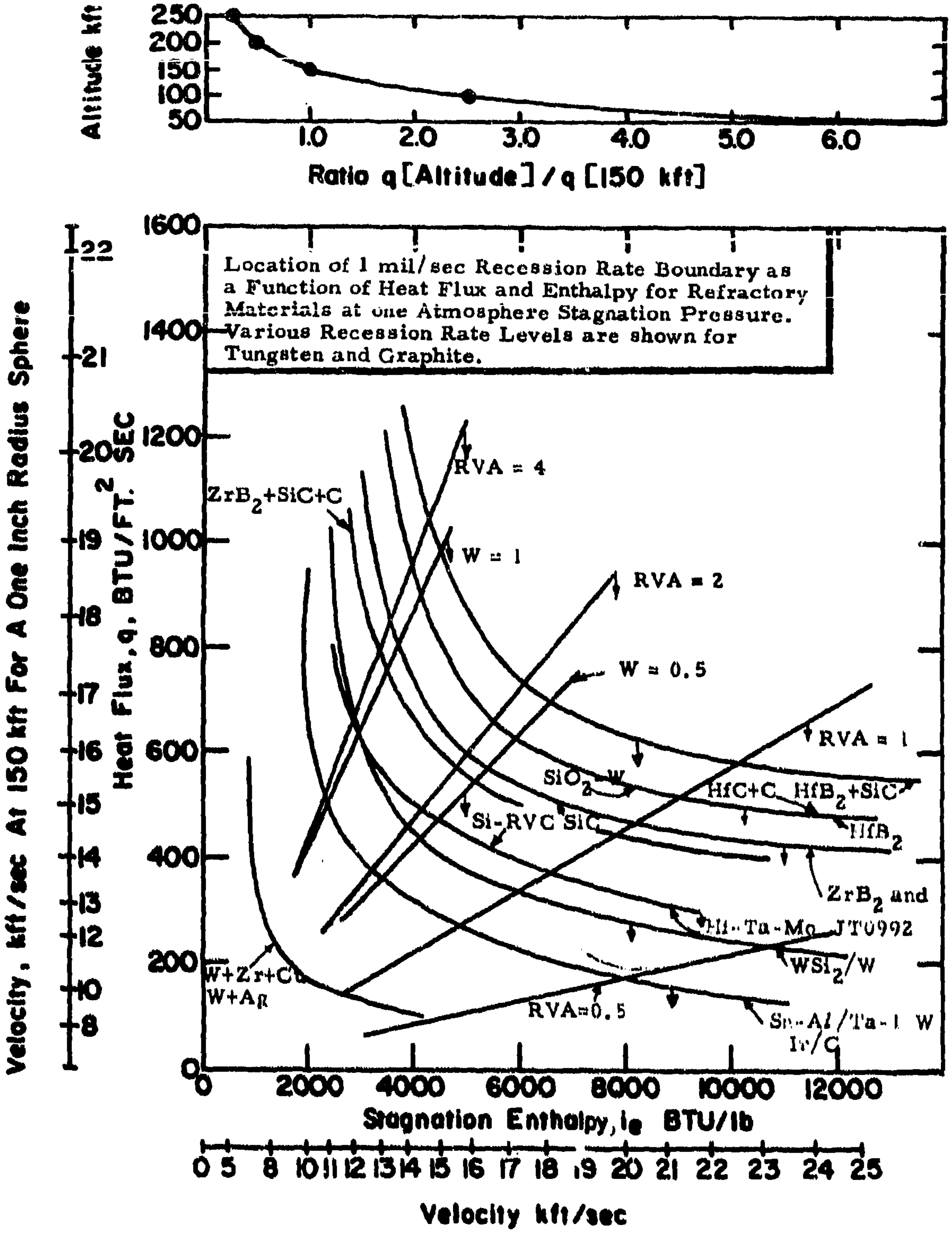

Figure 36. Location of 1 mil/sec Recession Rate Boundary as a Function of Heat Flux and Enthalpy for Refractory Materials at P_e = 1 atm. Various Recession Levels are Shown for RVA Graphite and Tungsten.

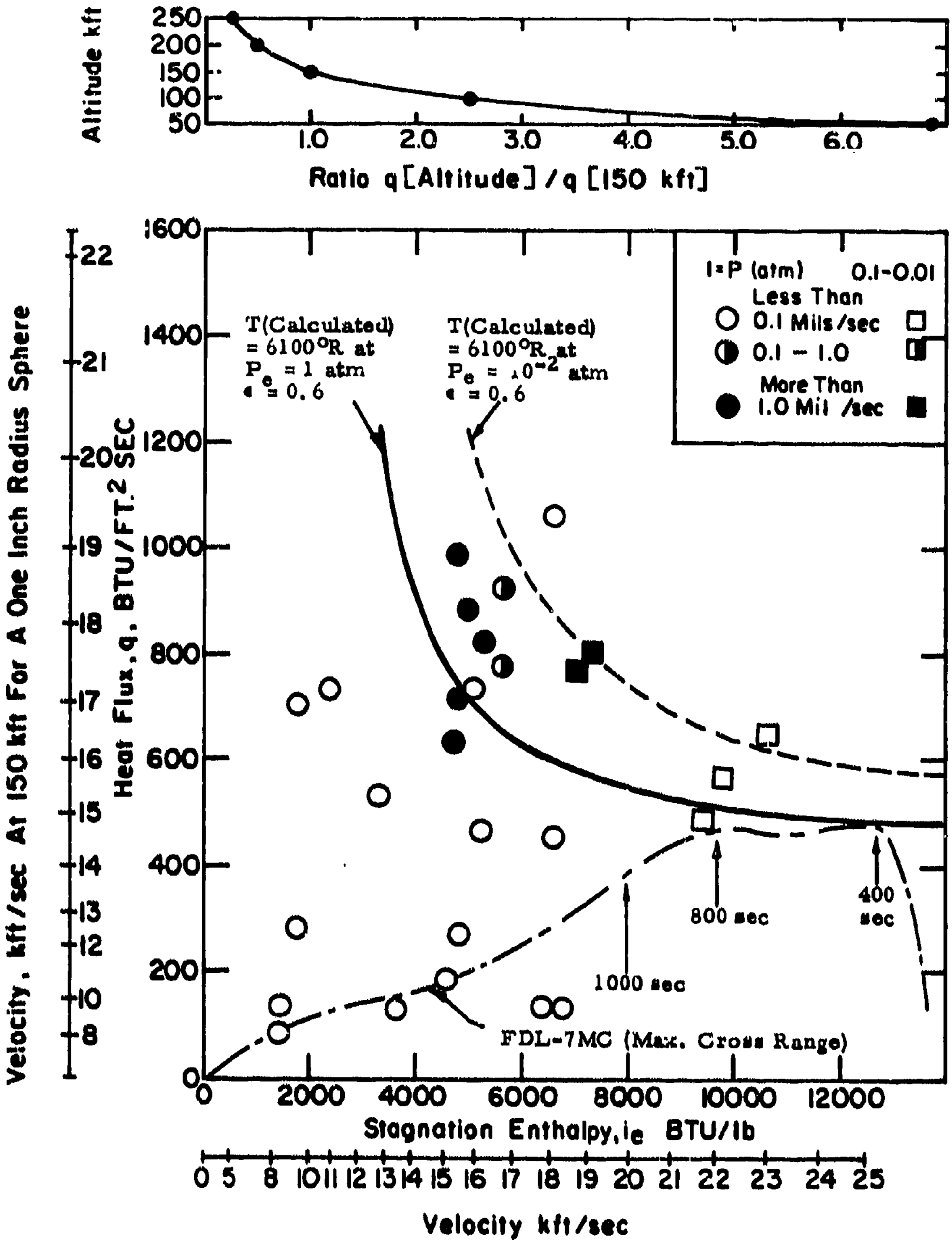

Figure 37. Recession Rate of Hafnium Diboride as a Function of Heat Flux and Stagnation Enthalpy. Compared with FDL-7MC-MCR Trajectory.

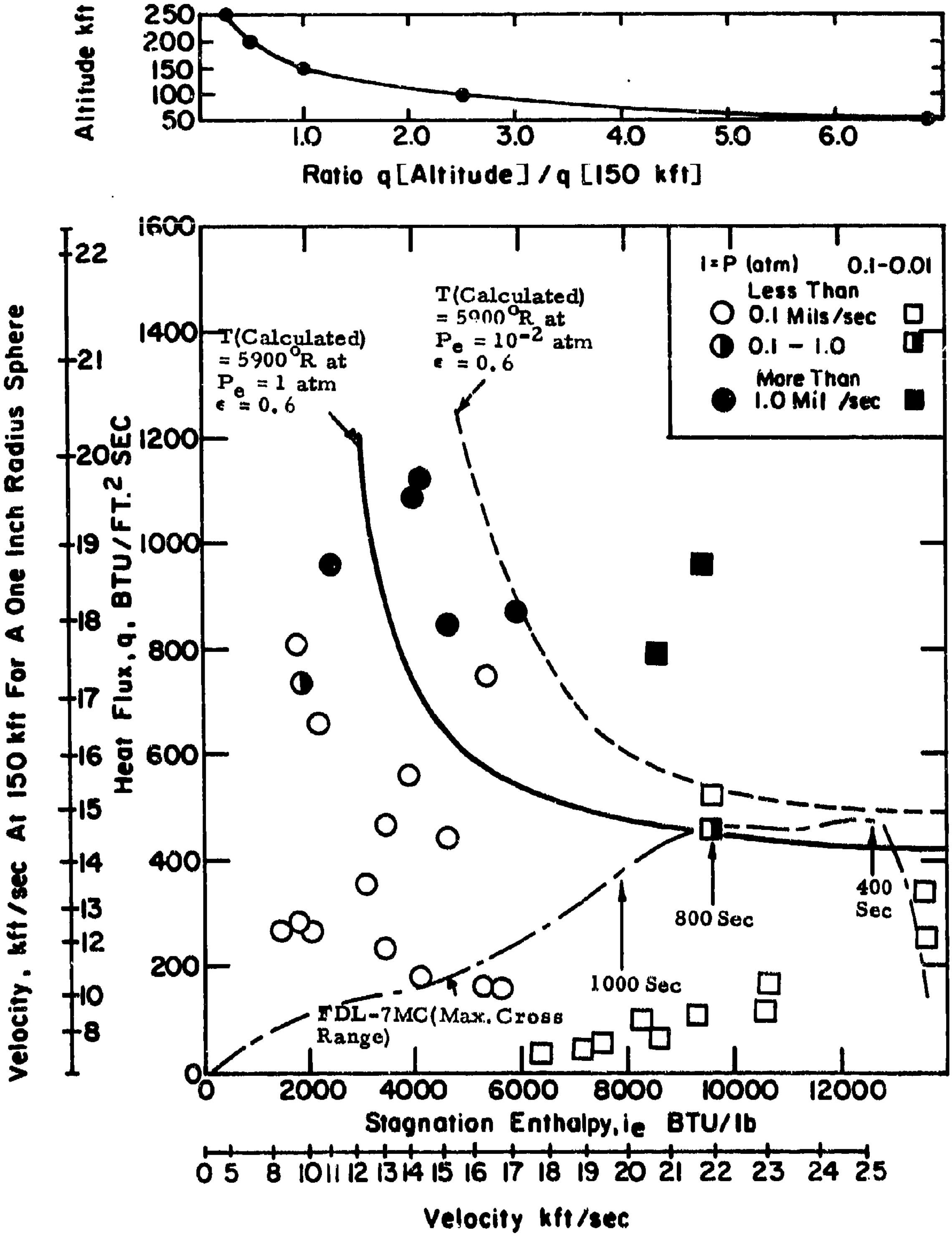

Figure 38. Recession Rate of Zirconium Diboride as a Function of Heat Flux and Stagnation Enthalpy. Compared with FDL-7MC-MCR Trajectories.

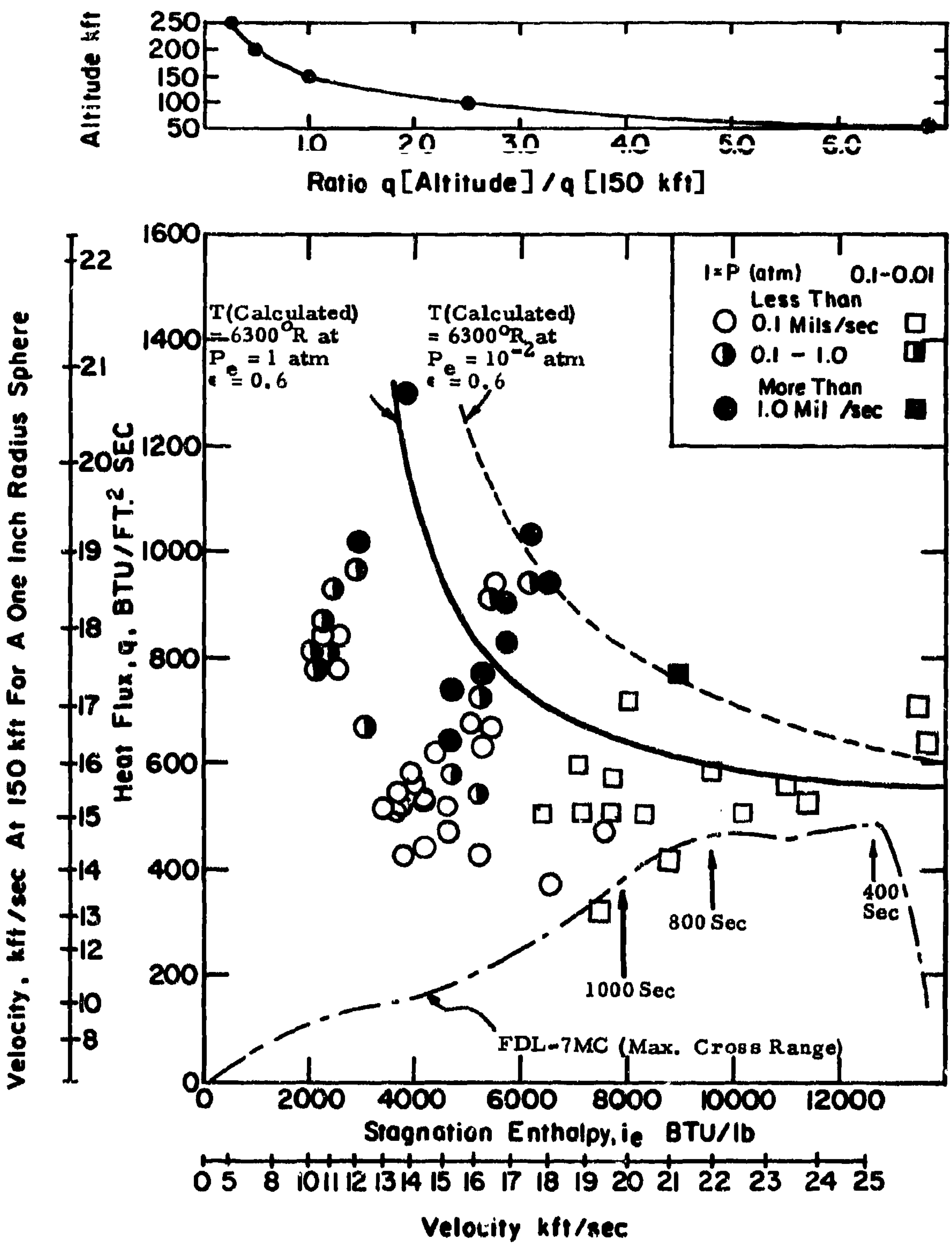

Figure 39. Recession Rate of HfB_2 + SiC Composites as a Function of Heat Flux and Stagnation Enthalpy. Compared with FDL-7MC-MCR Trajectory.

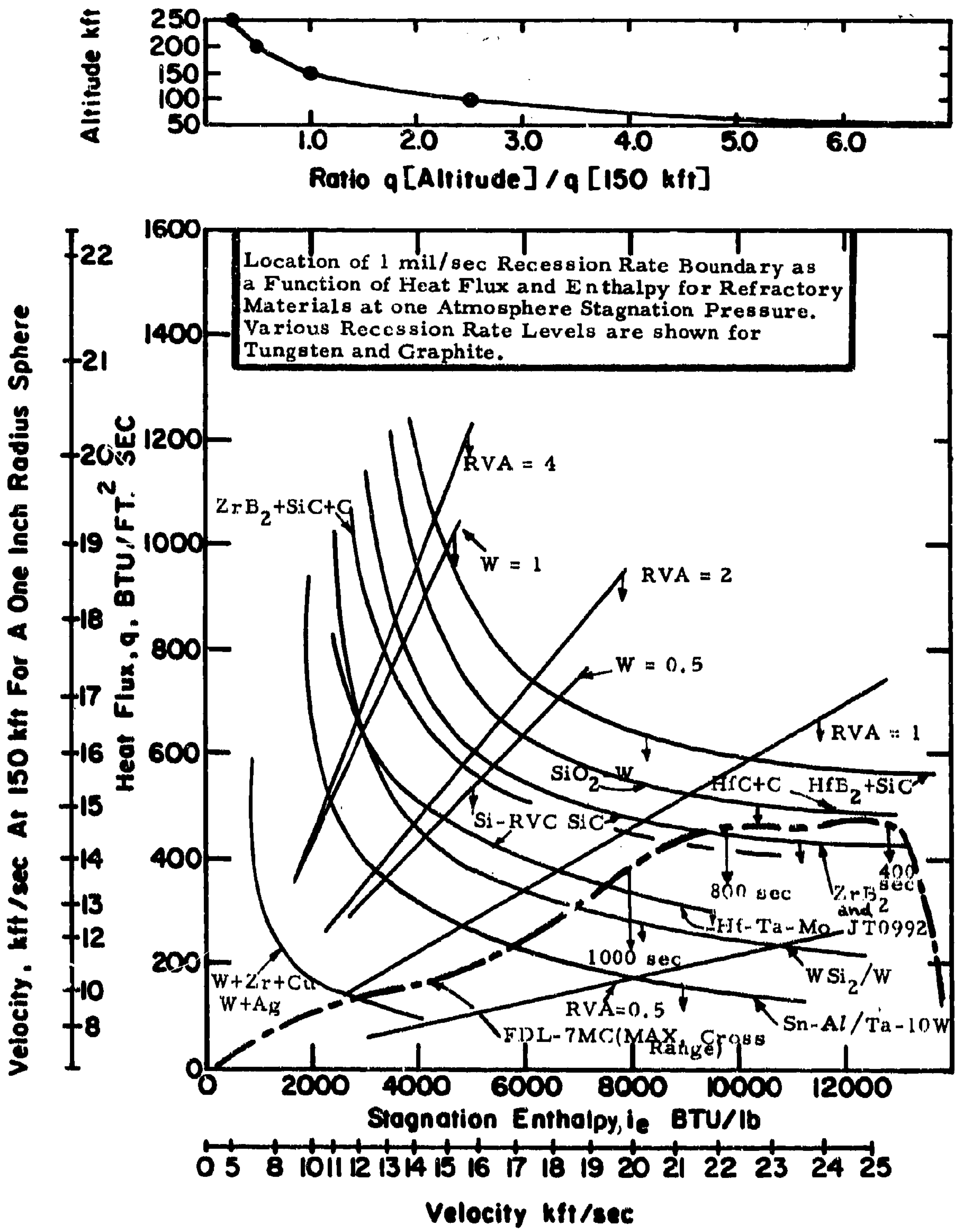

Figure 40. Superposition of the FDL-7MC Trajectory on the Flux-Enthalpy Map showing Recession Rates for Refractory Materials.

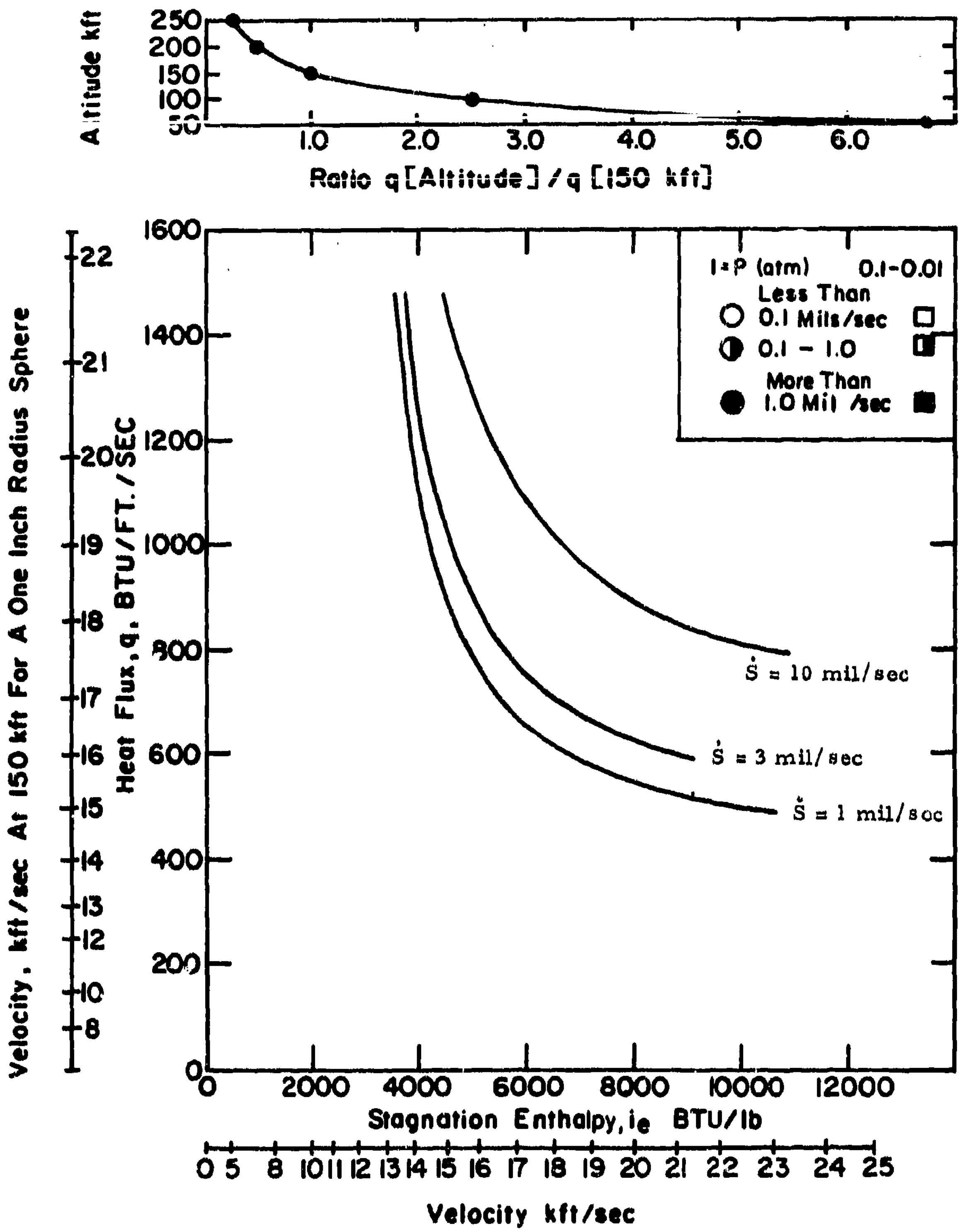

Figure 41. Computed Boundaries for Melting Recession of $HfB_{2.1}$ (A-2).

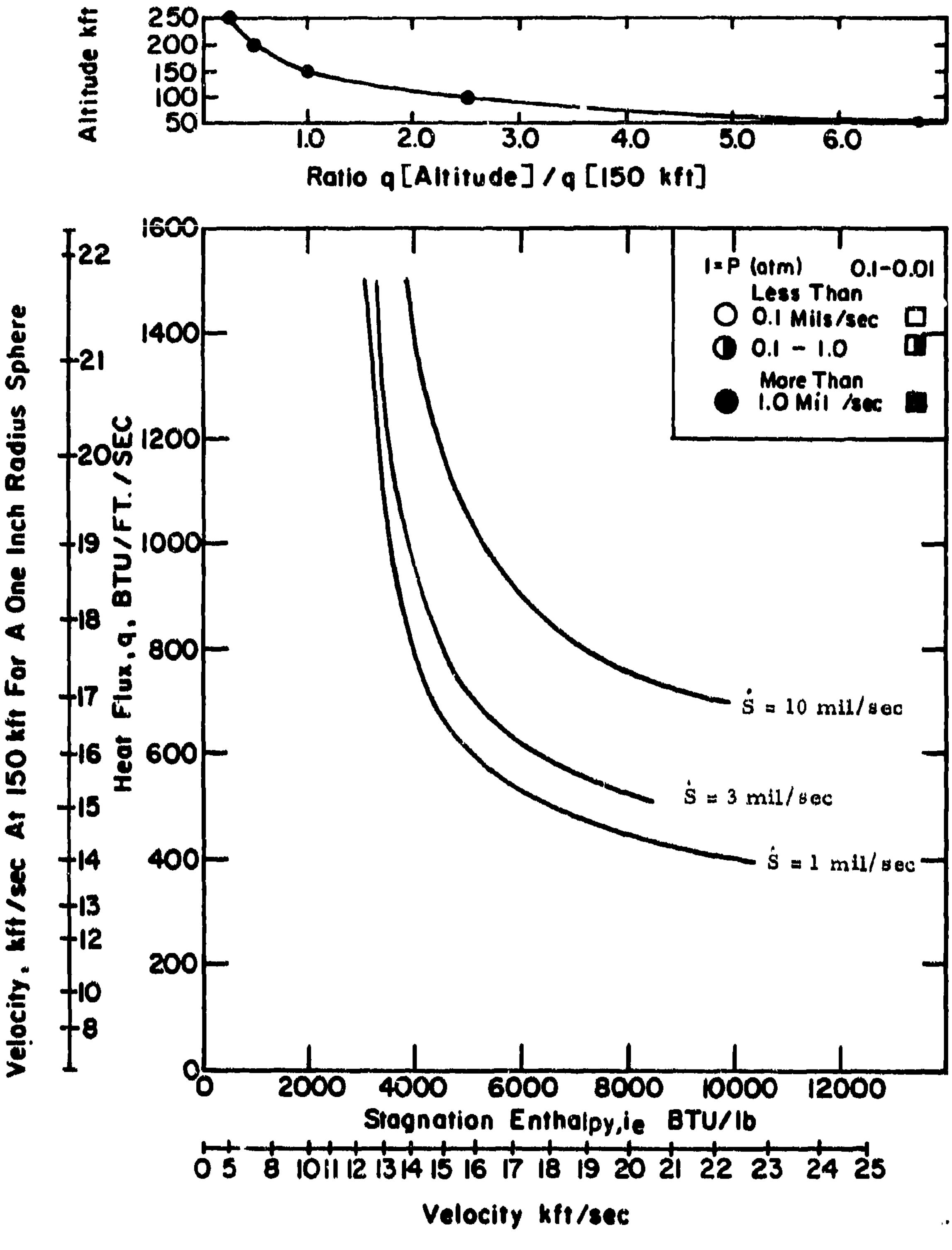

Figure 42. Computed Boundaries for Melting Recession of ZrB_2(A-3).

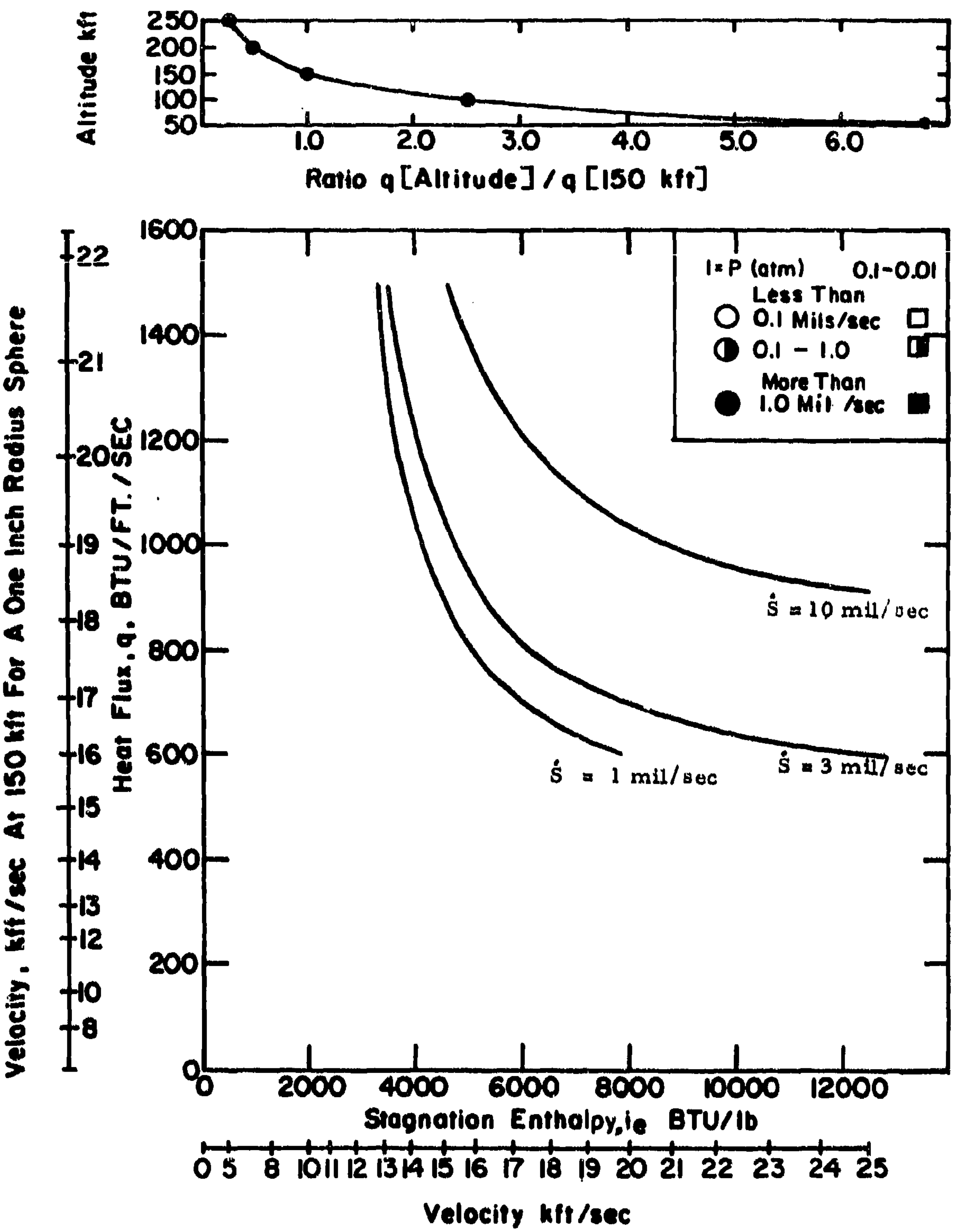

Figure 43; Computed Boundaries for Melting Recession of HfC+C (C-11).

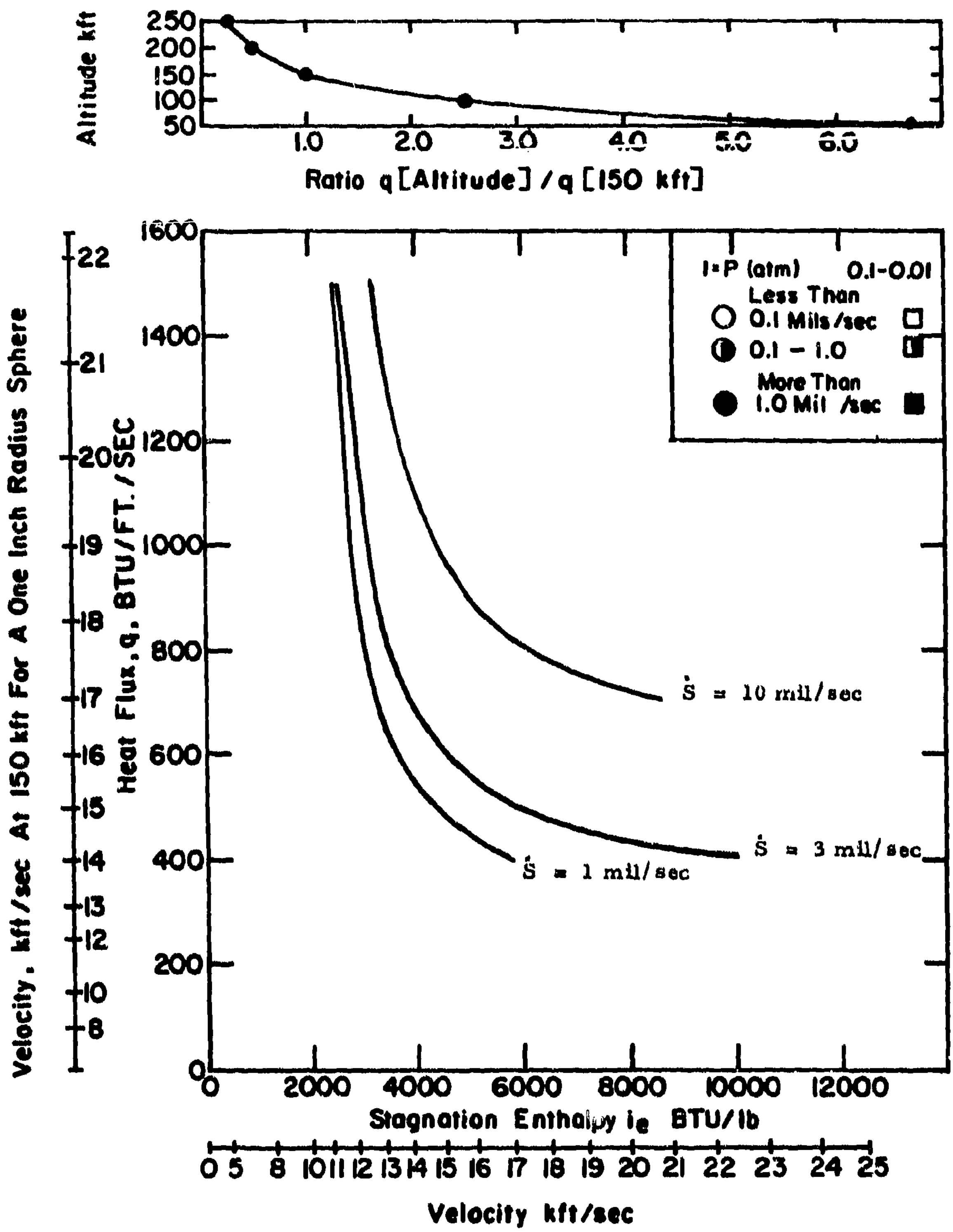

Figure 44. Computed Boundaries for Melting Recession of ZrC + C (C-12).

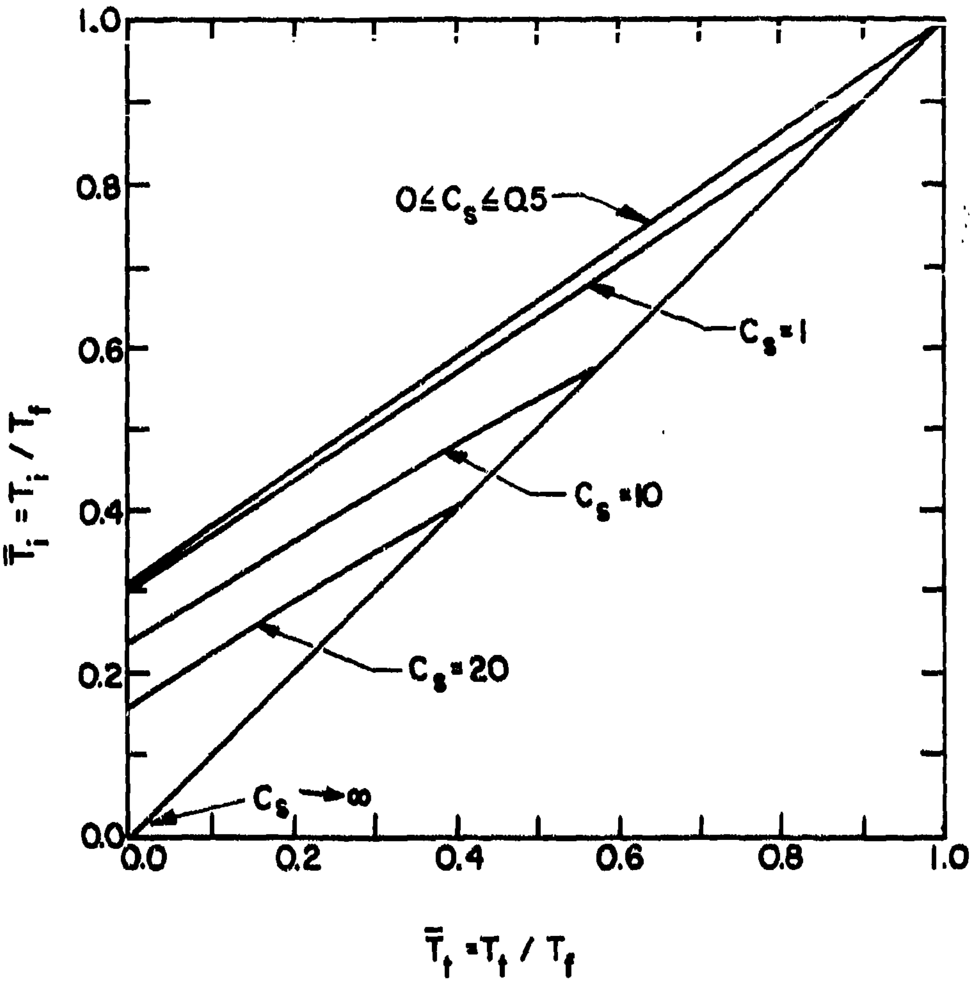

Figure 45. Variation of T_i with T_t for a Number of C_S Values According to Equation 64 when $I/L = 0$ and $k_F/k_S = 0.10$.

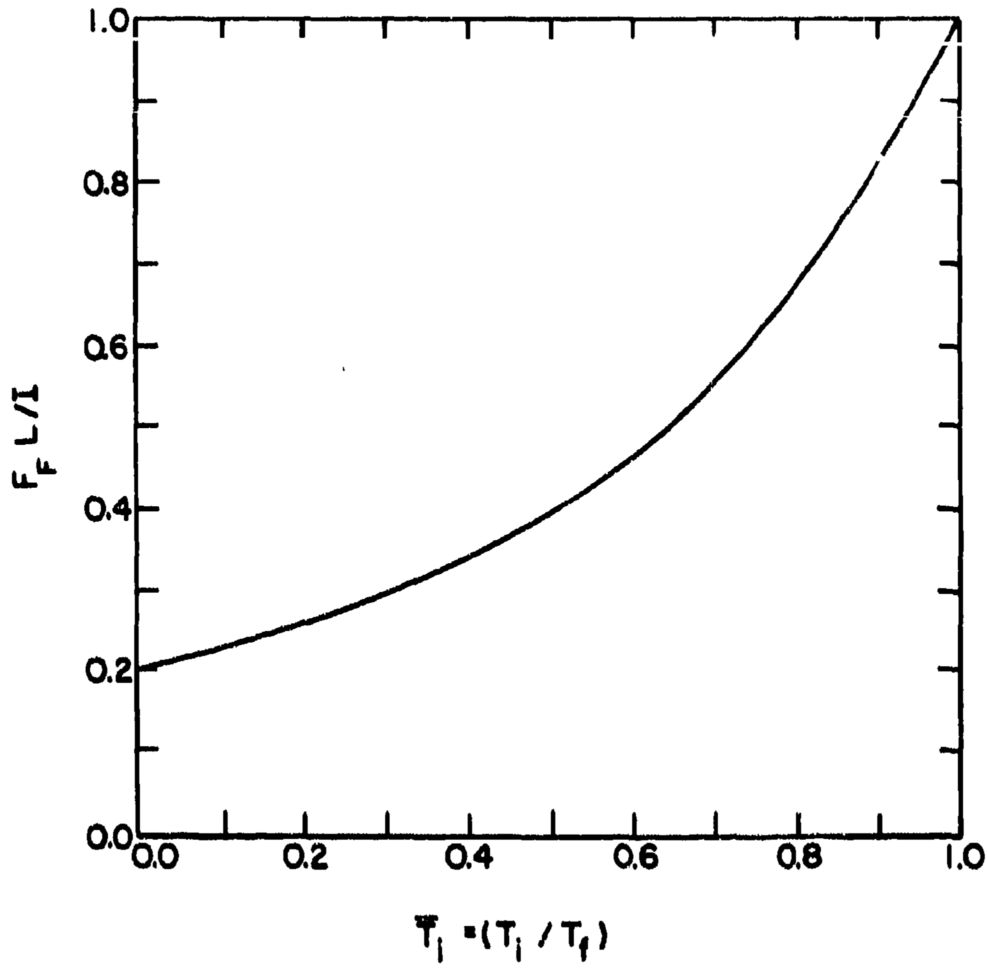

Figure 46. The Effect of Interface Temperature, $\bar{T}_i$, on the Level of the Radiation Contribution, F_F, According to Equation 66.

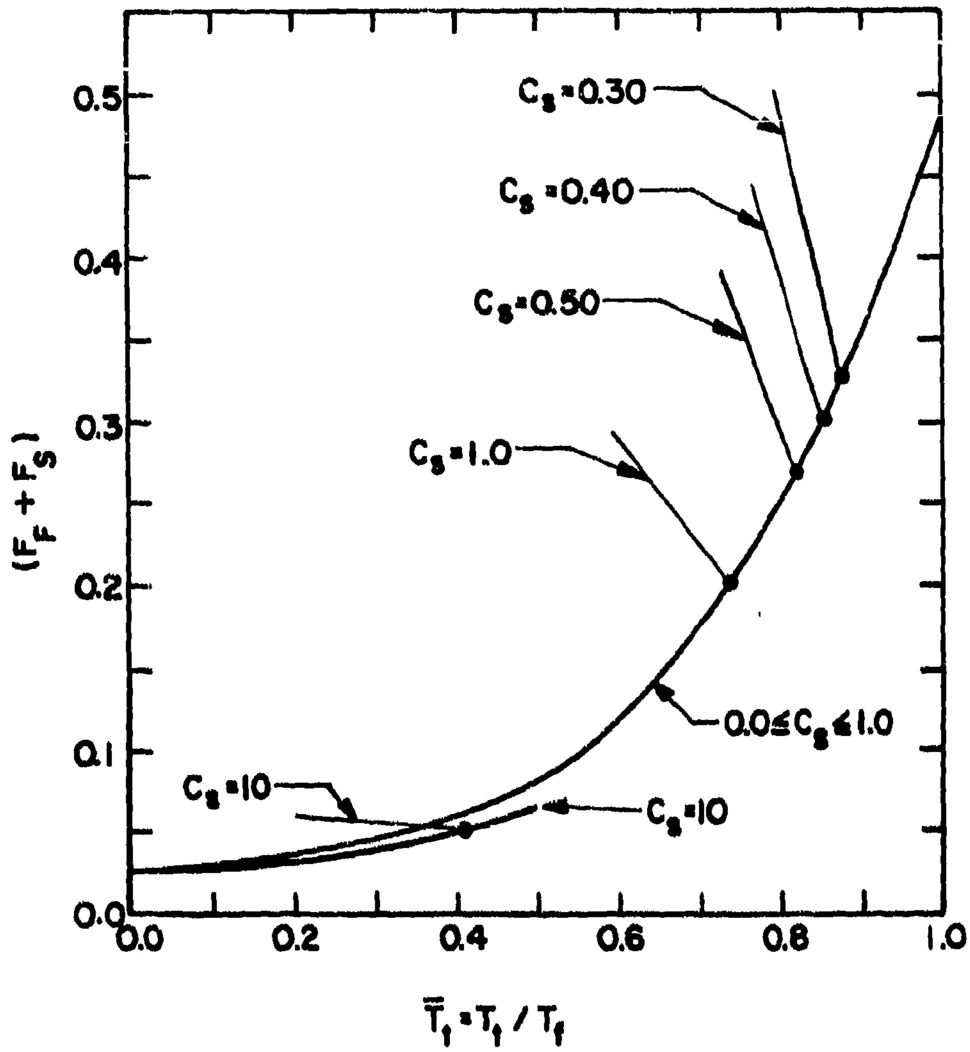

Figure 47. The Dependence of the Total Radiation Parameter (F_F+F_S) on $\bar{T}_t$ for various values of C_S when $I/L = 0.10$ and $k_F/k_S = 0.10$ derived from Equations 66 and 69. Intersections Define Solutions on the Basis of Equation 72.

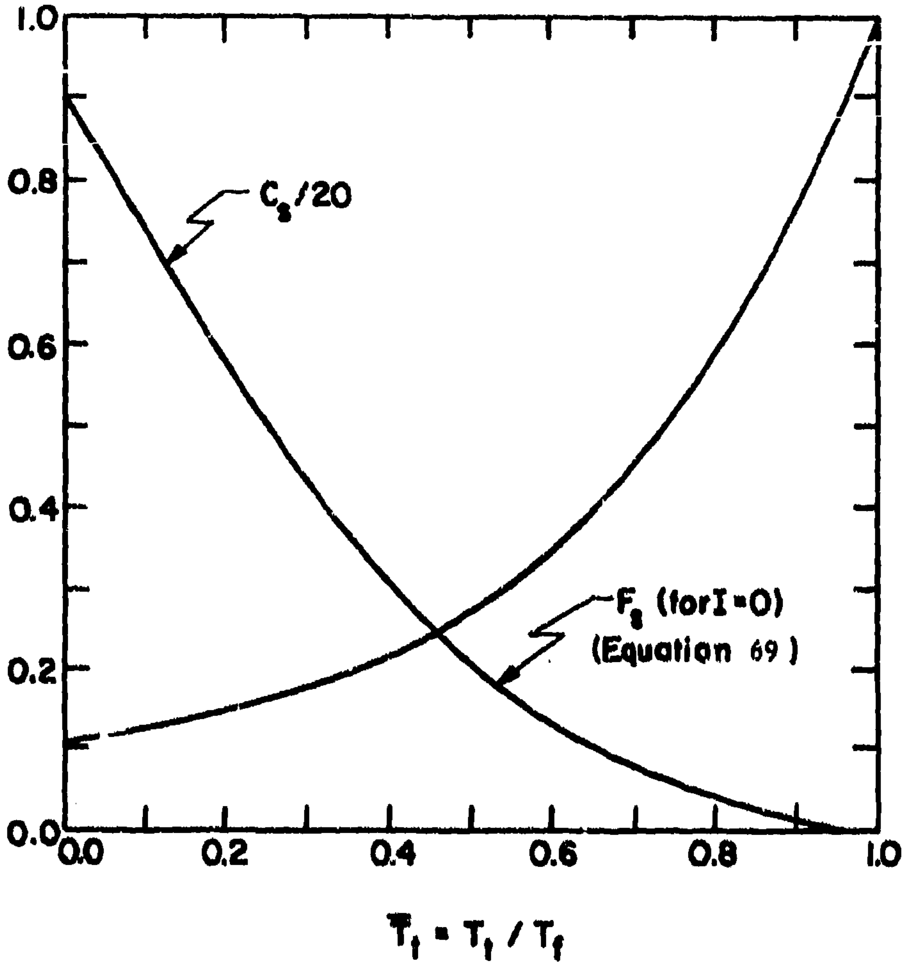

Figure 48. The Effect of C_S on $\overline{T}_t$ and the Corresponding Radiation Parameter F_S for the case where I = 0 (i.e. $\overline{T}_i = \overline{T}_f$) Based on Equation 74.

UNCLASSIFIED
Security Classification

DOCUMENT CONTROL DATA - R & D

(Security classification of title, body of abstract and indexing annotation must be entered when the overall report is classified)

1. ORIGINATING ACTIVITY (Corporate author) ManLabs, Inc. 21 Erie Street Cambridge, Massachusetts 02139	2a. REPORT SECURITY CLASSIFICATION UNCLASSIFIED; 2b. GROUP N/A

3. REPORT TITLE
Stability Characterization of Refractory Materials Under High Velocity Atmospheric Flight Conditions - Part IV-Volume I: Theoretical Correlation of Material Performance with Stream Conditions

4. DESCRIPTIVE NOTES (Type of report and inclusive dates)
Technical Documentary Report, April 1966 to July 1969

5. AUTHOR(S) (First name, middle initial, last name)
Larry Kaufman, Harvey Nesor, Harold Bernstein and Judson R. Baron

6. REPORT DATE	7a. TOTAL NO. OF PAGES	7b. NO. OF REFS
September 1969	115	41

8a. CONTRACT OR GRANT NO. AF33(615)-3859	9a. ORIGINATOR'S REPORT NUMBER(S) N/A
b. PROJECT NO. 7312 Task 731201	
c. 7350 Tasks 735001 and 735002	9b. OTHER REPORT NO(S) (Any other numbers that may be assigned this report)
d.	AFML-TR-69-84, Part IV-Volume I

10. DISTRIBUTION STATEMENT This document is subject to special export controls and each transmittal to foreign governments or foreign nationals may be made only with prior approval of the Air Force Materials Laboratory (MAMC), Wright-Patterson Air Force Base, Ohio 45433.

11. SUPPLEMENTARY NOTES	12. SPONSORING MILITARY ACTIVITY
N/A	Air Force Materials Laboratory (MAMC) Wright-Patterson Air Force Base Ohio 45433

13. ABSTRACT

The oxidation of refractory borides, graphites and JT composites, hyper-eutectic carbide-graphite composites, refractory metals, coated refractory metals, metal-oxide composites, and iridium coated graphites in air have been studied under high velocity atmospheric flight conditions. Elucidation of the relationship between hot gas/cold wall (HG/CW) and cold gas/hot wall (CG/HW) surface effects in terms of heat and mass transfer rates at high temperatures was a principal goal.

A method of presentation which compares recession rate as a function of heat flux and enthalpy for the candidate materials was developed. This description provides a means for comparing performance for various trajectories by applying a flux/enthalpy-altitude/velocity translation in considering candidate materials. Comparison of the trajectory of the FDL-7MC lifting reentry vehicle (Lift/Drag ratio between 2.5 and 3.0 and a 3" nose radius) eliminates all of the candidate materials except the boride composites. These composites have survived multicycle exposures totaling 20,000 seconds under conditions simulating the most severe portions of the FDL-7MC trajectory.

Measurement of temperature gradients through oxide films formed during arc plasma exposures indicate substantial gradients (1000°R through 100 mils) can exist.

This abstract is subject to special export controls and each transmittal to foreign governments or foreign nationals may be made only with prior approval of the Air Force Materials Laboratory (MAMC), Wright-Patterson Air Force Base, Ohio 45433.

DD FORM 1 NOV 65 1473 REPLACES DD FORM 1473, 1 JAN 64, WHICH IS OBSOLETE FOR ARMY USE.

UNCLASSIFIED
Security Classification

UNCLASSIFIED
Security Classification

14. KEY WORDS	LINK A		LINK B		LINK C	
	ROLE	WT	ROLE	WT	ROLE	WT
Oxidation						
Refractory borides						
Graphites						
JT composites						
Hypereutectic carbide-graphite composites						
Iridium coated graphites						
Heat flux						
Enthalpy						
Trajectories						
Lift/Drag						
Multicycle exposures						
Temperature gradients						
Surface temperature						
Gas velocity						
Stagnation pressure						
Metal-oxide composites						
Refractory metals						
Coated refractory metals						

UNCLASSIFIED
Security Classification